

Draft ver. March 1, 2024

Catalog of dense cores in the Orion A giant molecular cloud¹

YOSHITO SHIMAJIRI^{1,2,3}, Y. KITAMURA⁴, F. NAKAMURA², M. MOMOSE⁵, M. SAITO^{2,3}, T. TSUKAGOSHI⁵, M. HIRAMATSU², T. SHIMOIKURA⁶, K. DOBASHI⁶, C. HARA⁷, and R. KAWABE²

Yoshito.Shimajiri@cea.fr

ABSTRACT

We present Orion A giant molecular cloud core catalogs, which are based on 1.1 mm map with an angular resolution of $36''$ (~ 0.07 pc) and C^{18}O ($J=1-0$) data with an angular resolution of $26.4''$ (~ 0.05 pc). We have cataloged 619 dust cores in the 1.1 mm map using the Clumpfind method. The ranges of the radius, mass, and density of these cores are estimated to be $0.01 - 0.20$ pc, $0.6 - 1.2 \times 10^2 M_{\odot}$, and $0.3 \times 10^4 - 9.2 \times 10^6 \text{ cm}^{-3}$, respectively. We have identified 235 cores from the C^{18}O data. The ranges of the radius, velocity width, LTE mass, and density are $0.13 - 0.34$ pc, $0.31 - 1.31 \text{ km s}^{-1}$, $1.0 - 61.8 M_{\odot}$, and $(0.8 - 17.5) \times 10^3 \text{ cm}^{-3}$, respectively. From the comparison of the spatial distributions between the dust and C^{18}O cores, four types of spatial relations were revealed: (1) the peak positions of the dust and C^{18}O cores agree with each other (32.4% of the C^{18}O cores), (2) two or more C^{18}O cores are distributed around the peak position of one dust core (10.8% of the C^{18}O cores), (3) 56.8% of the C^{18}O cores are not associated with any dust cores, and (4) 69.3% of the dust cores are not associated with any C^{18}O cores. The data sets and analysis are public.

¹Laboratoire AIM, CEA/DSM-CNRS-Université Paris Diderot, IRFU/Service d’Astrophysique, CEA Saclay, F-91191 Gif-sur-Yvette, France

²National Astronomical Observatory of Japan, 2-21-1 Osawa, Mitaka, Tokyo 181-8588, Japan

³Nobeyama Radio Observatory, 462-2 Nobeyama, Minamimaki, Minamisaku, Nagano 384-1305, Japan

⁴Institute of Space and Astronautical Science, Japan Aerospace Exploration Agency, 3-1-1 Yoshinodai, Chuo-ku, Sagamihara, Kanagawa 252-5210, Japan

⁵College of Science, Ibaraki University, 2-1-1 Bunkyo, Mito, Ibaraki 310-8512, Japan

⁶Department of Astronomy and Earth Sciences, Tokyo Gakugei University, Koganei, Tokyo 184-8501, Japan

⁷The University of Tokyo, 7-3-1 Hongo Bunkyo, Tokyo 113-0033, Japan

Subject headings: catalogs, ISM: individual objects (Orion-A GMC)

1. Introduction

Stars are born in dark clouds and giant molecular clouds (GMCs) which consist primarily of molecular hydrogen (e.g., Cohen & Kuhi 1979; Tatematsu et al. 1993; Myers et al. 1995; Mardones et al. 1997; Ohashi et al. 1997; Dobashi et al. 2005; Buckle et al. 2012; Liu et al. 2012). The densest portions of the clouds are known as dense cores or molecular cloud cores where stars form through the gravitational collapse. To investigate such dense cores, the millimeter dust continuum emission is a good tracer (Motte et al. 1998; Johnstone et al. 2006; Kauffmann et al. 2008; Belloche et al. 2011). The observations in molecular lines are also required to investigate the dynamical states of the dense cores and to divide the cores overlapped in the same line of sight. Thus, a dense core survey both in the dust continuum and molecular line emission toward the overall cloud is essential to understand the formation and evolution of the dense cores.

In the last twenty years, many authors have investigated the dense cores in the dust continuum or molecular line emission toward the ρ Ophiuchi, Taurus, L1333, Chameleon I, Lupus III, CrA, Pipe nebula, and Southern Coalsack regions (Motte et al. 1998; Tachihara et al. 2002; Onishi et al. 2002; Dzib et al. 2013; Sánchez-Monge et al. 2013). However, dense core surveys covering the entire extent of one continuous cloud have been limited.

There are mapping data both in the dust continuum and molecular line emission toward the Orion-A giant molecular cloud (Orion-A GMC) which is the nearest GMC ($D=400$ pc Menten et al. 2007; Sandstrom et al. 2007; Hirota et al. 2008) and the best-studied one. Thus, the Orion-A GMC is one of the best regions to investigate the distributions and physical properties of the dense cores. In the Orion-A GMC, a large filamentary structure with a length of several $\times 10$ pc is seen along the north-south direction (Bally et al. 1987; Nagahama et al. 1998); the filamentary structure is known as the integral-shaped filament. Recently, Polychroni et al. (2013) identified filaments and dense cores in L 1641 N using the Herschel PACS 70/160 μm and SPIRE 250/350/500 μm data and found that most (71%) of the prestellar cores are located along the filaments. Many authors have carried out observations in the dust continuum emission at 850 μm , 1.2 mm, and 1.3 mm to investigate the physical properties of dense cores in the Orion-A GMC (Chini et al. 1997; Johnstone & Bally

¹The data sets and annotation files for *MIRIAD* and *KARMA* of Tables 2 and 4 are available at the NRO star-formation project web site via <http://th.nao.ac.jp/MEMBER/nakamrfm/sflegacy/data.html>.

1999; Nutter & Ward-Thompson 2007; Davis et al. 2009). Observations in dense-gas tracers such as the H¹³CO⁺, N₂H⁺, C¹⁸O, and CS emission lines have also been carried out (Tatematsu et al. 1993, 1998, 2008; Ikeda et al. 2007). These observations have, however, focused only on the integral-shaped filament. Hence, the distribution of the dense cores on the outside of the integral-shaped filament has not been revealed.

Previous authors (Shimajiri et al. 2011; Nakamura et al. 2012; Shimajiri et al. 2014) have presented wide, sensitive 1.1-mm dust-continuum and C¹⁸O ($J = 1-0$) line maps of the northern part of the Orion-A GMC with the AzTEC camera mounted on the Atacama Submillimeter Telescope Experiment (ASTE) 10-m telescope and with BEARS mounted on the Nobeyama Radio Observatory (NRO) 45 m telescope, respectively. In the 1.1 mm dust continuum map, we found the following new substructures in addition to the well-known integral-shaped filament. In the OMC-2/3 region, a filamentary structure is found to the east of the integral-shape filament. A shell-like structure around the HII region, M 43, and a filamentary structure associated with Dark Lane South Filament (DLSF), which is known as the photon-dominated region (PDR), (Rodríguez-Franco et al. 2001), are detected. In the southmost region where an active cluster-forming region of L 1641 N is located, four filamentary structures with a length of $\sim 0.5 - 2.0$ pc are seen almost aligned with each other. In the C¹⁸O ($J=1-0$) map, we found that the overall distribution of C¹⁸O is similar to that of the 1.1 mm dust continuum emission.

In this paper, we present a catalog of the identified cores in the 1.1-mm dust continuum and C¹⁸O ($J=1-0$) emission line using the Clumpfind method and their properties of the peak flux density, radius, mass, density, and aspect ratio. The 1.1 mm dust continuum and C¹⁸O emission data are from Shimajiri et al. (2011) and Shimajiri et al. (2014), respectively. We compare the physical properties of the identified C¹⁸O cores in the OMC-1, OMC-2/3, OMC-4, Dark Lane South Filament (DLSF), and bending structure regions to investigate region-to-region variations. In addition, we compare the spatial distributions of the AzTEC/ASTE 1.1 mm dust, BEARS/NRO 45m C¹⁸O, SCUBA/JCMT² 850 μ m (Nutter & Ward-Thompson 2007), BEARS/NRO 45m H¹³CO⁺ (Ikeda et al. 2007), and BEARS/NRO 45m N₂H⁺ (Tatematsu et al. 2008) cores to unveil their physical relationships.

²James Clerk Maxwell Telescope

2. Catalogs

2.1. 1.1-mm dust continuum emission

2.1.1. Core identification in the AzTEC 1.1 mm dust continuum map

The overall distribution of the AzTEC 1.1-mm dust continuum emission was revealed by Shimajiri et al. (2011). Here, we identify cores using the two-dimensional Clumpfind method (Williams et al. 1994). This algorithm has been widely used for the identification of cores and clumps (e.g., Kirk et al. 2006; Rathborne et al. 2009; Ikeda & Kitamura 2011; Tanaka et al. 2013). The algorithm works well with reasonable parameters to identify cores or clumps, although several authors have pointed out some shortcomings of the clumpfind algorithm (Pineda et al. 2009). Pineda et al. (2009) examined the behavior of the algorithm by changing the threshold level from 3σ to 20σ , a wider range than Williams et al. (1994) did, and found that the power-law index of the core mass function (CMF) sensitively depends on the threshold for the higher threshold range $> 5\sigma$. Ikeda & Kitamura (2009), however, demonstrated the weak dependence of core properties and CMF in Orion A on the threshold in a reasonable range from 2σ to 5σ levels, which was also shown by Pineda et al. (2009). As described in Sections 2.1.2 and 2.2.2, the physical properties (radius, mass, velocity width, etc.) of the condensations identified by the Clumpfind in this paper are similar to those of the star forming dense cores traced by the H¹³CO⁺ line (Ikeda et al. 2007, and references therein. See also Appendix A of this paper). In this paper, we will therefore define cores identified by the Clumpfind with a similar threshold value as they used.

The noise distribution of the AzTEC 1.1 mm continuum emission is not uniform over the image and is higher in the outer region. Before applying the Clumpfind (Williams et al. 1994), we cut off the outer edge of the AzTEC image, where the coverage is less than 30% and the noise level is higher by a factor of 1.3 than that in the central part. This is because the observations were made by the raster scan that boresights in azimuth and elevation and because the AzTEC 1.1 mm dust continuum image was obtained by mosaicing observations of two fields. The noise level is ~ 9 mJy beam⁻¹ in the central region and ~ 12 mJy beam⁻¹ in the outer region of the trimmed image. We applied the Clumpfind method to the AzTEC 1.1 mm dust continuum image with the criteria that the threshold should be the 2σ level and the depth of the valley between adjacent peaks should be larger than the 2σ interval. We adopted 9 mJy beam⁻¹ which is the noise level ($= 1\sigma$) in the central region as the noise level in the Clumpfind. Next, we removed cores whose FWHM sizes are less than the effective angular resolution ($\sim 36''$). Furthermore, we only took cores having peak intensities above the 4σ noise level. As described by Shimajiri et al. (2011), the emission around the central Orion-KL region could not be reconstructed as an accurate structure with the AzTEC data-

reduction technique, because the continuum emission around Orion-KL is too bright. Thus, we removed cores in the central Orion-KL region. As a result, we identified 619 dust cores(see also Appendix B), as shown in Figure 1. Here, we note that the 257 cores are located in the C¹⁸O observed region, excluding the central part of the Orion-KL region (see Figure 2).

To investigate the performance of the FRUIT data reduction, Shimajiri et al. (2011) performed a simulated source extraction in which Gaussian sources with various FWHM sizes and total flux densities were artificially embedded in the Orion data, and obtained the following result: The larger FWHM size of the model source, the lower the recovered fraction of the input total flux density of the source. In the case that the FWHM size of the input source is under 150'' (~ 0.3 pc), the output total flux density is underestimated by less than 20%. The total flux density of the source with a peak flux density under 20 Jy is underestimated by less than 10%. Moreover, the restored image of the 1.1 mm dust continuum emission is consistent with that of the SCUBA 850 μ m dust continuum emission. Consequently, the total flux densities of the sources in our map should be recovered by more than 80%, because the peak flux density FWHM size of the identified 1.1 mm dust cores are smaller than 20 Jy and 0.2 pc, respectively, as described in Section 2.1.2 (see also Appendix C).

2.1.2. Physical properties of the 1.1 mm dust cores

The mass of the 1.1 mm dust core ($\equiv M_{\text{H}_2}$) was derived from the total flux density at 1.1 mm, F_ν , on the assumption that all the 1.1 mm continuum emission arises from dust and that the emission is optically thin, using the formula,

$$M_{\text{H}_2} = \frac{F_\nu D^2}{\kappa_\nu B_\nu(T_d)}. \quad (1)$$

We adopted the dust mass opacity of $\kappa_\nu = 0.1 \left(\frac{\nu}{10^{12}\text{Hz}}\right)^\beta \text{ cm}^2 \text{ g}^{-1}$ with $\beta=2$ (Hildebrand 1983; Chini et al. 1997) and $D = 400$ pc. For the dust temperature, we adopted $T_d=20$ K (Cesaroni & Wilson 1994). We determined the apparent core radius R_{obs} as

$$R_{\text{obs}} = \left(\frac{A}{\pi}\right)^{\frac{1}{2}}, \quad (2)$$

assuming that the core is a sphere. Here, A is the projected area of the core, derived by the Clumpfind. We further estimated the core radius R_{core} corrected for the beam size on the assumption that the core has a Gaussian intensity profile as,

$$R_{\text{core}} = \left\{ R_{\text{obs}}^2 - \left[\frac{\Delta\theta/2}{\sqrt{2 \ln 2}} (2 \ln \frac{T_{\text{peak}}}{\Delta I})^{1/2} \right]^2 \right\}^{1/2}, \quad (3)$$

where $\Delta\theta$ ($=36''$) is the effective beam size of the AzTEC 1.1 mm dust continuum map, T_{peak} is the peak intensity of the core, and ΔI is the threshold level in the core identification (see Williams et al. 1994). We note that the grid size of the map was set to the effective angular resolution in the Clumpfind analysis. The mean gas density ($\equiv n$) of the core was derived as,

$$n = \frac{3M_{\text{H}_2}}{4\pi\mu m_{\text{H}} R_{\text{core}}^3}, \quad (4)$$

where μ is the mean molecular weight per free particle taken to be 2.33 and m_{H} is the mass of a hydrogen atom. The range of the radius R_{core} , mass M_{H_2} , and density n of the 1.1 mm dust cores are estimated to be 0.01 – 0.2 pc, $0.6 - 1.2 \times 10^2 M_{\odot}$, and $0.3 \times 10^4 - 9.2 \times 10^6 \text{ cm}^{-3}$, respectively. Figure 3 shows histograms of the radius, mass, density of the 1.1 mm dust cores. In the distributions of R_{core} , M_{H_2} , and n of the 1.1 mm dust cores, peaks are seen at 0.09 pc, $1.3 M_{\odot}$, and $1.0 \times 10^4 \text{ cm}^{-3}$, respectively. The uncertainty of R_{core} is 0.07 pc, which is derived from the uncertainty in the estimation of the core projected area. As estimated in Section 2.1.1, the uncertainty of the total flux density of the identified 1.1mm core should be less than 20%, since the size of the core is less than 0.2 pc. Since the uncertainty of the total flux density of the identified 1.1mm core should be less than 20% (see Section 2.1.1), the uncertainty of M_{H_2} is 20%. We summarized the mean, minimum, and maximum values of each physical parameter in Table 1. Table 2 shows the physical properties of all the identified cores.

2.2. The C¹⁸O ($J=1-0$) emission line

2.2.1. Core identification in the C¹⁸O map

The overall distribution of the C¹⁸O emission and the velocity structure are described by Shimajiri et al. (2014). To identify cores from the C¹⁸O ($J=1-0$) data, we applied the Clumpfind algorithm (Williams et al. 1994) to the C¹⁸O ($J=1-0$) cube data with an angular resolution of 26''.4 and a velocity channel width of 0.104 km s⁻¹. Here, note that we applied the Gaussian gridding convolution function (GCF) with 22''.5 FWHM size to the original C¹⁸O data, resulting in the effective angular resolution of 26''.4, and did no smoothing in

the velocity space. We adopted the criteria that the threshold should be the 2σ level ($1\sigma = 0.19$ K in T_{MB}) and the depth of the valley between adjacent peaks should be larger than the 2σ interval as suggested by Williams et al. (1994). We also followed the additional criteria introduced by Ikeda et al. (2007) and rejected ambiguous or fake core candidates whose sizes and velocity widths are smaller than the spatial and velocity resolutions, respectively: a core must contain two or more continuous velocity channels, and they must have at least 3 pixels whose intensities are above the 3σ level, and in addition the pixels must be connected to one another in both the space and velocity domains. As a result, we identified 235 cores in total (see Figure 2).

2.2.2. Physical properties of the C^{18}O cores

We estimated the radius R_{core} , velocity width in FWHM dV_{core} , LTE (Local Thermo-dynamic Equilibrium) mass M_{LTE} , virial mass M_{VIR} , and mean density n of the C^{18}O cores. The definitions of these parameters are the same as those used by Ikeda et al. (2007) and Ikeda & Kitamura (2009). We estimated the core radius R_{core} using equation (3). To obtain the observed velocity width dV_{obs} , we calculated a velocity dispersion within the C^{18}O cores, and then we multiplied the factor $\sqrt{8\ln 2}$ to convert the core velocity dispersion to the FWHM line width on the assumption of a Gaussian profile. Thus, the observed velocity width dV_{obs} is given by

$$dV_{\text{obs}} = \sqrt{8\ln 2} \left[\frac{\sum_i v_i^2 I_i}{\sum_i I_i} - \left(\frac{\sum_i v_i I_i}{\sum_i I_i} \right)^2 \right]^{1/2}, \quad (5)$$

where v_i and I_i are the radial velocity and intensity of the i -th pixel in each core, respectively. The velocity width dV_{core} should be corrected for the velocity resolution, $dV_{\text{spec}}=0.104$ km s $^{-1}$ as

$$dV_{\text{core}} = \sqrt{dV_{\text{obs}}^2 - dV_{\text{spec}}^2}. \quad (6)$$

In the mass estimation, we adopted $T_{\text{ex}} = 20$ K (Cesaroni & Wilson 1994). For the fractional abundance of C^{18}O relative to H_2 , $X_{\text{C}^{18}\text{O}}$, we adopted 1.7×10^{-7} (Frerking et al. 1982). Assuming that the $\text{C}^{18}\text{O}(J=1-0)$ emission is optically thin, we have

$$M_{\text{LTE}} = 3.47 \times 10^{-2} \left(\frac{X_{\text{C}^{18}\text{O}}}{1.7 \times 10^{-7}} \right)^{-1} T_{\text{ex}} e^{5.27/T_{\text{ex}}} \left(\frac{D}{400 \text{ pc}} \right)^2 \left(\frac{\Delta\theta}{26''.4} \right)^2 \left(\frac{\eta_{\text{MB}}}{0.4} \right)^{-1} \left(\frac{\Sigma_i T_{\text{A}}^* \Delta V_i}{\text{K kms}^{-1}} \right) M_{\odot}, \quad (7)$$

where $\Sigma_i T_{\text{A}}^* \Delta V_i$ is the total integrated intensity of the core. We adopted a main beam efficiency η_{MB} of 38% for the 2010 season data and 36% for the 2013 season data (see Shimajiri et al. 2014). Note that we adopted the grid spacing of the data cube, $\Delta\theta$, set to the effective angular resolution of $26''.4$. The mean gas density of the core was derived by

$$n = \frac{3M_{\text{LTE}}}{4\pi\mu m_{\text{H}} R_{\text{core}}^3}. \quad (8)$$

The virial mass assuming that the cores have spherical shapes and the virial ratio are estimated as

$$M_{\text{VIR}} = 209 \left(\frac{R_{\text{core}}}{\text{pc}} \right) \left(\frac{dV_{\text{core}}}{\text{km s}^{-1}} \right)^2 M_{\odot} \quad (9)$$

and

$$\mathcal{R}_{\text{vir}} = \frac{M_{\text{VIR}}}{M_{\text{LTE}}}, \quad (10)$$

respectively. The range of R_{core} , dV_{core} , M_{LTE} , and n are $0.13 - 0.34 \text{ pc}$, $0.31 - 1.31 \text{ km s}^{-1}$, $1.0 - 61.8 M_{\odot}$, and $(0.8 - 17.5) \times 10^3 \text{ cm}^{-3}$, respectively (see Table 3). Figure 3 shows histograms of R_{core} , M_{LTE} , and n of the C^{18}O cores: peaks are seen at 0.22 pc , $15.1 M_{\odot}$, and $2.9 \times 10^3 \text{ cm}^{-3}$, respectively. The uncertainty of R_{core} is 0.05 pc derived from the uncertainty in the estimation of the core projected area. The uncertainty of dV_{core} is 0.104 km s^{-1} , corresponding to the velocity resolution. The uncertainty of M_{LTE} is a factor of 6, which is derived from the uncertainty in $X_{\text{C}^{18}\text{O}}$ (Shimajiri et al. 2014). The physical properties of the individual C^{18}O cores are listed in Table 4.

Figures 4 (a) and (b) show virial ratio - LTE mass and virial ratio - density relations of the identified C^{18}O cores, respectively. We consider that the cores with a \mathcal{R}_{vir} value less than three are under virial equilibrium according to Ikeda & Kitamura (2009). With the increasing LTE mass and density, the virial ratio decreases; a similar trend between the LTE mass and the virial ratio was also found by Dobashi et al. (1996), Yonekura et al. (1997), and Ikeda et al. (2007). Most of the bound C^{18}O cores are distributed in the filamentary

structure. On the other hand, most of the unbound C¹⁸O cores are distributed outside the filamentary structure (see Section 3.5). Figure 4 (c) shows a LTE mass - R_{core} relation of the C¹⁸O cores. The best-fit power-law functions for the unbound and bound cores are $\log_{10}(M_{\text{LTE}}/M_{\odot}) = (3.8 \pm 13.6)\log_{10}(R_{\text{core}}/\text{pc}) + (3.2 \pm 9.3)$ and $\log_{10}(M_{\text{LTE}}/M_{\odot}) = (6.6 \pm 16.5)\log_{10}(R_{\text{core}}/\text{pc}) + (5.3 \pm 10.5)$, respectively.³ No significant difference can be seen between the data distributions for the unbound and bound core due to the larger uncertainty in the estimation of the LTE mass, although the trend that the LTE mass of the bound core is larger than that of the unbound core can be recognized in Figure 4 (c). Figure 4 (d) shows a dV_{core} - R_{core} relation of the identified C¹⁸O cores. The best-fit power-law functions for the unbound and bound cores are $\log_{10}(dV_{\text{core}}/\text{km s}^{-1}) = (2.7 \pm 14.6)\log_{10}(R_{\text{core}}/\text{pc}) + (1.6 \pm 10.0)$ and $\log_{10}(dV_{\text{core}}/\text{km s}^{-1}) = (2.4 \pm 8.3)\log_{10}(R_{\text{core}}/\text{pc}) + (1.3 \pm 5.3)$, respectively. No significant difference can be seen between the data distributions for the unbound and bound cores.

Figure 5 shows the change of the systemic velocity of the cores (i.e., the peak C¹⁸O velocity) along the declination, which is best fitted by the relation ($V_{\text{sys}}/\text{km s}^{-1}$) = (5.1 ± 0.3) (Dec/deg) + (36.5 ± 1.8) . This result suggests a presence of a large-scale velocity gradient along the south-north direction ($\sim 0.7 \text{ km s}^{-1} \text{ pc}^{-1}$) (cf., the velocity gradient along the integral-shaped filament is estimated to be $1.0 \text{ km s}^{-1} \text{ pc}^{-1}$ in the ¹²CO, ¹³CO, H¹³CO⁺, CS lines (Bally et al. 1987; Tatematsu et al. 1993; Ikeda et al. 2007; Shimajiri et al. 2011; Buckle et al. 2012; Shimajiri et al. 2014)).

3. Discussion

3.1. Mass distribution of the 1.1 mm dust cores

Region-to-region variation of the dust core mass distribution can be recognized in Figure 1. The high-mass cores ($M_{\text{H}_2} \geq 10.0 M_{\odot}$) are mainly located in the integral-shaped filament. On the other hand, the intermediate-mass ($1.0 M_{\odot} \leq M_{\text{H}_2} < 10.0 M_{\odot}$) and low-mass ($M_{\text{H}_2} < 1.0 M_{\odot}$) cores tend to appear on the outside of the integral-shaped filament. One of the reasons why the high-mass cores are concentrated in the integral-shaped filament is that the 1.1 mm dust cores in the integral-shaped filament could not be resolved in the AzTEC observations with an angular resolution of $\sim 36''$ (corresponding to $\sim 0.07 \text{ pc}$ at 400 pc). In fact, previous SCUBA 850 μm observations with an angular resolution of \sim

³The χ -square fitting method with uncertainties in both the x and y coordinates was applied by using the IDL MPFITEXY tool (Williams et al. 2010).

14'' (Nutter & Ward-Thompson 2007) resolved each 13 1.1 mm dust core into two or three smaller cores (also see Table 2). Furthermore, interferometer observations with a high angular resolution of $\sim 1 - 3''$ revealed that cores in OMC-2/FIR 4, OMC-2/FIR 6, and L1641 N consist of several smaller cores (Shimajiri et al. 2008, 2009; Stanke & Williams 2007). Observations with interferometers such as the Atacama Large Millimeter/Submillimeter Array (ALMA) are crucial to unveil the internal structures of the cores and confirm whether the trend of the region-to-region variation of the dust core mass distribution is significant.

3.2. Cross identification between the 1.1 mm dust cores and the cataloged YSOs

Recently, Megeath et al. (2012) identified young stellar objects (YSOs) in the Orion A and B molecular clouds from the infrared array camera (IRAC)/Spitzer and multi-band imaging photometer for Spitzer (MIPS)/Spitzer data. They classified 2991 YSOs as pre-main sequence stars with disks and 488 YSOs as protostars using the criterion that the spectral index α ($=\lambda F_\lambda/d\lambda$) ≥ -0.3 for protostars and $\alpha < -0.3$ for pre-main sequence (PMS) stars with disks. The active galactic nucleus (AGN), galaxies with polycyclic aromatic hydrocarbons (PAH) emission, outflow shock knots and stars contaminated by PAH emission are excluded from these YSO catalog (see Megeath et al. 2012). The AzTEC map includes 1801 of 2991 pre-main sequence stars with disks and 202 of 488 protostars. The central part of the Orion-KL region, which could not be well reconstructed by the AzTEC, includes 122 pre-main sequence stars with disks and 22 protostars. We removed these pre-main sequence stars with disks and protostars from the following comparison with our cores.

Figure 6 shows a histogram of the separations between the YSOs cataloged by Megeath et al. (2012) and the peak positions of the 1.1 mm dust cores nearest to them. In the figure, only the protostars and PMSs with separations less than 36'', which is the angular resolution of the AzTEC 1.1 mm dust continuum data, are counted. The distribution of the protostars has a peak at a separation of 7.5'' and decreases to 15''. Thus, we adopted the 15'' separation as a criterion to identify the YSOs associated with the 1.1 mm dust cores. As a result, 50/1679 (3.0%) of the pre-main sequence stars with disks are associated with the 1.1 mm dust cores and 49/180 (36.1%) of the protostars associated with the cores. Figures 7–9 show close-up images of the 1.1 mm dust cores associated with the YSOs. We note that the spatial resolution of the AzTEC 1.1 mm dust continuum map is $\sim 36''$ (corresponding to ~ 0.07 pc at 400 pc), which cannot resolve each dense core in a cluster-forming region where many dense cores are concentrated in small areas. This effect should lower the detection rate. For example, previous dust continuum observations in the 1.3-mm dust continuum emission with

an angular resolution of $11''$ found eleven dust cores in the OMC-2 region (Chini et al. 1997), but only three cores are identified in our AzTEC 1.1 mm dust continuum map. In addition, we cannot exclude the possibility that the dust cores and the YSOs overlap by chance on the same line of sight. However, this possibility is thought to be small, since the YSOs are likely to be in the Orion-A GMC.

To investigate the region-to-region variation of the environments and evolutionary phases of star formation, we compared the number density of the 1.1 mm dust cores, protostars, and pre-main sequence stars in OMC-1, OMC-2/3, OMC-4, DLSF, the bending structure, and the southern part in the 1.1 mm dust continuum map. The OMC-1 region is known to be a high-mass star-forming region (Furuya & Shinnaga 2009; Bally et al. 2011; Lee et al. 2013). The OMC-2/3 region is known to be an intermediate-mass star-forming region (Takahashi et al. 2006, 2008, 2009; Takahashi & Ho 2012; Takahashi et al. 2013; Shimajiri et al. 2008, 2009). The DLSF is influenced by the far ultraviolet (FUV) radiation from the trapezium cluster (Rodríguez-Franco et al. 2001; Shimajiri et al. 2011, 2013, 2014). In the southern area of the 1.1 mm dust continuum map, cloud-cloud collision is suggested to be occurring by Nakamura et al. (2012). We summarize numbers and number densities of the 1.1 mm dust cores, protostars, and pre-main sequence stars in each region in Table 5. Although the six areas/regions are not uniquely and rigorously defined and this is likely to introduce some uncertainties in statistical analyses and discussions, the number density of the 1.1 mm dust cores in the southern part of the 1.1 mm dust continuum map ($4.2 \text{ cores pc}^{-2}$) is found to be the lowest. In the integral-shaped filament, the number densities of the protostars in OMC-1, OMC-2/3, and OMC-4 ($6.3 - 8.0 \text{ protostars pc}^{-2}$) are similar. On the other hand, the number densities of protostars in the other regions of DLSF, the bending structure, and the southern part are 3 - 27 times lower than those in the integral-shaped filament. This is consistent with the fact that the OMC-1, OMC-2/3, and OMC-4 regions are more active star-forming regions than the DLSF, bending structure, and southern regions. The number density ratios of the 1.1 mm dust cores without YSOs to YSOs including protostars and pre-main sequence stars with disk in OMC-2/3 ($6.8 \text{ cores pc}^{-2}/41.8 \text{ YSOs pc}^{-2} = 0.16$) and OMC-4 ($7.4 \text{ cores pc}^{-2}/81.3 \text{ YSOs pc}^{-2} = 0.09$) are 2.6–6.0 times lower than those in the other regions of DLSF ($11.1 \text{ cores pc}^{-2}/20.3 \text{ YSOs pc}^{-2} = 0.54$), the bending structure ($8.4 \text{ cores pc}^{-2}/18.1 \text{ YSOs pc}^{-2} = 0.46$), and the southern part ($4.2 \text{ cores pc}^{-2}/8.6 \text{ YSOs pc}^{-2} = 0.49$). Thus, we speculate that the DLSF, bending structure, and southern regions are in younger evolutionary stages than that of the integral-shaped filament.

This interpretation is supported by the spatial variation of the mean density of the 1.1mm dust core. The mean densities of the 1.1mm dust cores in OMC-2/3 and OMC-4 are 6.2×10^4 and $18.9 \times 10^4 \text{ cm}^{-3}$, respectively, while those in the bending, DLSF, and south regions are 1.7×10^4 , 2.1×10^4 , and $3.0 \times 10^4 \text{ cm}^{-3}$, respectively. Consequently,

the mean densities of the 1.1 mm dust cores in the integral-shaped filament is 2.1 – 11.1 times higher than those in the DLSF, bending structure, and southern regions. Since the gas density is generally thought to increase as star formation progresses, the difference in mean density suggests that the integral-shaped filament is most evolved. We must consider another possibility that the OMC-2/3 and OMC-4 regions are forming higher mass stars. In fact, the OMC-2/3 region is known as an intermediate star forming region (Takahashi et al. 2006). However, as shown in Fig. 10 (c), the difference in the M_{LTE} distribution between OMC-2/3 and Bending as well as between DLSF and OMC-4 is not significant, suggesting that the stars with similar masses will form on the assumption of the same star formation rate among the regions.

3.3. Comparison of the core properties in the OMC-1, OMC-2/3, OMC-4, DLSF, and bending structure regions

In the Orion-A GMC, the environments and evolutional phases of star formation have considerable region-to-region variations as discussed in Section 3.2. To investigate the influence of the different environment and evolutional phase on physical properties of the dense cores, we compare the physical properties of the C¹⁸O cores in the OMC-1, OMC-2/3, OMC-4, DLSF, and bending structure regions. Figure 10 shows histograms of the radius, velocity width, LTE mass, and virial ratio of the C¹⁸O cores, respectively, in the five regions. To quantitatively examine the similarities of the physical properties among the five regions, we applied the Kolmogorov-Smirnov (KS) test, which considers the maximum deviation between the distributions of two samples (e.g., Wall & Jenkins 2012), to the five histograms in each panel (see Tables 6 and 7). The results of the KS test show that there is no significant difference among the five regions for most of the physical properties. Although the R_{core} values in DLSF are relatively small as shown in Fig. 10 (a), the KS test shows no significant difference for the R_{core} values due to the small sample for DLSF. The dV_{core} distribution in DLSF is significantly different from that in the OMC-2/3 region with a significant level of five percent (p -value = 3.1%). The dV_{core} value in DLSF is relatively small as shown in Fig. 10 (b). The LTE-mass distribution in DLSF is significantly different from those in OMC-1 and OMC-2/3 with a significant level of five percent (p -value = 0.7%). As described in the above, the LTE-mass distributions in DLSF and OMC-4 have two distinct peaks at $M_{\text{LTE}} = 2.9 M_{\odot}$ and $24.2 M_{\odot}$.

3.4. Effects of external pressure and internal magnetic field on the dynamical states of the C¹⁸O cores

The external pressure and internal magnetic (B) field in the cores are important factors to determine their dynamical states. Recently, Li et al. (2013) performed high angular (5'') resolution observations with a velocity resolution of 0.6 km s⁻¹ in NH₃ using the Very Large Array (VLA) and Green Bank Telescope (GBT) toward the OMC-2/3 region (c.f., the mean velocity width of the C¹⁸O cores is 0.61 km s⁻¹). They found that most of the massive cores are supercritical from the comparison between mass and critical mass, suggesting that cores will collapse or fragment. The critical mass M_{critical} is defined as $M_{\text{critical}} = M_J + M_\Phi$, where M_J and M_Φ are the Jeans mass and the maximum mass that can be supported by a steady B field (e.g., McKee & Zweibel 1992). Here, we investigate the dynamical states of the C¹⁸O cores with the external pressure and the internal magnetic field according to Li et al. (2013).

The Jeans mass is estimated as

$$M_J = 1.182 \frac{\sigma^4}{G^{3/2} P_{\text{ic}}^{1/2}}, \quad (11)$$

where G is the gravitational constant, σ is the one-dimensional velocity dispersion within the core, and P_{ic} is the external pressure. The pressure P_{ic} can be expressed as $P_{\text{ic}} = n_{\text{ic}} \mu m_H \sigma_{\text{ic}}^2$. We considered the tenuous gas traced by the ¹³CO (1–0) emission line as the external gas of the C¹⁸O cores. Thus, we adopted the density n_{ic} of 2.0×10^3 cm⁻³ (Nagahama et al. 1998) and the velocity dispersion σ_{ic} of 0.67 km s⁻¹ (Shimajiri et al. 2014). The velocity dispersion in the core, σ , can be estimated from the core velocity width dV_{core} as $\sigma = dV_{\text{core}} / \sqrt{8 \ln 2}$, assuming a Gaussian velocity profile. As a result, the Jeans mass M_J of the C¹⁸O cores is estimated to be $0.2 - 55.6 M_\odot$ (see Table 3). On the other hand, the maximum mass can be estimated using the formula,

$$M_\Phi = c_\Phi \frac{\pi B R_{\text{core}}^2}{G^{1/2}}, \quad (12)$$

where c_Φ is a non-dimensional scaling factor and is 0.12 for an axisymmetric isothermal cloud (Tomisaka et al. 1988) and B is the magnetic field strength. Crutcher et al. (1999) derived the field strength from the observations of the Zeeman effect in CN toward OMC-1 and found $B \sim 0.19 - 0.36$ mG. Here, we adopted 0.1 mG as the field strength according to Li et al. (2013). Thus, the estimated maximum mass could be the lower limit. As a result, the maximum mass M_Φ of the C¹⁸O cores is estimated to be $0.1 - 0.8 M_\odot$ (see Table 3).

Here we define the critical mass ratio \mathcal{R}_c as,

$$\mathcal{R}_c = \frac{M_{\text{LTE}}}{M_J + M_\Phi}. \quad (13)$$

We list M_J , M_Φ , and \mathcal{R}_c of each C^{18}O core in Table 4. Figure 11 shows a relation between the virial and critical mass ratios of the C^{18}O cores. The \mathcal{R}_c value decreases with the increasing the \mathcal{R}_{vir} value. The difference between $\mathcal{R}_{\text{vir}} - \mathcal{R}_c$ relations for the bound and unbound C^{18}O cores are recognized in Fig. 11. The slopes for the bound C^{18}O cores are larger than those for the unbound C^{18}O cores. The best-fit power-law functions are $\mathcal{R}_c = 6.6 \pm 0.12 \mathcal{R}_{\text{vir}}^{-1.16 \pm 0.04}$ for the unbound C^{18}O cores and $\mathcal{R}_c = 12.3 \pm 2.9 \mathcal{R}_{\text{vir}}^{-1.56 \pm 0.18}$ for the bound C^{18}O cores. We found that all the bound C^{18}O cores are supercritical ($\mathcal{R}_c \geq 1$) and 25 of the 61 unbound C^{18}O cores are subcritical ($\mathcal{R}_c < 1$) as seen in Fig. 11. Here, we note that there are large uncertainties in the estimates of the Jeans mass owing to the relation of $M_J \propto \sigma^4$ and in the estimation of the maximum mass owing to the large uncertainty in B . For further investigation of the dynamical states of the dense cores, observations with higher spectral resolution and measurements of the magnetic field strength would be crucial.

3.5. Comparison between the 1.1 mm dust and C^{18}O cores

In Sections 2.1 and 2.2, we have identified the 257 dust and 213 C^{18}O cores using the Clumpfind method and estimated their physical properties in the C^{18}O observing area. The mean R_{core} value of the C^{18}O cores (0.22 ± 0.04 pc) is 2.4 times larger than that of the 1.1 mm dust cores (0.09 ± 0.03 pc). The 1.1 mm dust continuum emission probably traces the inner part of the dense cores, while the C^{18}O emission line probably traces the outer part of the dense cores. The n value range of the 1.1 mm dust cores ($(0.3 - 915.0) \times 10^4 \text{ cm}^{-3}$) is 13 times larger than that of the C^{18}O cores ($(0.8 - 17.5) \times 10^3 \text{ cm}^{-3}$).

We compared the spatial distribution of the 1.1 mm dust cores with that of the C^{18}O cores. Figures 12 – 15 show the positions of the 213 C^{18}O cores on the AzTEC 1.1 mm dust continuum map in the OMC-2/3, OMC-4, DLSF, and bending structure regions. Figure 16 shows the positions of the C^{18}O cores in the OMC-1 region where the 1.1 mm image could not be well reconstructed there. Figure 17 shows the positions of the 1.1 mm dust cores in the southern part of the 1.1 mm dust continuum map where there is no C^{18}O data. We found that the spatial relation between the 1.1 mm dust and C^{18}O cores can be categorized into the following four types as shown in Figure 18:

[Category A] The peak positions of the 1.1 mm dust and C^{18}O cores agree with each other within the 1.1 mm map resolution of $36''$.

[Category B] Several C¹⁸O cores are distributed around the peak positions of the 1.1 mm dust cores within the 1.1 mm map resolution of 36".

[Category C] The C¹⁸O cores not associated with any 1.1 mm dust cores.

[Category D] The 1.1 mm dust cores not associated with any C¹⁸O cores.

Table 8 summarizes the numbers of the 1.1 mm dust and C¹⁸O cores in each category. We found 69 pairs of the dust and C¹⁸O cores in Category A. In this category, one C¹⁸O core seems to be associated with one 1.1 mm dust core. In Category B, there are 23 C¹⁸O cores (10.8%) and 10 dust cores (3.9%). There are three possible explanations for the B type cores. One is the several cores are overlapped in the same line of sight. The V_{LSR} is different among the C¹⁸O cores which are associated with the same 1.1 mm dust core (see Tables 2 and 4). Furthermore, the peak positions of 6/10 dust cores (AzTEC-Ori 110, 232, 234, 242, 272, and 482) coincide with those on the C¹⁸O integrated intensity map which includes all velocity components as well as the dust continuum map. These results suggest that several cores are distributed on the same line of sight. Second is due to the poor angular resolution of the AzTEC data. The resolution of the AzTEC data (= 36") is larger than in the C¹⁸O data (= 26"). To confirm this possibility, we identified the C¹⁸O cores using the C¹⁸O data smoothed to the same angular resolution as the AzTEC 1.1mm map (=36"). As a result, 5 of 10 dust cores (AzTEC-Ori 162, 232, 242, 273, and 482) are associated with one C¹⁸O core identified on the 36" map, although these dust cores are associated with two C¹⁸O cores identified on the 26".4 map. This result suggests that these 1.1 mm dust cores are not resolved due to the poor angular resolution. Hence, distinct condensations resolved by the C¹⁸O observations may remain unresolved by the AzTEC observations. The other is the depletion of the C¹⁸O molecules in the central parts of dust cores. Such depletion in the central part of the dust condensation has been reported in the B 68 and L 1498 regions (Bergin et al. 2002; Tafalla et al. 2002). Although the inter-core diffuse gas in the Orion-A GMC is warmer than those in low-mass star forming regions, the dense cores are well-shielded from nearby radiation and become cool enough for CO molecules to freeze onto dust grains. In fact, the CO depletion in the dense cores in the Orion-A GMC has been reported by several authors (Ripple et al. 2013; Tatematsu et al. 2014; Ren et al. 2014).

In Category C, we identified 121 C¹⁸O isolated cores. There are two possible origins of these cores. First is due to the poor angular resolution of the AzTEC data. Some 1.1 mm dust cores are associated with two cores in the 850 μm data with an angular resolution of 14", suggesting that the 850 μm data with the higher angular resolution resolved the 1.1 mm dust cores. Some 850 μm cores associated with the C¹⁸O cores are not associated with any 1.1 mm dust cores. These cores are located between two 1.1 mm dust cores or on

elongated structures in the 1.1 mm dust map as shown in Figs. 21 - 22. The reason why the 1.1 mm dust cores are not associated with any 850 μm cores is probably that the 850 μm counterparts in the 1.1 mm map are not identified due to the poor angular resolution. We note that the smoothed 850 μm map with the same angular resolution as in the 1.1 mm map is quite consistent with the 1.1 mm map (see Fig. 20 in Shimajiri et al. 2011). Second is that these C¹⁸O cores do not have high enough column density to be detected in the dust continuum. Figure 19 shows the histogram of each column densities of the 1.1 mm dust, all C¹⁸O cores, and C¹⁸O cores in Category C. The column densities of each cores is estimated from the equation, $N_{\text{H}_2} = n \times 2 R_{\text{core}}$. The minimum column density of the 1.1 mm cores ($2.4 \times 10^{21} \text{ cm}^{-2}$) is twice larger than that of the C¹⁸O cores ($1.0 \times 10^{21} \text{ cm}^{-2}$). The column density sensitivity of the C¹⁸O data is higher than that of the 1.1 mm data. On the contrary, the mass sensitivity of the C¹⁸O data is worse than that of the 1.1 mm data as shown in Fig. 3 (b), since the mean radius R_{core} of the C¹⁸O cores is twice larger than that of the 1.1 mm dust cores. Although the column density estimation has uncertainties, there is a possibility that the C¹⁸O cores lacking 1.1 mm cores are due to the lack of the sensitivity of the column density of the 1.1 mm data. For the 81 bound C¹⁸O cores (51.9%), we speculate that the central part of the cores have not yet evolved to reach the density $> \sim 10^4 \text{ cm}^{-3}$ and are not detected in the dust continuum, as described in the beginning of this section. For the 40 unbound C¹⁸O cores, we speculate that the unbound C¹⁸O cores are transient structures created by turbulent compression and do not have high enough column density. Most of the unbound C¹⁸O cores ($\sim 70.2\%$) are in Category C and are not located on the integral-shaped filament. Here, we define the integral-shaped filament as the area having signal-to-noise ratios above 15 for the 1.1 mm flux density in the OMC 2, 3, and 4 regions for this study. Recent three-dimensional Magnetohydrodynamic (MHD) simulations have suggested that the turbulent compression creates a local dense part that is gravitationally unbound and cannot produce stars (Nakamura & Li 2011).

In Category D, there are 178 dust cores that are not associated with any C¹⁸O cores out of the 257 dust cores that were in the C¹⁸O-observed region (excluding Orion-KL). We discuss three possible origins of these cores as follows.

The first possible origin is that the C¹⁸O molecule is selectively dissociated by the FUV radiation from the massive stars in the trapezium cluster and NU Ori. The FUV intensity at the wavelengths of the dissociation lines for abundant CO decays rapidly on the surface of molecular clouds owing to very large optical depths of the FUV emission at these wavelengths (Glassgold et al. 1985; Yurimoto & Kuramoto 2004; Liszt 2007; Röllig & Ossenkopf 2013). Bethell et al. (2007) suggested that the photoionization may play a significant role at $A_{\text{v}} \sim 10$ in the case that the cores are sufficiently clumpy using a reverse Monte Carlo radiative transfer code and spectral modeling. They also mentioned that the cosmic-ray ionization is

dominant in such high A_v regions. For less abundant C^{18}O , which has shifted absorption lines owing to the difference in the vibrational-rotational energy levels, the decay of FUV is much lower. The FUV radiation can penetrate the dense region owing to the clumpiness of the cloud. Shimajiri et al. (2013) have found that the distributions of the [CI] emission coincide with those of the ^{12}CO emission in the PDRs of Orion bar, M43, and DLSF as well as the entire of the cloud, suggesting that these PDRs and the entire of the Orion A cloud have the clumpy structures (Spaans 1996; Kramer et al. 2008). For the three PDRs, the ionizing sources are the neighboring OB stars, because the 8 μm (PAH), 1.1 mm, and ^{12}CO emission are located sequentially as a function of the distance from the OB stars, i.e., the edge-on view for the OB star/PDR system (Shimajiri et al. 2011). This result suggests that these PDRs are located on the plane of the sky against OB stars. As a result, C^{18}O molecules are expected to be selectively dissociated by FUV photons even in the inner part of the cloud. It is possible that the structure of the cloud is clumpy and full of holes such that the mean extinction through the cloud from the perspective of the exciting stars is generally $A_v << 5$, even though the apparent extinction (based on the observed dust emission) is much greater. Figure 20 shows the correlation between the 1.1 mm dust and C^{18}O intensities at the position of the 1.1 mm dust cores. The 1.1 mm dust cores associated with the C^{18}O cores, which are categorized into A or B, have stronger C^{18}O intensity. The number of the 1.1 mm dust cores not associated with any C^{18}O cores (Category D) increases with decreasing C^{18}O peak intensity. Most of the 1.1 mm dust cores (56/70 cores) in the PDRs are not associated with any C^{18}O cores. Here, we defined the area of PDRs, DLSF, M43, and Regions A-D, as listed in Table 9 (also see Regions A, B, C, and D shown by Shimajiri et al. 2011). The C^{18}O intensity at the position of the 1.1 mm dust cores in the PDRs is lower than the intensity expected from the best-fit line for the 1.1 mm dust cores associated with the C^{18}O cores as shown in Fig. 20. The C^{18}O intensity at the position of several 1.1 mm dust cores not in PDRs is below the 3σ level. These dust cores are located around NGC1977 and DLSF. Thus, these cores seem to be also influenced by the FUV radiation. These facts suggest that the C^{18}O molecule is selectively dissociated by the FUV radiation in the low 1.1 mm flux density range. Shimajiri et al. (2014) found that the abundance ratio of ^{13}CO to C^{18}O , $X_{^{13}\text{CO}}/X_{\text{C}^{18}\text{O}}$, in the Orion A GMC decreases with the increasing C^{18}O column density, implying that the effect of the selective FUV dissociation of C^{18}O becomes smaller in the higher 1.1 mm flux density range where it becomes hard for the FUV radiation to penetrate owing to the dust shielding. Note that several 1.1 mm dust cores in the large 1.1 mm flux density range are categorized into D. This might be because the FUV radiation can penetrate the large 1.1 mm flux density regions owing to the clumpiness of the cloud. In fact, the $X_{^{13}\text{CO}}/X_{\text{C}^{18}\text{O}}$ value is larger than the solar system value of 5.5 even in the inner part of the cloud (Shimajiri et al. 2014). Meanwhile, Shimajiri et al. (2011) found that the ^{12}CO peak intensity range in the DLSF region is $\sim 20 - 50$ K. Especially, at the outer layers of the cloud surface in DLSF,

it increases up to 50 K. On the assumption that the ^{12}CO ($J=1-0$) line is optically thick, the result shows that the temperature is 20 – 50 K in DLSF, suggesting that the regions with bright dust but faint C^{18}O emission have dust temperatures higher than the assumed 20 K. Thus, there is a possibility that the outer layers of the cloud surface is significantly heated, driving up dust emission and (self-shielded) ^{12}CO emission, but the FUV radiation could still penetrate far enough into the unshielded C^{18}O layer to photodissociate the C^{18}O molecule without heating it.

The second possibility is the depletion of the C^{18}O molecule in the central part of the dust cores. In this case, the C^{18}O peak positions are distributed around the center positions of the dust cores. The peak positions of the C^{18}O cores disagree with those of the 1.1 mm dust cores (Ripple et al. 2013; Tatematsu et al. 2014; Ren et al. 2014).

The third possibility is contaminations from the components by ambient gas and surrounding cores. As shown in Fig. 20, many 1.1 mm dust cores are not associated with any C^{18}O cores, in spite of the fact that these C^{18}O intensities are more than 3σ and are not located in PDRs. In most cases, the C^{18}O cores and/or extended emission are distributed around the 1.1 mm dust cores categorized into D (also see Fig. 3 (b) in Shimajiri et al. 2014). There is a possibility that the C^{18}O cores associated with the 1.1 mm dust cores categorized into D are embedded in the components of other C^{18}O cores and/or extended emission and can not be extracted as cores.

3.6. Comparison among the 1.1 mm dust, 850 μm dust, H^{13}CO^+ , and N_2H^+ cores

We also compared the spatial distribution of the 1.1 mm dust cores with those of the SCUBA 850 μm dust (Nutter & Ward-Thompson 2007), H^{13}CO^+ (1–0)(Ikeda et al. 2007), and N_2H^+ (1–0) cores (Tatematsu et al. 2008). The H^{13}CO^+ and N_2H^+ emission are known as the dense gas tracers (e.g., Saito et al. 2001; Takakuwa et al. 2003; Maruta et al. 2010; Friesen et al. 2010; Johnstone et al. 2010; Tanaka et al. 2013). The angular resolution of the SCUBA 850 μm data is $14''$ (0.03 pc) and Nutter & Ward-Thompson (2007) identified the condensations having a peak flux density more than 5σ relative to the local background as cores. The H^{13}CO^+ data has an angular resolution of $21''$ (0.04 pc) and Ikeda et al. (2007) identified the H^{13}CO^+ dense cores by the Clumpfind. The N_2H^+ observations with a telescope beam size of $17''.8$ (0.03 pc) were performed with a grid spacing of $20''.55$ (0.04 pc) and Tatematsu et al. (2008) identified the N_2H^+ dense cores by eyes from the $F_1, F = 0, 1-1, 2$ component, which is an isolated component of the seven hyperfine components, and the most intense hyperfine component $F_1, F=2, 3-1, 2$. In Table 2, we summarize the SCUBA

850 μm dust, H^{13}CO^+ , and N_2H^+ cores distributed around the peaks of the 1.1 mm cores within the spatial resolution of 36''. Figures 21 – 23 show the comparison of the spatial distribution among the 1.1 mm dust, C^{18}O , 850 μm dust, H^{13}CO^+ , and N_2H^+ cores. Table 10 summarizes the comparison.

The AzTEC map excluding the Orion KL region contains 198 850 μm dust cores and 202 H^{13}CO^+ cores. The overall spatial distribution of the 1.1 mm dust cores has good agreement with that of the 850 μm dust cores. We found that 133 of the 215 850 μm dust cores (61.9%) are associated with the 1.1 mm dust cores. However, 82 850 μm dust cores (38.1%) are not detected in the 1.1 mm continuum emission, probably because of the insufficient sensitivity and beam dilution in the 1.1 mm map. The lowest mass of the dense cores detected in the SCUBA 850 μm observations is $0.13 - 0.15 M_\odot$, which is four times smaller than those detected in the 1.1 mm dust continuum observations. In addition, the angular resolution of the SCUBA 850 μm observations is 2.6 times higher than that of the 1.1 mm dust continuum observations. These facts indicate that the sensitivity of the SCUBA data is ten times higher than that of the AzTEC 1.1 mm dust continuum data. We found that 56.7% (119/210) of the H^{13}CO^+ cores are associated with the 1.1 mm dust cores. The fraction is 1.3 times higher than that for the C^{18}O cores, in spite of the fact that the mass detection limit of the H^{13}CO^+ observations is twice higher than that of the C^{18}O observations. Furthermore, the mean density of the 1.1mm dust cores ($5.5 \times 10^4 \text{ cm}^{-3}$) is closer to that of the H^{13}CO^+ cores ($1.6 \times 10^4 \text{ cm}^{-3}$) and smaller than that of the C^{18}O cores ($0.4 \times 10^4 \text{ cm}^{-3}$). Thus, the 1.1 mm dust continuum and the H^{13}CO^+ emission line are thought to trace the similar density area. These facts suggest that the H^{13}CO^+ emission is a better tracer of the dense cores than the C^{18}O emission.

In the comparison of the spatial distributions between the 1.1 mm dust and N_2H^+ cores, the high fraction of 77.8% (21/27) of the N_2H^+ cores are found to be associated with the 1.1 mm dust cores. Such a high fraction implies that both the N_2H^+ and H^{13}CO^+ emission can trace well the dense cores compared to the C^{18}O emission. The remaining six N_2H^+ cores are not associated with any 1.1 mm dust cores probably owing to the insufficient spatial resolution of the 1.1 mm map. In fact, the six cores are located in the extended feature in the 1.1 mm map, and are associated with the SCUBA 850 μm dust cores. We note that the number of the N_2H^+ cores is the smallest and the lowest mass of the detected N_2H^+ cores is $7.3 M_\odot$, which is much larger than those of the 1.1 mm, 850 μm , and H^{13}CO^+ cores.

4. Summary

The main results of this study are summarized as follows:

1. We have cataloged 619 dust cores in the AzTEC 1.1 mm dust continuum using the Clumpfind method. The ranges of the radius R_{core} , mass M_{H_2} , and density n of these cores are estimated to be 0.01–0.2 pc, $0.6 - 1.2 \times 10^2 M_{\odot}$, and $0.3 \times 10^4 - 9.2 \times 10^6 \text{ cm}^{-3}$, respectively. The high-mass cores ($M_{\text{H}_2} \geq 10.0 M_{\odot}$) are located in the integral-shaped filament. On the other hand, the intermediate-mass ($1.0 M_{\odot} \leq M_{\text{H}_2} < 10.0 M_{\odot}$) and low-mass ($M_{\text{H}_2} < 1.0 M_{\odot}$) cores are mainly located on the outside of the filament.
2. The distribution of the C¹⁸O ($J=1-0$) emission is similar to that of the 1.1 mm dust continuum emission. We have identified 235 C¹⁸O cores from the C¹⁸O data by the Clumpfind algorithm. The ranges of R_{core} , dV_{core} , M_{LTE} , and n are 0.13 – 0.34 pc, $0.31 - 1.31 \text{ km s}^{-1}$, $1.0 - 61.8 M_{\odot}$, and $(0.8 - 17.5) \times 10^3 \text{ cm}^{-3}$, respectively. In the 235 C¹⁸O cores, 61 cores are gravitationally unbound, while 174 cores are gravitationally bound.
3. We performed the core identification with various step sizes and threshold levels in a reasonable range of 2σ to 5σ in order to investigate the influence of the Clumpfind parameters on the core properties. The number of the identified C¹⁸O cores significantly decreases with increasing step size, while the core number weakly depends on the threshold level. The R_{core} , dV_{core} , and M_{LTE} values gradually increase with increasing step size, but do not depend on the threshold level.
4. The LTE mass vs. virial ratio and density vs. virial ratio relations of the identified C¹⁸O cores show that the virial ratio tends to decrease with the increasing LTE mass and density. The best-fit power-law functions for the unbound and bound cores are $(M_{\text{LTE}}/M_{\odot}) = (58.2 \pm 27.3)(R_{\text{core}}/\text{pc})^{1.7 \pm 0.3}$ and $(M_{\text{LTE}}/M_{\odot}) = (325.9 \pm 130.4)(R_{\text{core}}/\text{pc})^{2.1 \pm 0.3}$, respectively. The coefficient for the bound cores is significantly larger than for the unbound cores. The difference between the data distributions for the unbound and bound cores cannot be seen in the dV vs. R_{core} relation.
5. We compared the physical properties of the C¹⁸O cores among the OMC-1, OMC-2/3, OMC-4, DSLF, and bending structure regions. The Kolmogorov-Smirnov (KS) test showed that there is no significant difference among the five regions for each property, although the physical environments in the regions are very different from each other.
6. We investigated the dynamical states of the C¹⁸O cores with the external pressure and internal magnetic field. We found that all the bound C¹⁸O cores are supercritical ($\mathcal{R}_{\text{c}} \geq 1$) and 25 of the 61 unbound C¹⁸O cores are subcritical ($\mathcal{R}_{\text{c}} < 1$), although there are large uncertainties in the estimation of the Jeans mass owing to the relation of $M_J \propto \sigma^4$.

7. We examined the spatial relations between the 1.1 mm dust and C¹⁸O cores. We found that the relations can be categorized into the following four groups. First, one C¹⁸O core is associated with one 1.1 mm dust core. Second, two or more C¹⁸O cores are associated with one dust core. Third, there are isolated C¹⁸O cores which are not associated with any dust core. Fourth, 1.1 mm dust cores not associated with any C¹⁸O cores also exist.
8. We compared the spatial distributions of the 1.1 mm dust, 850 μ m dust, C¹⁸O, H¹³CO⁺, and N₂H⁺ cores. The overall distribution of the 1.1 mm dust cores is found to have good agreement with that of the 850 μ m dust cores. In addition, the N₂H⁺ and H¹³CO⁺ emission are found to trace well the dense dust cores compared to the C¹⁸O emission.

We acknowledge the anonymous referee for providing helpful suggestions to improve this paper. Y. Shimajiri was financially supported by a Research Fellowship from the JSPS for Young Scientists. This work was supported by JSPS KAKENHI Grant Number 90610551. Part of this work was supported by the French National Research Agency (Grant no. ANR11BS560010STARFICH). K. S., T. S., and F. N., were supported by JSPS KAKENHI Grant Numbers, 26287030, 26610045, 26350186, and 24244017. M. M., and T. T., were supported by MEXT KAKENHI No. 23103004.

Facilities: ASTE (AzTEC), Nobeyama 45m (BEARS).

REFERENCES

- Bally, J., Lanber, W. D., Stark, A. A., & Wilson, R. W. 1987, ApJ, 312, L45
- Bally, J., Cunningham, N. J., Moeckel, N., et al. 2011, ApJ, 727, 113
- Belloche, A., Schuller, F., Parise, B., et al. 2011, A&A, 527, A145
- Bergin, E. A., Alves, J., Huard, T., & Lada, C. J. 2002, ApJ, 570, L101
- Bethell, T. J., Zweibel, E. G., & Li, P. S. 2007, ApJ, 667, 275
- Buckle, J. V., Davis, C. J., Francesco, J. D., et al. 2012, MNRAS, 422, 521
- Cesaroni, R., & Wilson, T. L. 1994, A&A, 281, 209
- Chini, R., Reipurth, B., Ward-Thompson, D., et al. 1997, ApJ, 474, L135

- Cohen, M., & Kuhi, L. V. 1979, ApJS, 41, 743
- Crutcher, R. M., Troland, T. H., Lazareff, B., Paubert, G., & Kazès, I. 1999, ApJ, 514, L121
- Davis, C. J., Froebrich, D., Stanke, T., et al. 2009, A&A, 496, 153
- Dobashi, K., Bernard, J.-P., & Fukui, Y. 1996, ApJ, 466, 282
- Dobashi, K., Uehara, H., Kandori, R., et al. 2005, PASJ, 57, 1
- Dzib, S. A., Loinard, L., Mioduszewski, A. J., et al. 2013, ApJ, 775, 63
- Frerking, M. A., Langer, W. D., & Wilson, R. W. 1982, ApJ, 262, 590
- Friesen, R. K., Di Francesco, J., Shimajiri, Y., & Takakuwa, S. 2010, ApJ, 708, 1002
- Furuya, R. S., & Shinnaga, H. 2009, ApJ, 703, 1198
- Glassgold, A. E., Huggins, P. J., & Langer, W. D. 1985, ApJ, 290, 615
- Hildebrand, R. H. 1983, QJRAS, 24, 267
- Hirota, T., Ando, K., Bushimata, T., et al. 2008, PASJ, 60, 961
- Ikeda, N., Sunada, K., & Kitamura, Y. 2007, ApJ, 665, 1194
- Ikeda, N., & Kitamura, Y. 2009, ApJ, 705, L95
- Ikeda, N., & Kitamura, Y. 2011, ApJ, 732, 101
- Johnstone, D., & Bally, J. 1999, ApJ, 510, L49
- Johnstone, D., Matthews, H., & Mitchell, G. F. 2006, ApJ, 639, 259
- Johnstone, D., Rosolowsky, E., Tafalla, M., & Kirk, H. 2010, ApJ, 711, 655
- Kauffmann, J., Bertoldi, F., Bourke, T. L., Evans, N. J., II, & Lee, C. W. 2008, A&A, 487, 993
- Kramer, C., Cubick, M., Röllig, M., et al. 2008, A&A, 477, 547
- Kirk, H., Johnstone, D., & Di Francesco, J. 2006, ApJ, 646, 1009
- Lee, K., Looney, L. W., Schnee, S., & Li, Z.-Y. 2013, ApJ, 772, 100
- Li, D., Kauffmann, J., Zhang, Q., & Chen, W. 2013, ApJ, 768, L5

- Liu, T., Wu, Y., & Zhang, H. 2012, ApJS, 202, 4
- Liszt, H. S. 2007, A&A, 476, 291
- Maruta, H., Nakamura, F., Nishi, R., Ikeda, N., & Kitamura, Y. 2010, ApJ, 714, 680
- Mardones, D., Myers, P. C., Tafalla, M., et al. 1997, ApJ, 489, 719
- McKee, C. F., & Zweibel, E. G. 1992, ApJ, 399, 551
- Megeath, S. T., Gutermuth, R., Muzeirole, J., et al. 2012, AJ, 144, 192
- Menten, K. M., Reid, M. J., Forbrich, J., & Brunthaler, A. 2007, A&A, 474, 515
- Motte, F., Andre, P., & Neri, R. 1998, A&A, 336, 150
- Myers, P. C., Bachiller, R., Caselli, P., et al. 1995, ApJ, 449, L65
- Nakamura, F., & Li, Z.-Y. 2011, ApJ, 740, 36
- Nakamura, F., Miura, T., Kitamura, Y., et al. 2012, ApJ, 746, 25
- Nagahama, T., Mizuno, A., Ogawa, H., & Fukui, Y. 1998, AJ, 116, 336
- Nutter, D., & Ward-Thompson, D. 2007, MNRAS, 374, 1413
- Ohashi, N., Hayashi, M., Ho, P. T. P., et al. 1997, ApJ, 488, 317
- Onishi, T., Mizuno, A., Kawamura, A., Tachihara, K., & Fukui, Y. 2002, ApJ, 575, 950
- Pineda, J. E., Rosolowsky, E. W., & Goodman, A. A. 2009, ApJ, 699, L134
- Polychroni, D., Schisano, E., Elia, D., et al. 2013, ApJ, 777, L33
- Rathborne, J. M., Lada, C. J., Muench, A. A., et al. 2009, ApJ, 699, 742
- Ren, Z., Li, D., & Chapman, N. 2014, ApJ, 788, 172
- Ripple, F., Heyer, M. H., Gutermuth, R., Snell, R. L., & Brunt, C. M. 2013, MNRAS, 431, 1296
- Rodríguez-Franco, A., Wilson, T. L., Martín-Pintado, J., & Fuente, A. 2001, ApJ, 559, 985
- Röllig, M., & Ossenkopf, V. 2013, A&A, 550, AA56
- Sánchez-Monge, Á., Palau, A., Fontani, F., et al. 2013, MNRAS, 432, 3288

- Sandstrom, K. M., Peek, J. E. G., Bower, G. C., Bolatto, A. D., & Plambeck, R. L. 2007, ApJ, 667, 1161
- Saito, M., Kawabe, R., Kitamura, Y., & Sunada, K. 2001, ApJ, 547, 840
- Shimajiri, Y., Takahashi, S., Takakuwa, S., Saito, M., & Kawabe, R. 2008, ApJ, 683, 255
- Shimajiri, Y., Takahashi, S., Takakuwa, S., Saito, M., & Kawabe, R. 2009, PASJ, 61, 1055
- Shimajiri, Y., Kawabe, R., Takakuwa, S., et al. 2011, PASJ, 63, 105
- Shimajiri, Y., Sakai, T., Tsukagoshi, T., et al. 2013, ApJ, 774, L20
- Shimajiri, Y., Kitamura, Y., Saito, M., et al. 2014, A&A, 564, A68
- Spaans, M. 1996, A&A, 307, 271
- Stanke, T., & Williams, J. P. 2007, AJ, 133, 1307
- Tachihara, K., Onishi, T., Mizuno, A., & Fukui, Y. 2002, A&A, 385, 909
- Tafalla, M., Myers, P. C., Caselli, P., Walmsley, C. M., & Comito, C. 2002, ApJ, 569, 815
- Takakuwa, S., Kamazaki, T., Saito, M., & Hirano, N. 2003, ApJ, 584, 818
- Takahashi, S., Saito, M., Takakuwa, S., & Kawabe, R. 2006, ApJ, 651, 933
- Takahashi, S., Saito, M., Ohashi, N., et al. 2008, ApJ, 688, 344
- Takahashi, S., Ho, P. T. P., Tang, Y.-W., Kawabe, R., & Saito, M. 2009, ApJ, 704, 1459
- Takahashi, S., & Ho, P. T. P. 2012, ApJ, 745, L10
- Takahashi, S., Ho, P. T. P., Teixeira, P. S., Zapata, L. A., & Su, Y.-N. 2013, ApJ, 763, 57
- Tanaka, T., Nakamura, F., Awazu, Y., et al. 2013, ApJ, 778, 34
- Tatematsu, K., Umemoto, T., Kameya, O., et al. 1993, ApJ, 404, 643
- Tatematsu, K., Umemoto, T., Heyer, M. H., et al. 1998, ApJS, 118, 517
- Tatematsu, K., Kandori, R., Umemoto, T., & Sekimoto, Y. 2008, PASJ, 60, 407
- Tatematsu, K., Ohashi, S., Umemoto, T., et al. 2014, PASJ, 66, 16
- Tomisaka, K., Ikeuchi, S., & Nakamura, T. 1988, ApJ, 335, 239

- Wall, J. V., & Jenkins, C. R. 2012, Practical Statistics for Astronomers, by J. V. Wall , C. R. Jenkins, Cambridge, UK: Cambridge University Press, 2012,
- Williams, J. P., de Geus, E. J., & Blitz, L. 1994, ApJ, 428, 693
- Williams, M. J., Bureau, M., & Cappellari, M. 2010, MNRAS, 409, 1330
- Yonekura, Y., Dobashi, K., Mizuno, A., Ogawa, H., & Fukui, Y. 1997, ApJS, 110, 21
- Yurimoto, H., & Kuramoto, K. 2004, Science, 305, 1763

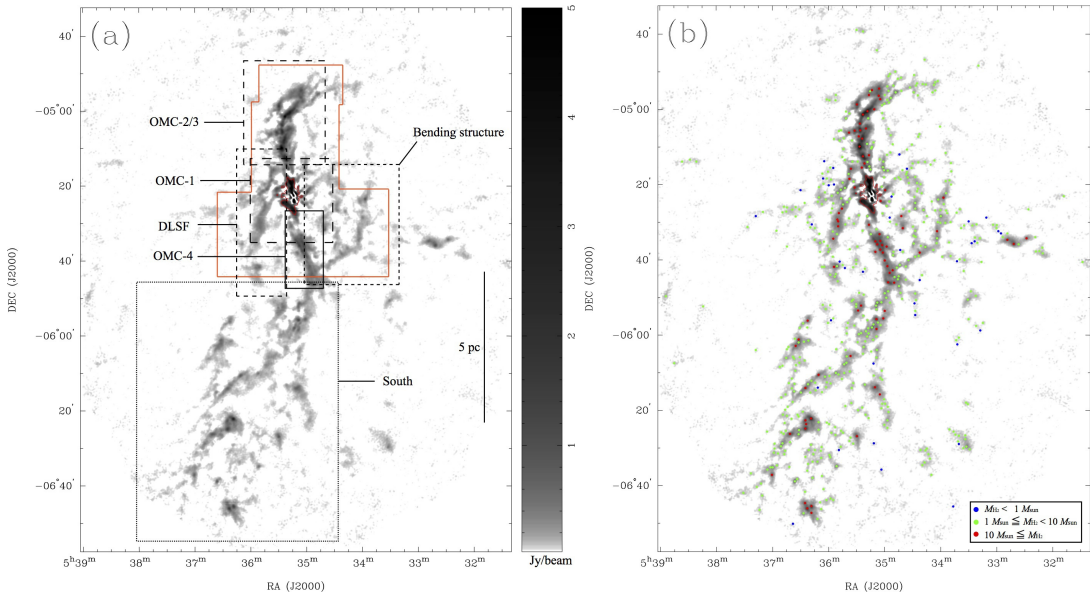


Fig. 1.— (a) AzTEC 1.1 mm dust continuum emission map of the Orion A GMC in gray scale. The five distinct regions of the OMC-1, OMC-2/3, OMC-4, DLSF, bending structure, and south regions are indicated by the boxes with different black broken lines, corresponding to the regions shown in Figs 12 – 17. The 1.1 mm emission around the central Orion-KL region could not be reconstructed as an accurate structure with the AzTEC data-reduction technique, because the continuum emission around Orion-KL is too bright. The red polygon shows the region mapped in C^{18}O ($J=1-0$). The linear scale of 1 pc is shown on the right side. (b) The identified dust cores in the AzTEC 1.1 mm map. The red, green, and blue filled circles show the positions of the dust cores with masses of $\geq 10 M_{\odot}$, $1 - 10 M_{\odot}$, and $< 1 M_{\odot}$, respectively (see also Fig 3.).

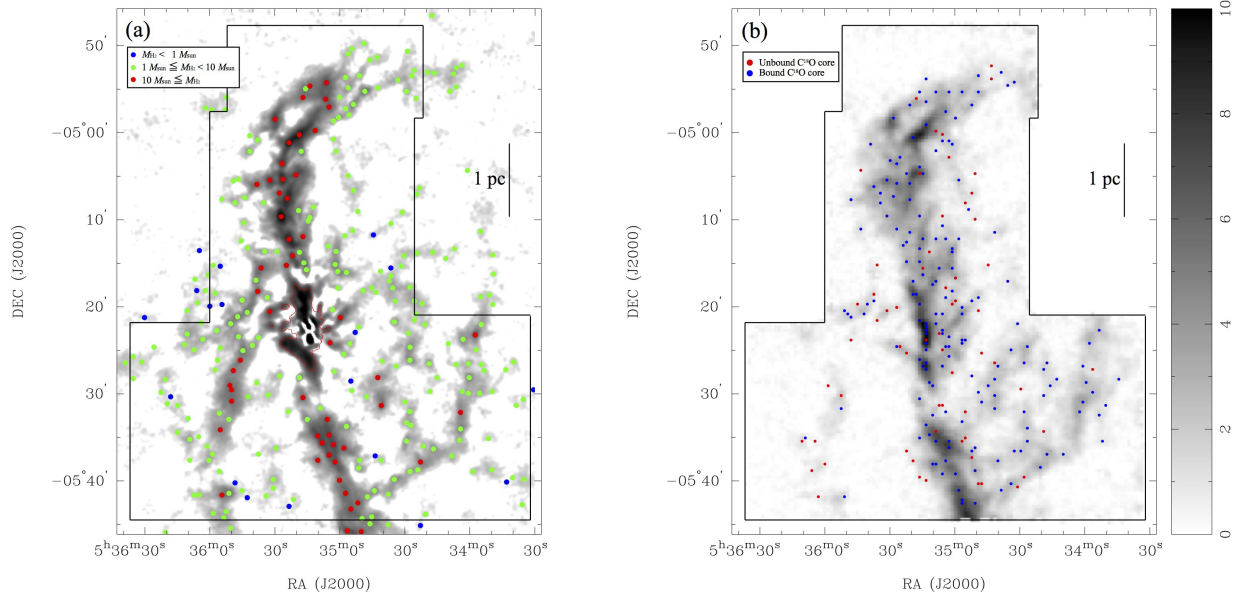


Fig. 2.— (a) Close-up view of the upper half of Fig. 1 (b). The black polygon shows the the area mapped in C¹⁸O. (b) Positions of the identified C¹⁸O cores shown on the integrated intensity map (gray scale). The blue and red filled circles correspond to gravitationally bound and unbound cores, respectively. The gray scale bar on the right side of the panel is for the C¹⁸O intensity in K km s⁻¹.

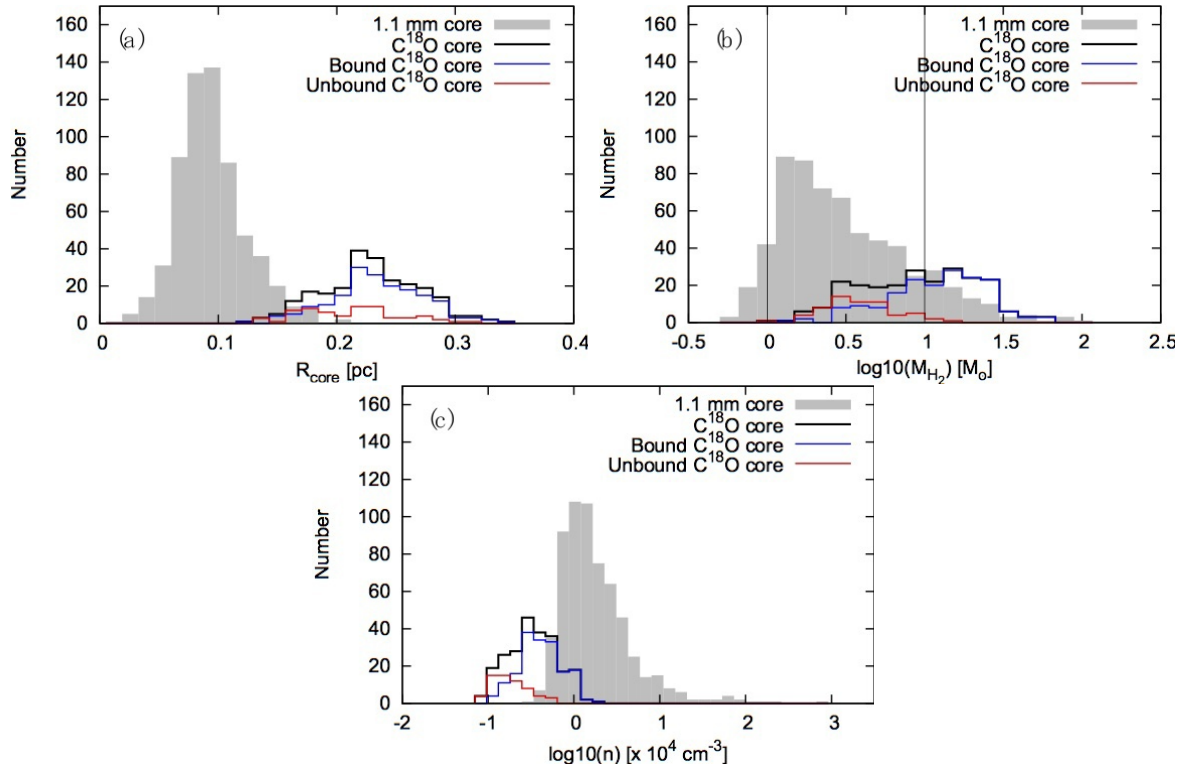


Fig. 3.— Histograms of (a) the radius R_{core} of the 1.1 mm dust and C^{18}O cores, (b) the mass M_{H_2} , and (c) the density n . The gray boxes show the 1.1 mm dust cores, and the black, blue, and red lines correspond to all the C^{18}O cores, the gravitationally bound C^{18}O ones, and the unbound C^{18}O ones, respectively. In panel (b), the vertical black broken lines indicate $M_{\text{H}_2}=1$ and $10 M_{\odot}$.

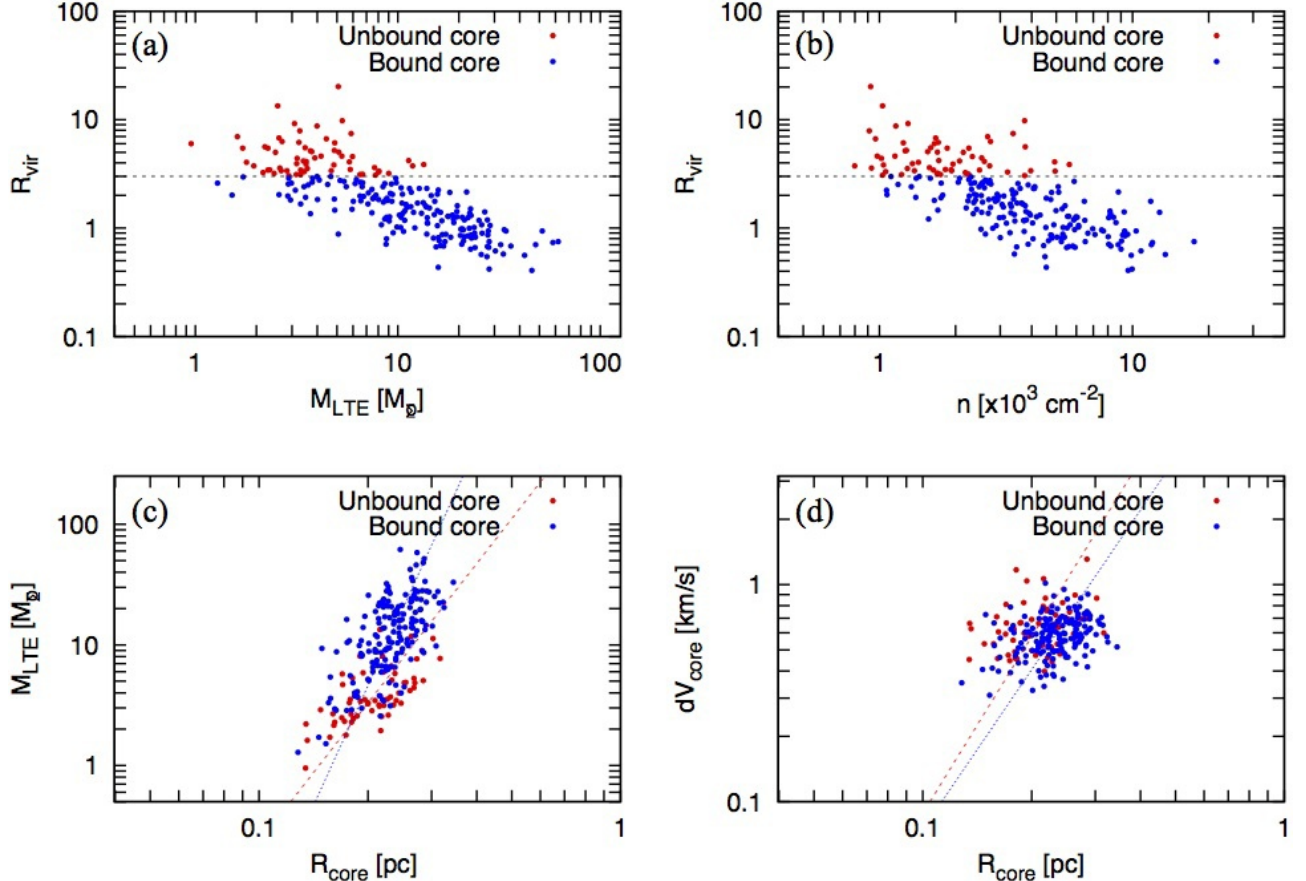


Fig. 4.— The relations of the (a) \mathcal{R}_{vir} vs. M_{LTE} , (b) \mathcal{R}_{vir} vs. n , (c) M_{LTE} vs. R_{core} , and (d) dV_{core} vs. R_{core} of the C¹⁸O cores. We assume that the cores with $\mathcal{R}_{\text{vir}} < 3.0$ are under virial equilibrium by considering the uncertainty in $X_{\text{C}^{18}\text{O}}$ of a factor 3. The black broken lines in panels (a) and (b) show $\mathcal{R}_{\text{vir}} = 3.0$. The red and blue filled circles represent the unbound ($\mathcal{R}_{\text{vir}} \geq 3.0$) and bound ($\mathcal{R}_{\text{vir}} < 3.0$) cores, respectively. The red and blue broken lines in the bottom panels show the best-fit power-law functions for the unbound and bound cores, respectively.

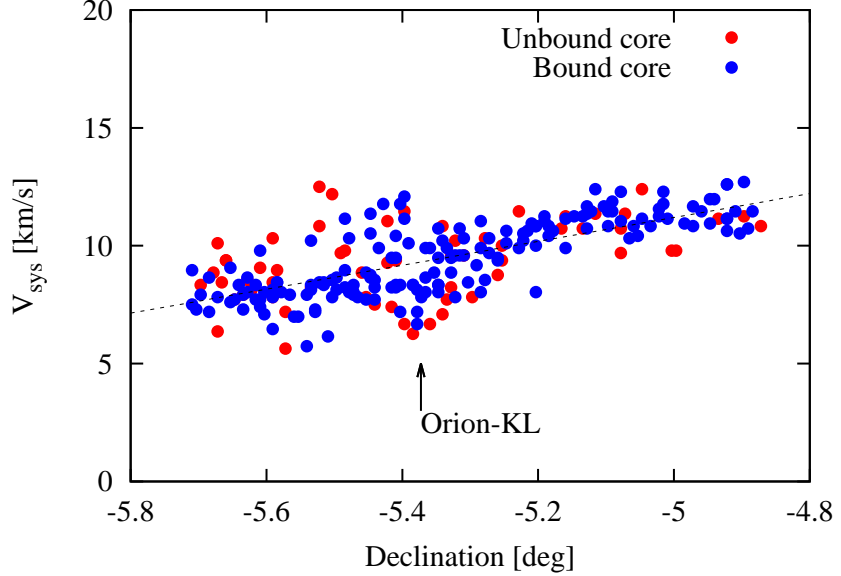


Fig. 5.— The V_{sys} vs. Dec. relation of the C^{18}O cores. The red and blue filled circles show the unbound ($\mathcal{R}_{\text{vir}} \geq 3.0$) and bound ($\mathcal{R}_{\text{vir}} < 3.0$) cores, respectively. The black broken line shows the linear function for all the cores. The vertical arrow shows the position of Orion-KL.

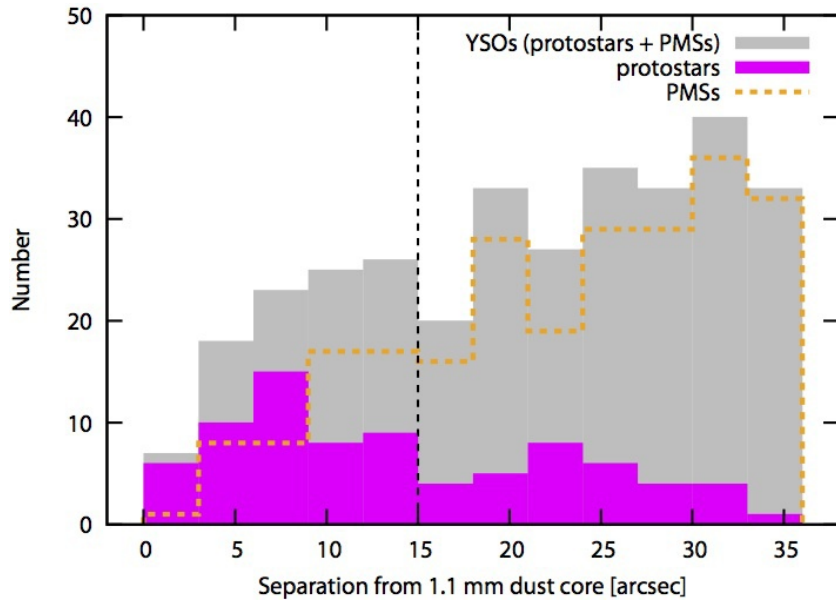


Fig. 6.— Histogram of the separations between the AzTEC 1.1 mm dust cores and YSOs.

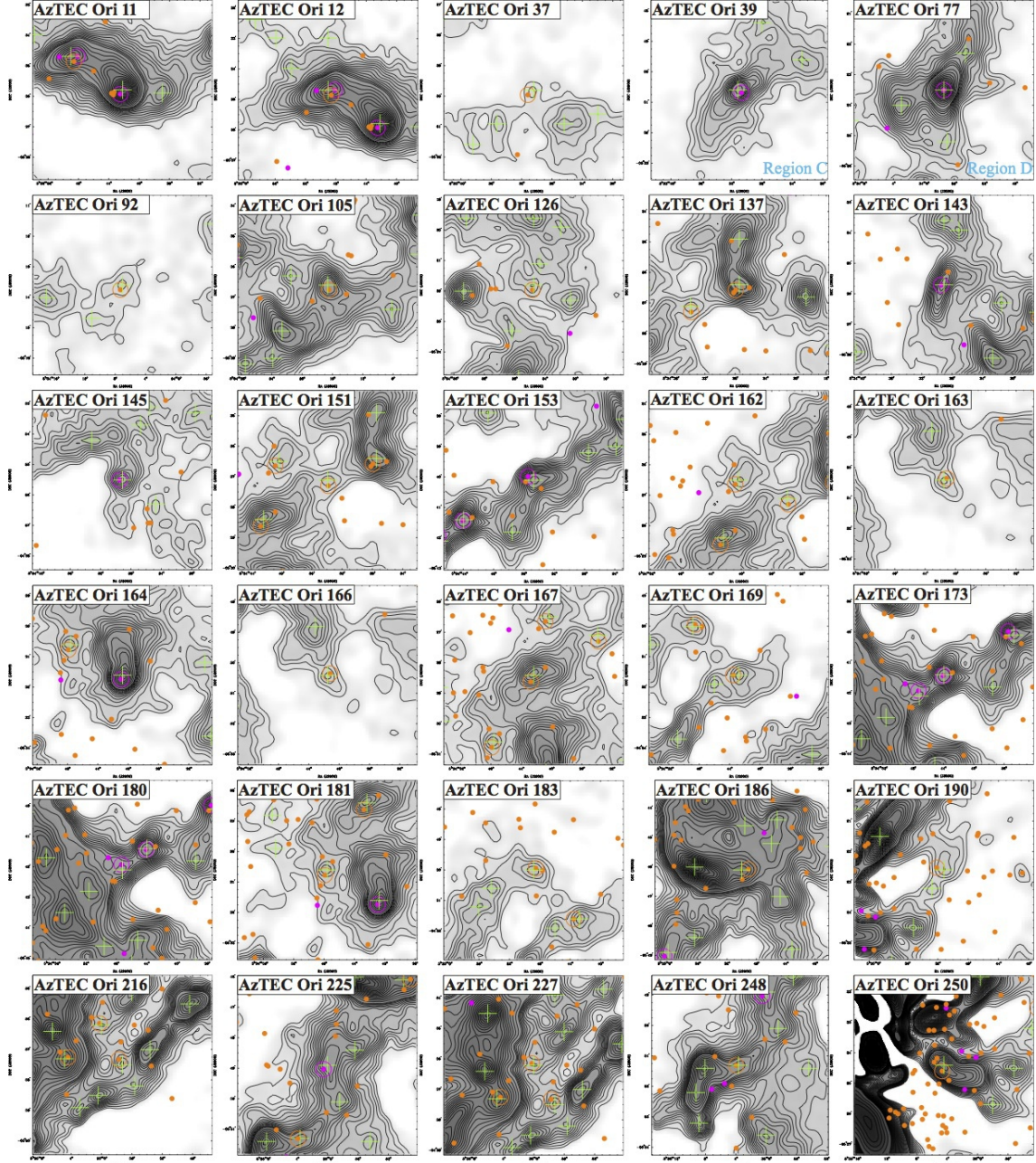


Fig. 7.— Close-up 1.1 mm continuum images of the dust cores associated with protostars and pre-main sequence stars. The green plus signs denote the peak positions of the identified 1.1 mm dust cores, and the ID number of the central core is shown at the top of each panel. The labels in light blue show the source names used in other studies (Chini et al. 1997; Stanke & Williams 2007; Shimajiri et al. 2011). In each panel, the contours start from the 4σ level with an intervals of 2σ for the range of $4 - 30\sigma$, 5σ for the range of $30 - 305\sigma$, and 50σ for the range $> 305\sigma$. The magenta and orange open circles indicate the positions of the Spitzer protostars and pre-main sequence stars, respectively (Megeath et al. 2012), associated with the 1.1 mm dust cores. The magenta and orange small filled circles show the positions of the other protostars and pre-main sequence stars, respectively.

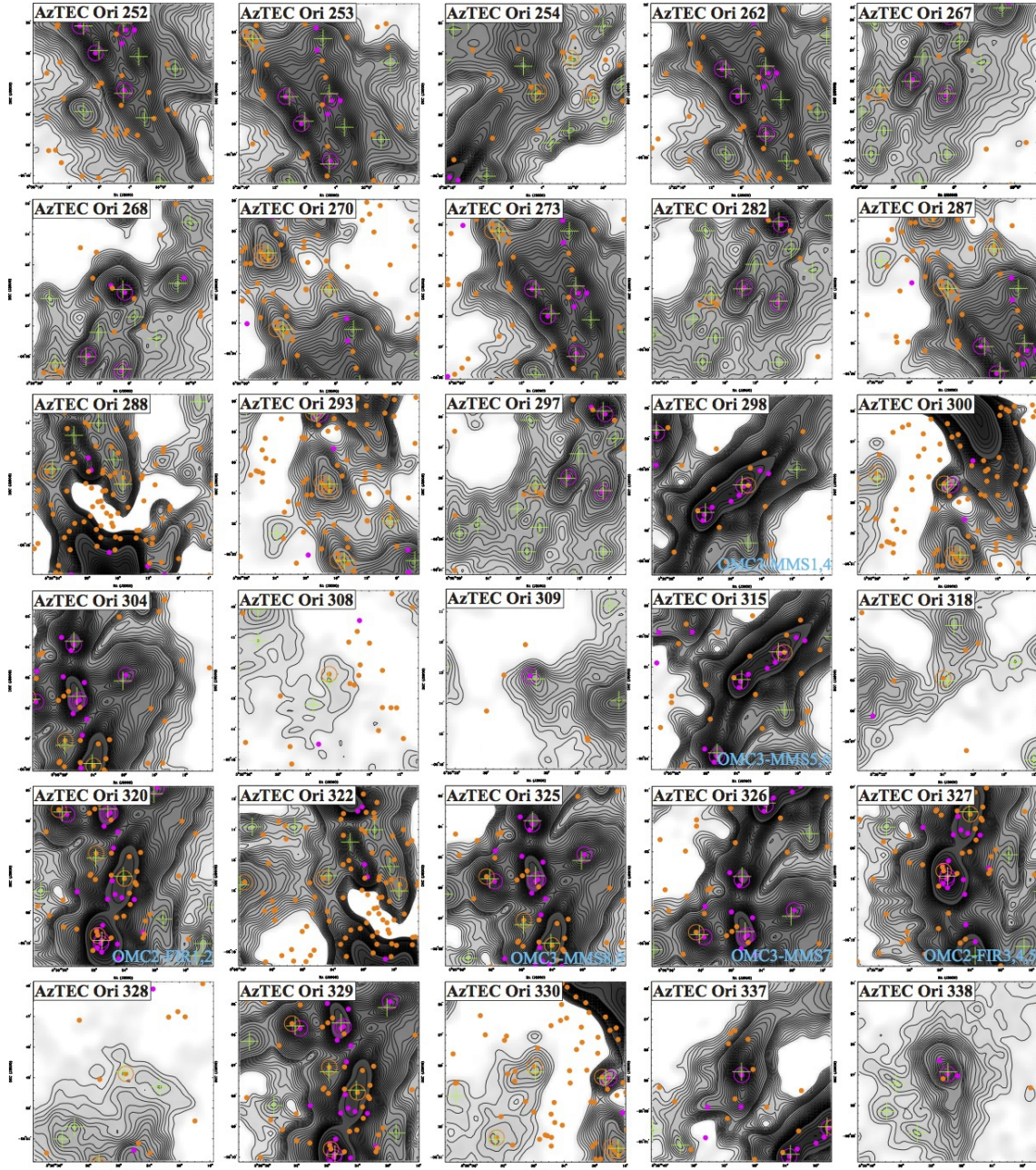


Fig. 8.— Continuation of Fig. 7.

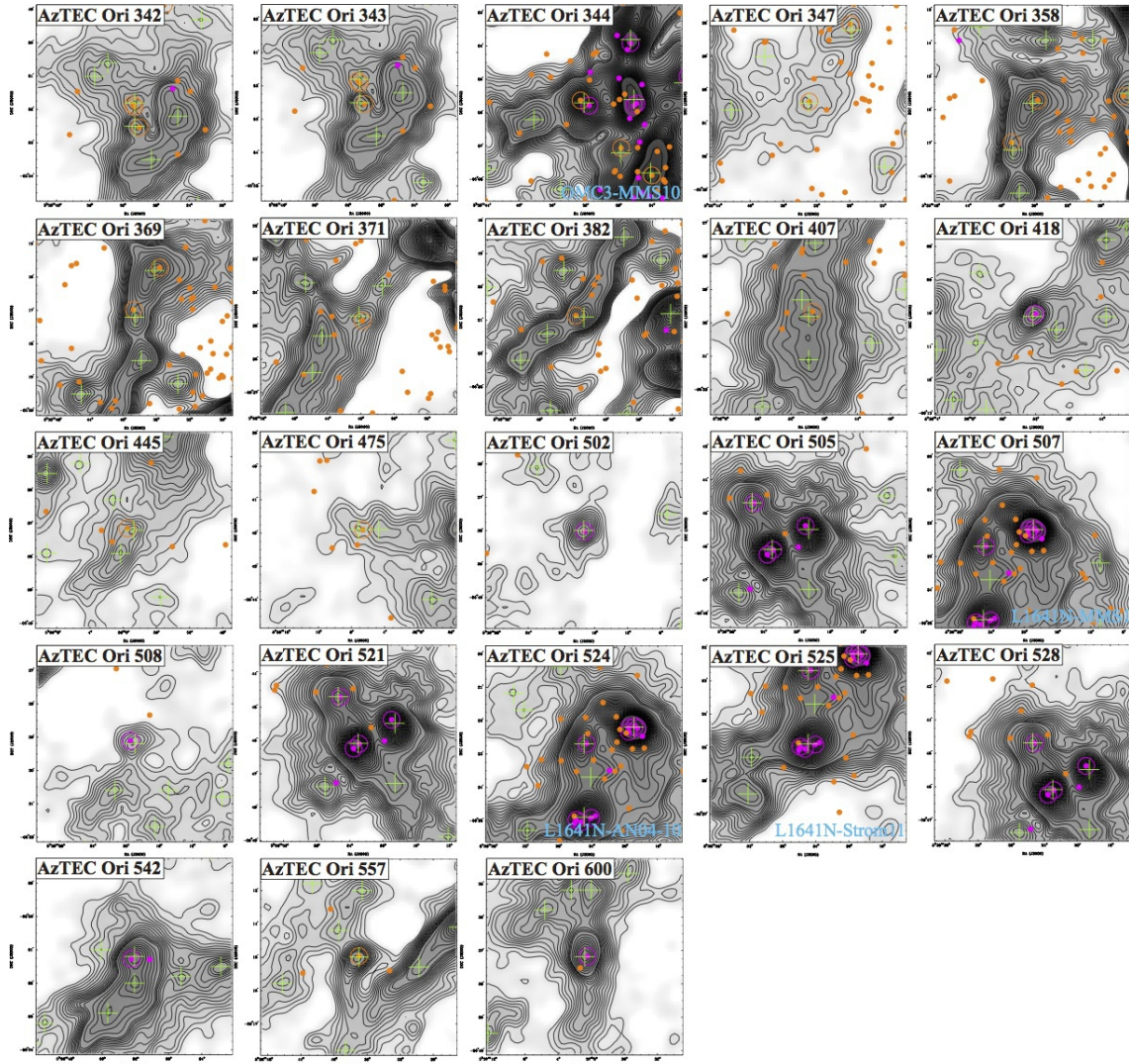


Fig. 9.— Continuation of Fig. 7.

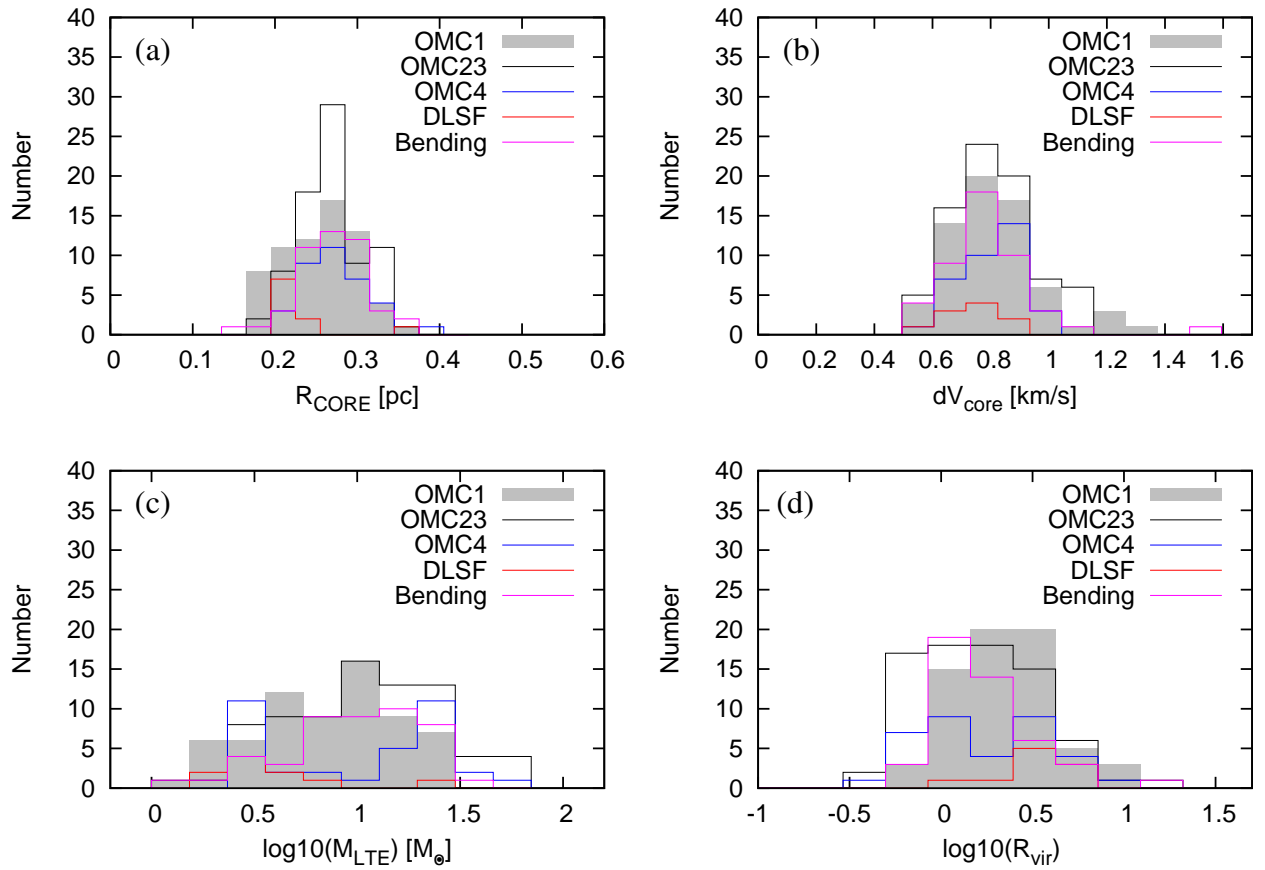


Fig. 10.— Histograms of (a) R_{core} , (b) dV_{core} , (c) M_{LTE} , and (d) R_{vir} of the C^{18}O cores in the OMC-1, OMC-2/3, OMC-4, DLSF, and bending structure regions shown by the gray, black, blue, red, and magenta lines, respectively.

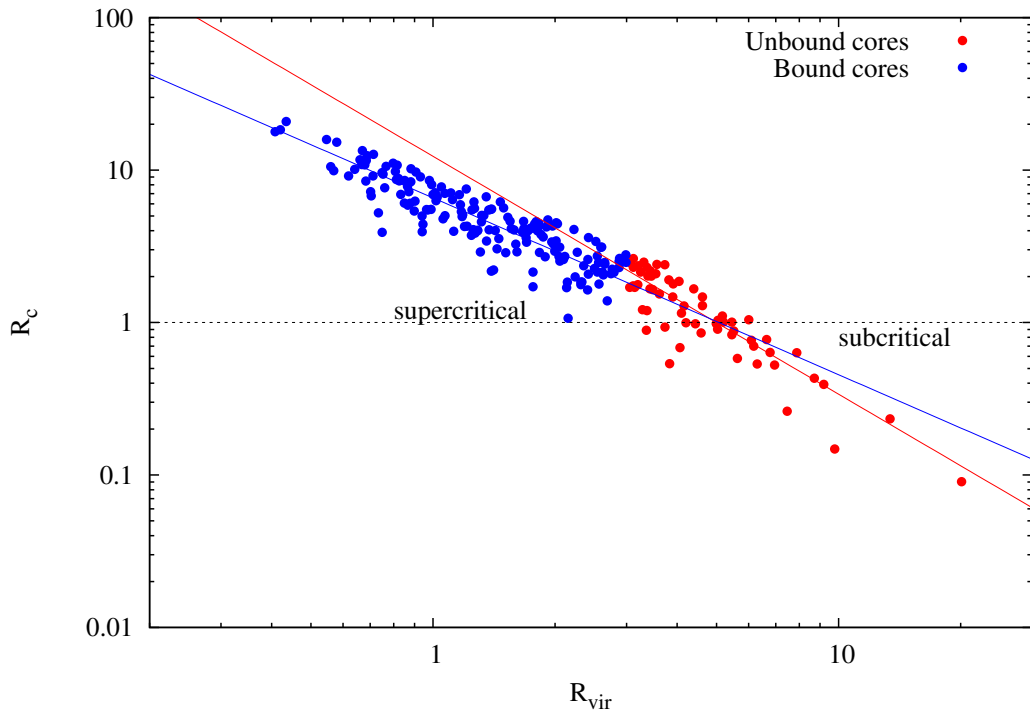


Fig. 11.— The \mathcal{R}_c vs. \mathcal{R}_{vir} relation of the C^{18}O cores. The red and blue filled circles show the unbound ($\mathcal{R}_{\text{vir}} \geq 3.0$) and bound ($\mathcal{R}_{\text{vir}} < 3.0$) cores, respectively. The red and blue lines show the best-fit power-law functions for the unbound and bound cores, respectively. The horizontal black broken line denotes $\mathcal{R}_c = 1$.

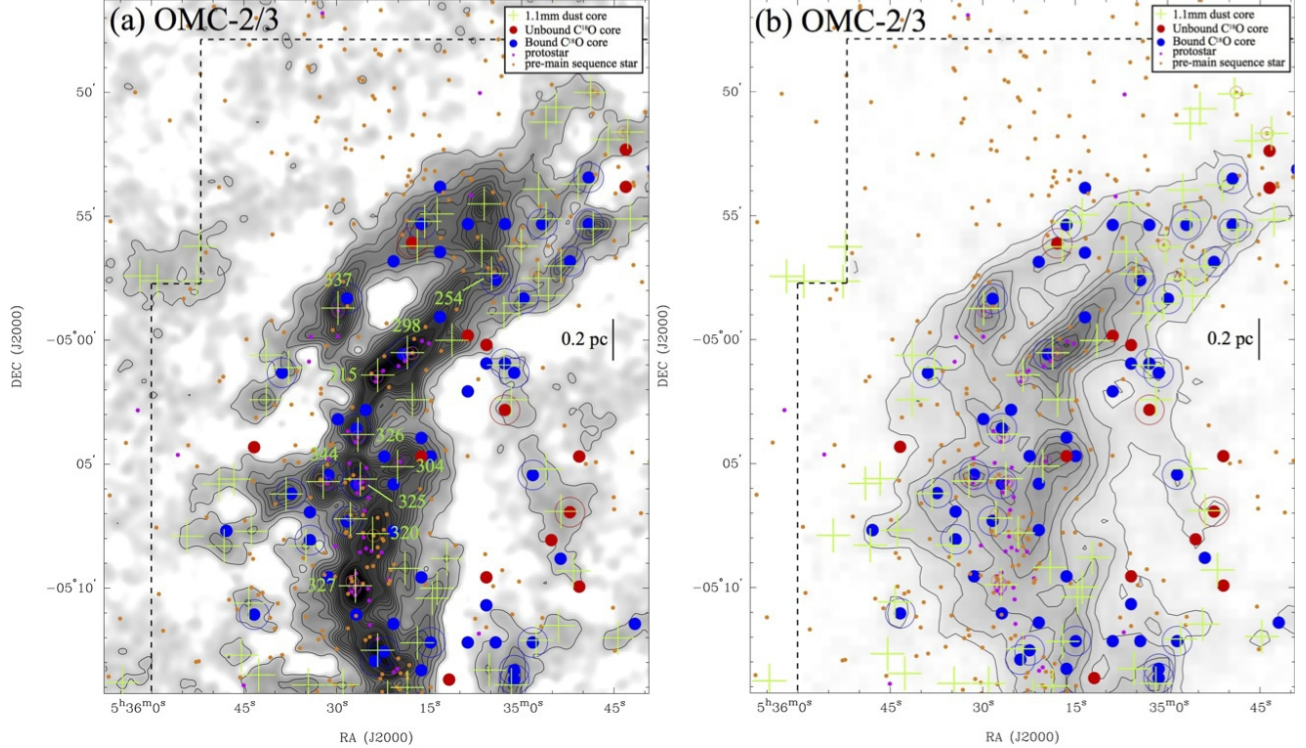


Fig. 12.— Our identified 1.1 mm dust and C¹⁸O cores on (a) the AzTEC 1.1 mm and (b) the C¹⁸O integrated intensity maps of the OMC-2/3 region. The green plus signs denote the positions of the 1.1 mm dust cores. The red and blue filled circles show the positions of the bound ($\mathcal{R}_{\text{vir}} < 3$) and unbound ($\mathcal{R}_{\text{vir}} \geq 3$) C¹⁸O cores, respectively. The red and blue open circles show the C¹⁸O cores associated with the 1.1 mm dust cores. The numbers labeled in green are the ID numbers of the AzTEC cores associated with the YSOs shown in Figs. 7–9. The magenta and orange open circles show the positions of the Spitzer protostars and pre-main sequence stars (Megeath et al. 2012), respectively, associated with the 1.1 mm dust cores. The magenta and orange filled circles show the positions of the other Spitzer sources. In panel (a), the contours start from the 5 σ level with an interval of 10 σ for the range of 5 - 105 σ and 50 σ for the range $> 105\sigma$. The black dashed lines indicate the C¹⁸O mapping area. In panel (b), the contours start 1 K km s⁻¹ with an interval of 1 K km s⁻¹.

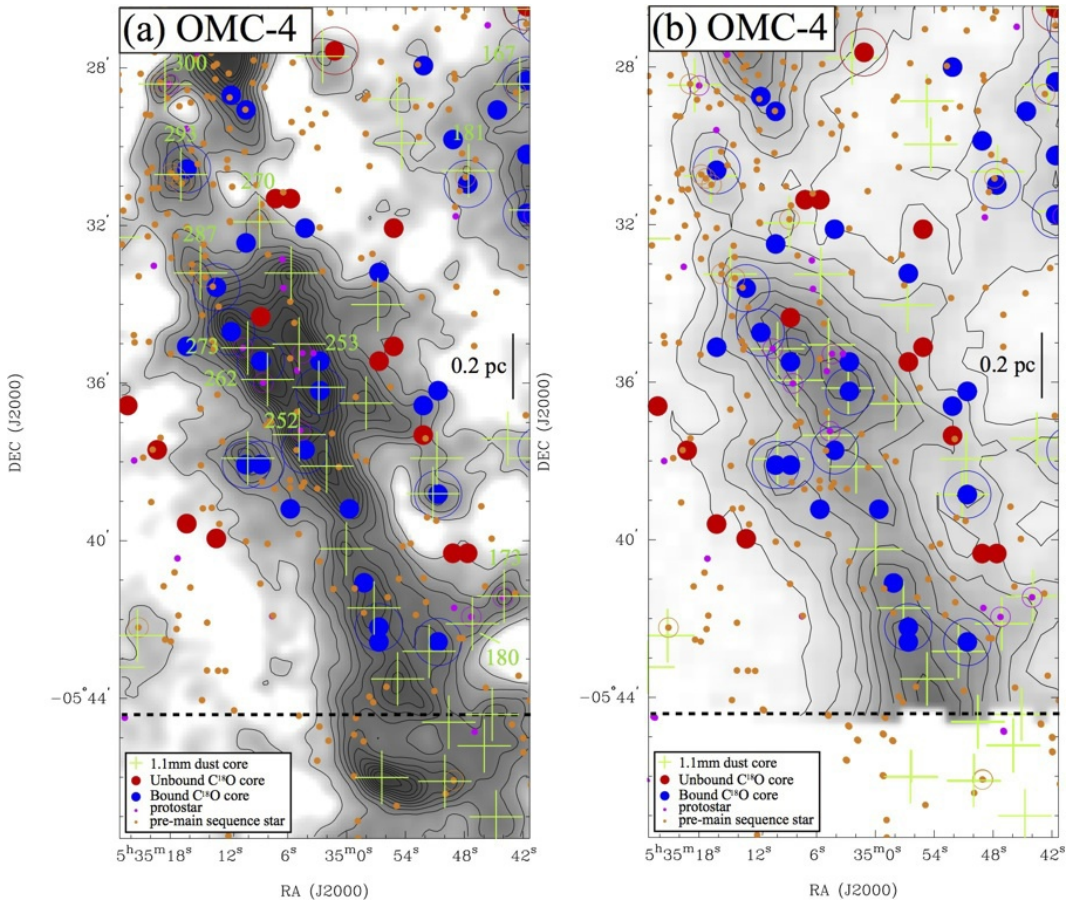


Fig. 13.— Same as Fig. 12, but for the OMC-4 region.

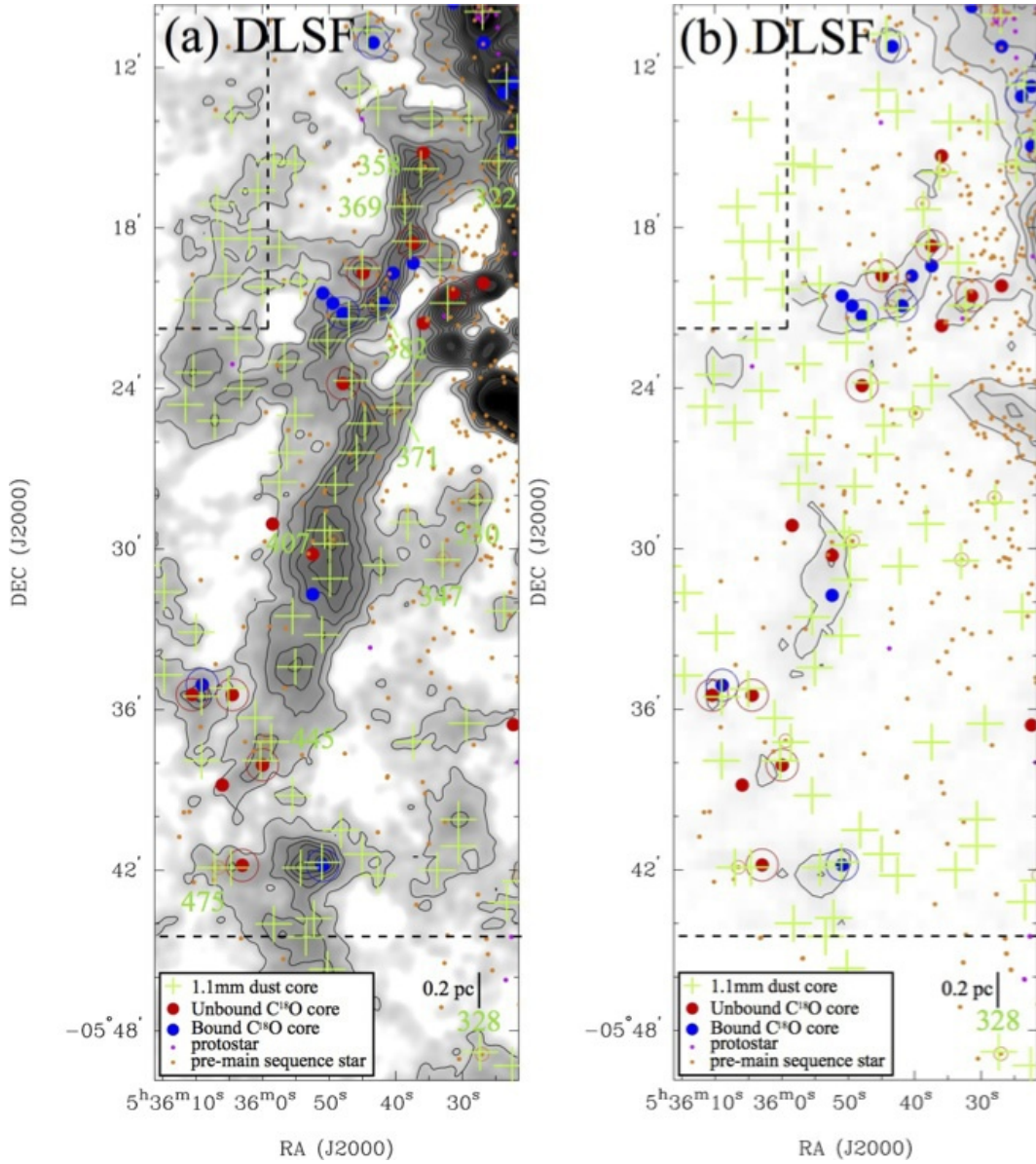


Fig. 14.— Same as Fig. 12, but for the DLSF region.

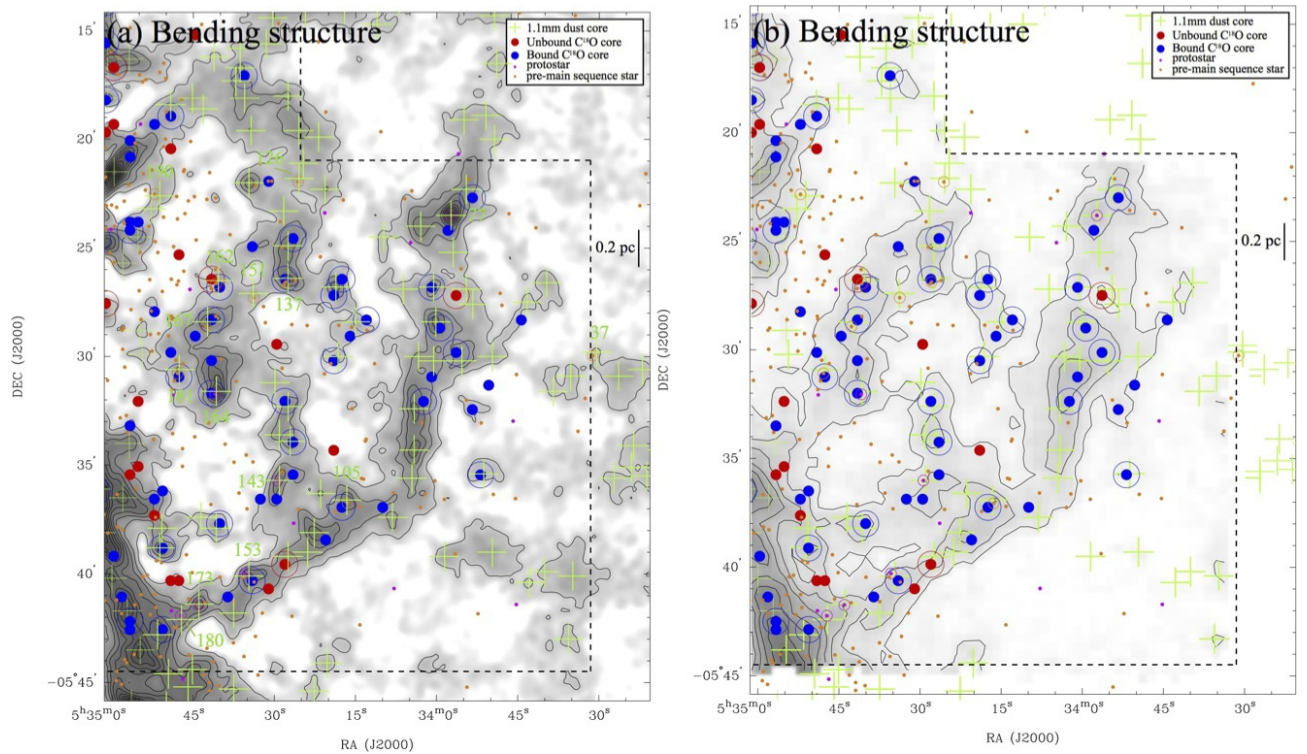


Fig. 15.— Same as Fig. 12, but for the bending structure region.

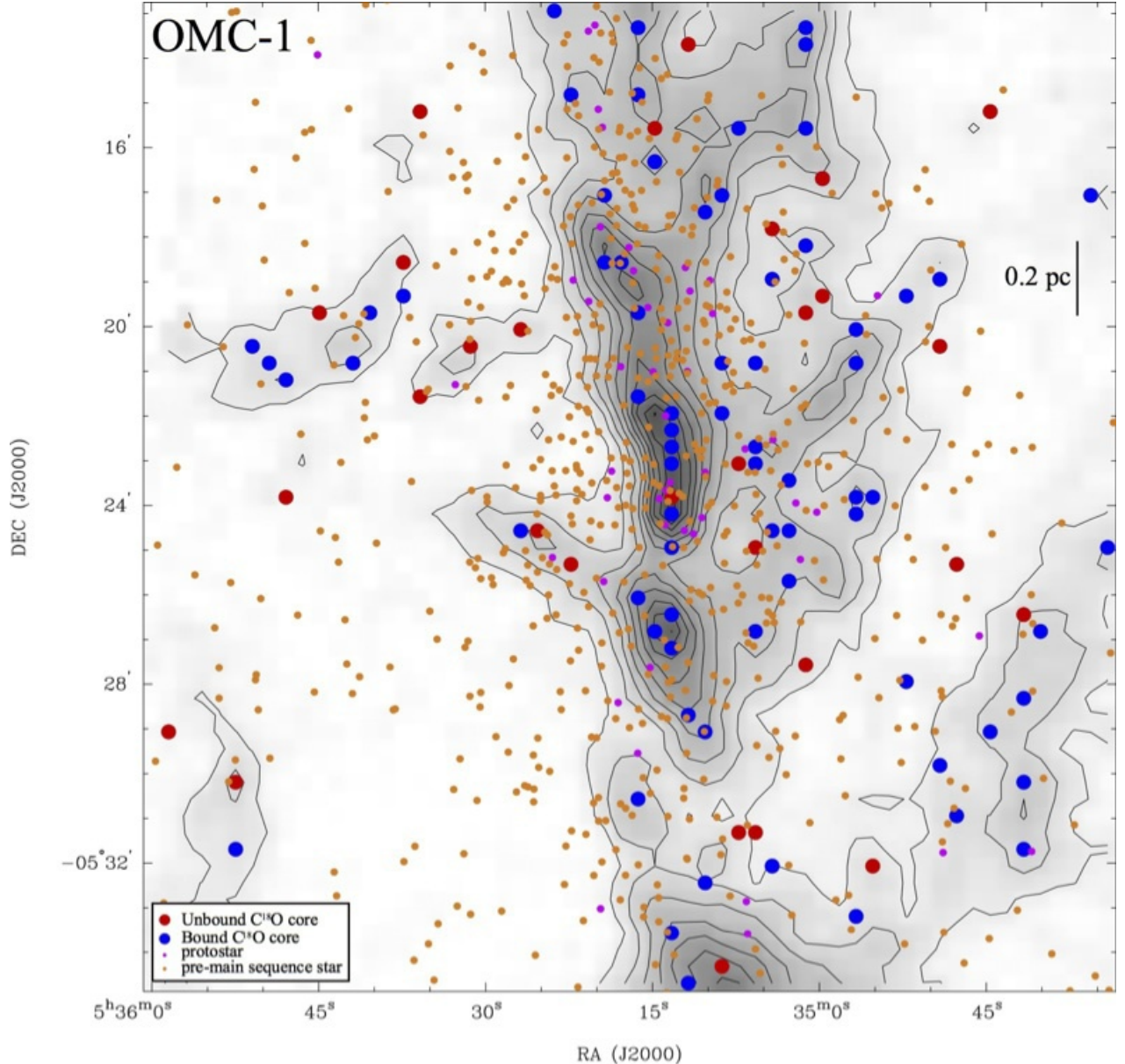


Fig. 16.— The identified C¹⁸O cores shown on the C¹⁸O total integrated intensity map of the OMC-1 region. The contour levels start at 1 K km s⁻¹ in T_{MB} with intervals of 1 K km s⁻¹. The 1.1 mm emission around the central Orion-KL region could not be reconstructed as an accurate structure with the AzTEC data-reduction technique, because the continuum emission around Orion-KL was too bright. The meanings of the symbols are the same as in Fig. 12.

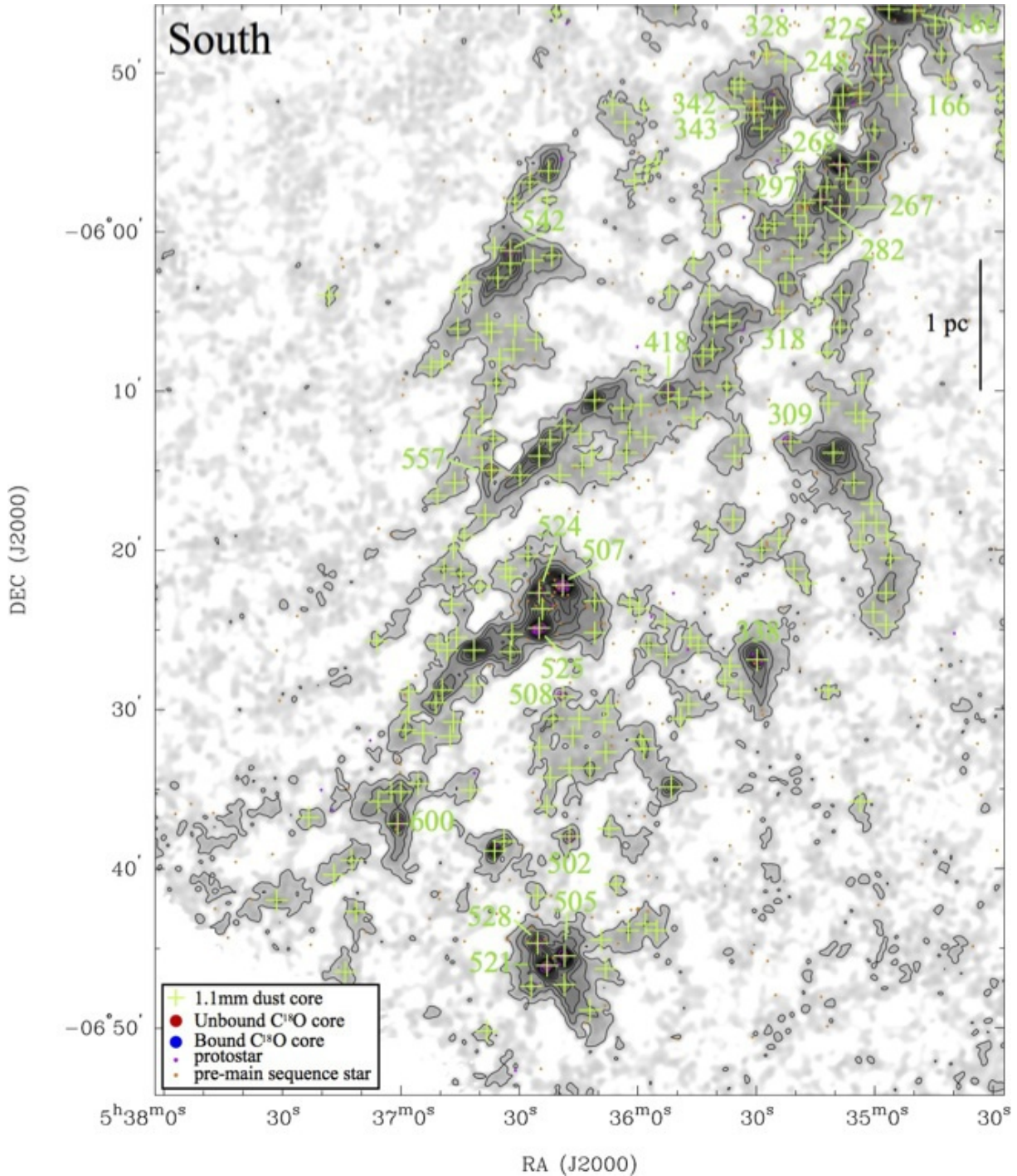


Fig. 17.— The identified 1.1 mm dust cores shown on the AzTEC 1.1 mm map of the South region. There is no C¹⁸O data in this region. The symbols and the contours are the same as in Fig. 12.

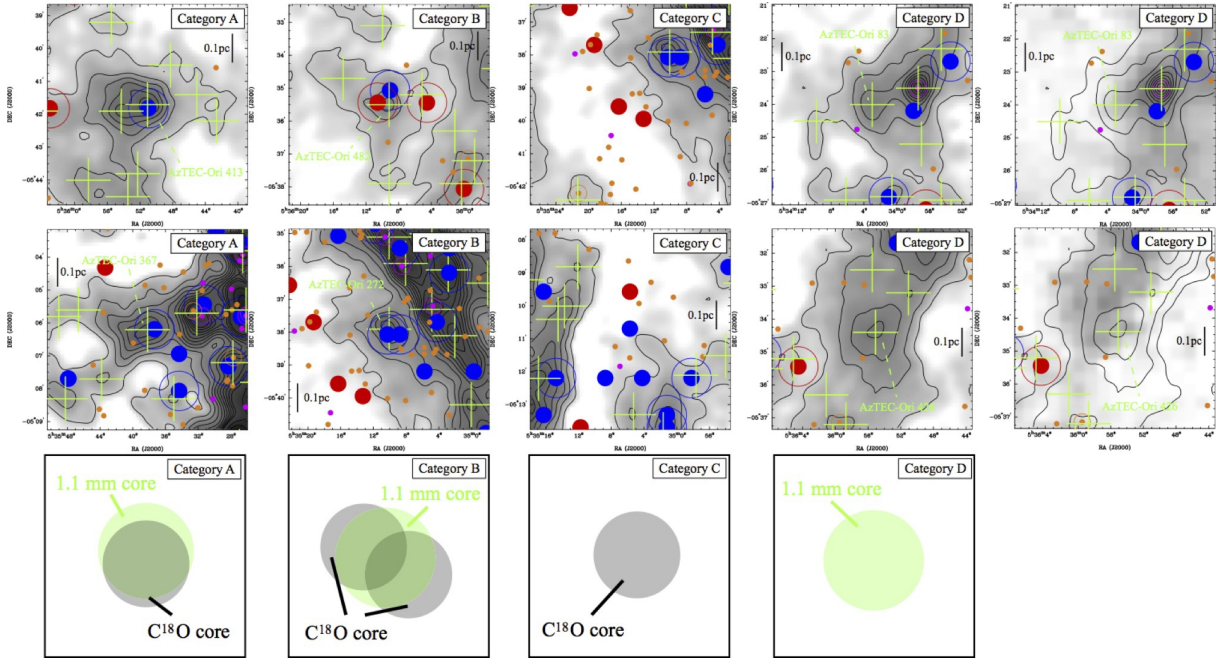


Fig. 18.— Typical examples in Categories A to D (from left to right). The top and middle panels show the close-up views of the 1.1 mm continuum emission images with the positions of the 1.1 mm dust and C^{18}O cores. The most right panels show the C^{18}O total intensities in gray scale with the 1.1 mm continuum emission (contours) for the two examples in Category D. The symbols and the contours are the same as in Fig. 12. The schematic illustrations in the bottom panels indicate the spatial relations between the 1.1 mm dust and C^{18}O cores in the four categories.

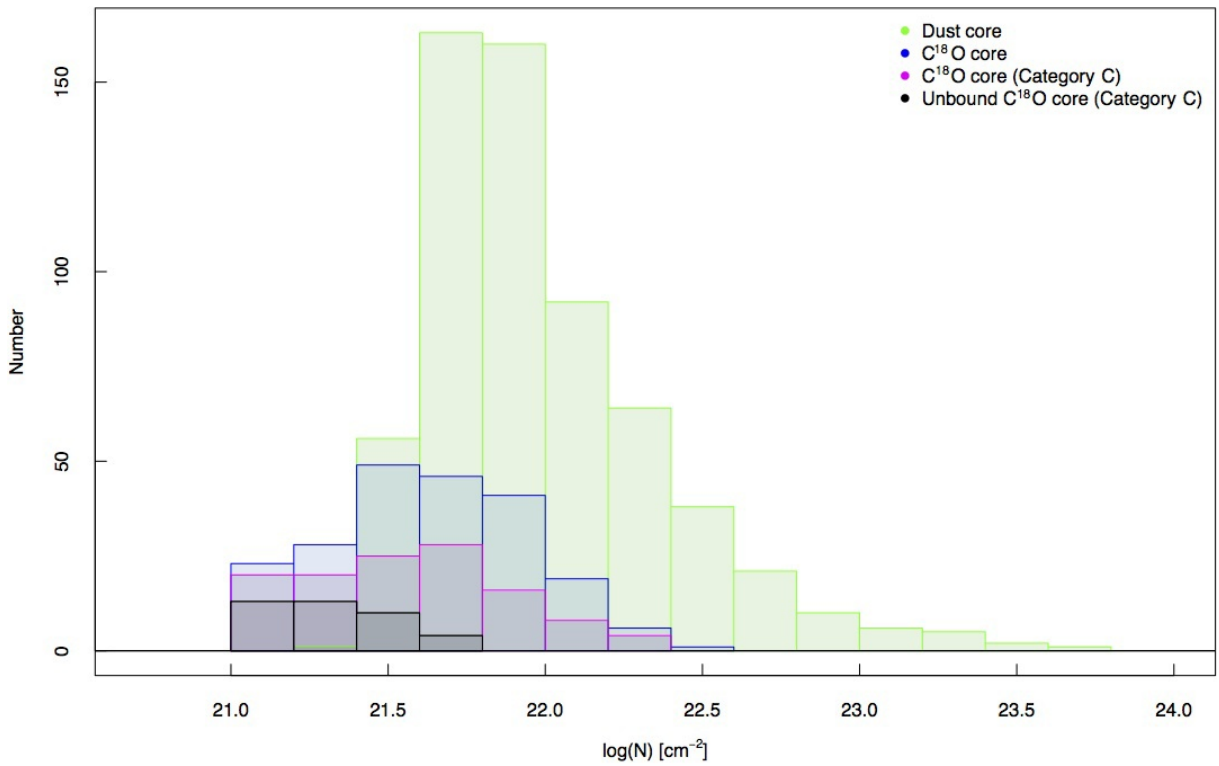


Fig. 19.— Histograms of the column densities of the 1.1 mm dust and C¹⁸O cores. The column densities of each cores is estimated from the equation, $N_{\text{H}_2} = n \times 2 R_{\text{core}}$. The green, blue, pink, and black histograms correspond to the 1.1 mm dust core, all C¹⁸O cores , C¹⁸O cores in Category C, and unbound C¹⁸O cores in Category C, respectively. The C¹⁸O cores distributed around Orion-KL are excluded for this plot.

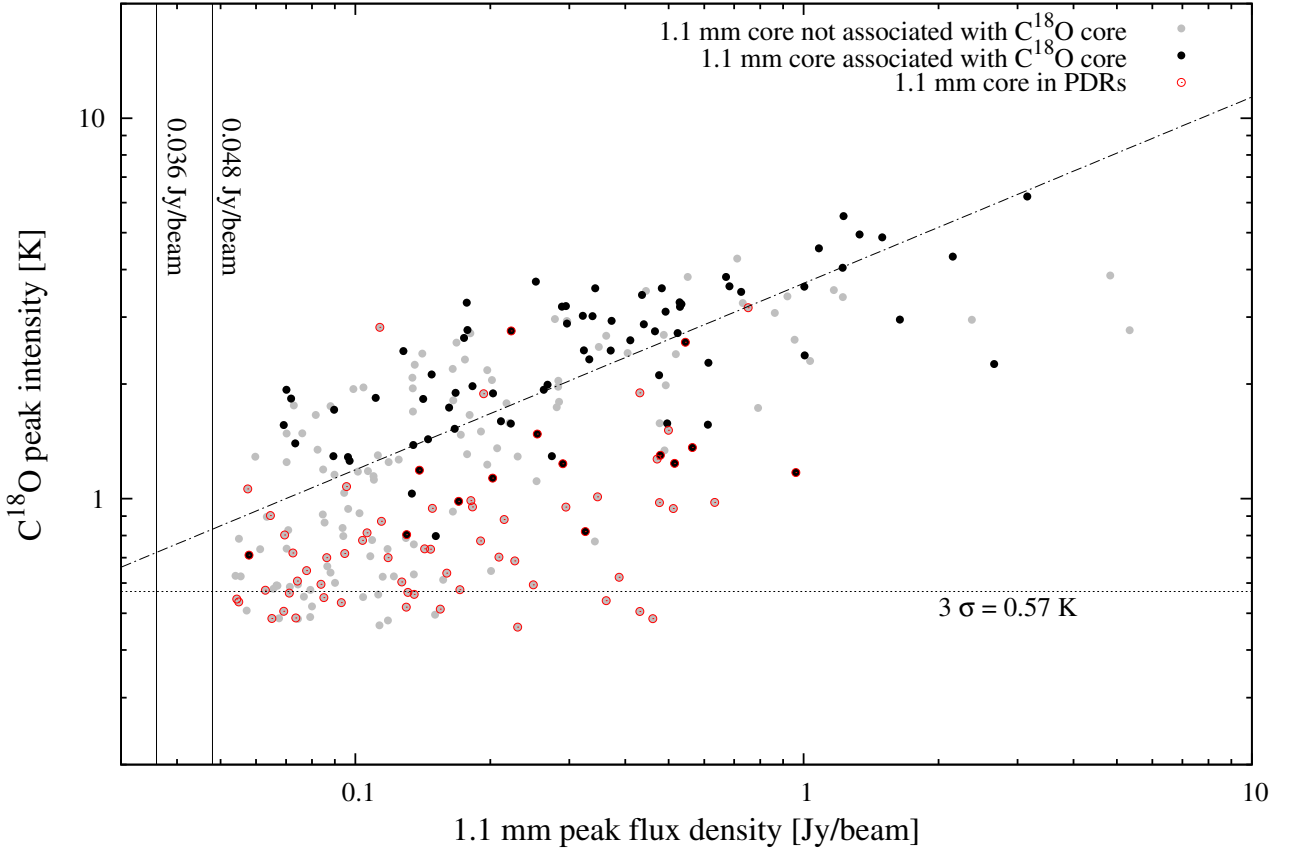


Fig. 20.— Comparison between the 1.1 mm peak flux density and the C¹⁸O peak intensity at the 1.1 mm dust cores. The gray filled circles are for the 1.1 mm dust cores not associated with any C¹⁸O cores. The black filled circles are for the 1.1 mm dust cores associated with the C¹⁸O cores. The open red circles are for the 1.1 mm dust cores in the PDRs. The horizontal line indicates the 3σ level ($1\sigma=0.19$ K) of the C¹⁸O data. The vertical lines indicate the 4σ level ($1\sigma=9$ mJy beam⁻¹ in the central region of the 1.1 mm dust map and 12 mJy beam⁻¹ on the outer edge) of the 1.1 mm data. The dashed line shows the best fit power law function for the 1.1 mm dust cores associated with the C¹⁸O cores, $\log_{10}(T_{\text{C}^{18}\text{O}}/\text{K}) = (0.49 \pm 0.14) \log_{10}(F_{1.1\text{mm}}/\text{Jy beam}^{-1}) + (0.57 \pm 0.06)$.

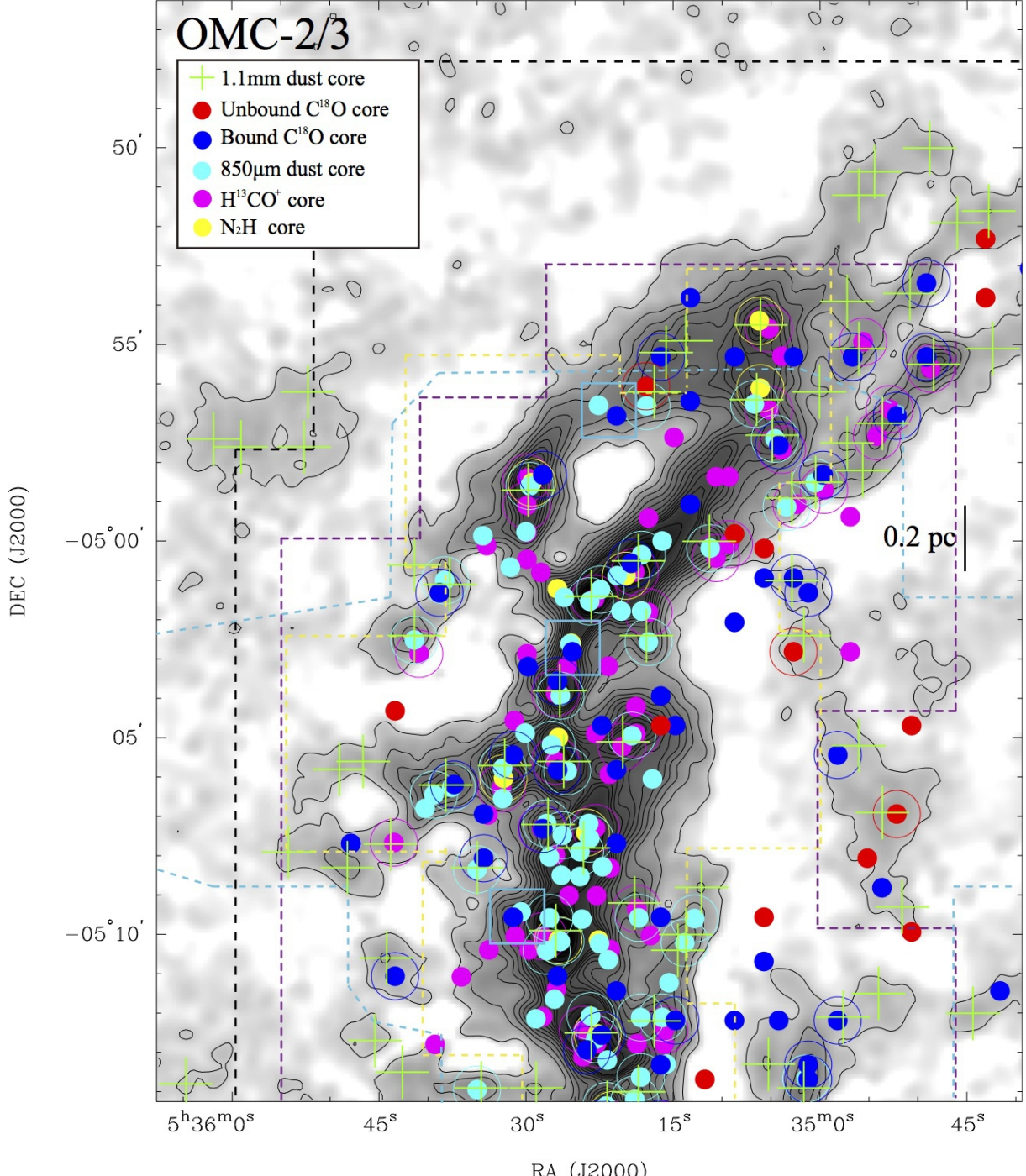


Fig. 21.— The identified 1.1 mm dust and C^{18}O cores shown together with the 850 μm , H^{13}CO^+ , and N_2H^+ cores on the AzTEC 1.1 mm map of the OMC-2/3 region. The green crosses and the red and blue circles are the same as in Figure 10. The aqua-, magenta-, and yellow-filled circles denote the positions of the 850 μm , H^{13}CO^+ , and N_2H^+ cores, respectively. The open circles denote the cores associated with the 1.1 mm dust cores. The black, aqua, magenta, and yellow dashed lines indicate C^{18}O , 850 μm , H^{13}CO^+ , and N_2H^+ observed areas. Contours for the 1.1 mm map are the same as in Fig. 12. The open aqua boxes denote the C^{18}O cores associated with the 850 μm dust cores, but not associated with any 1.1 mm dust cores.

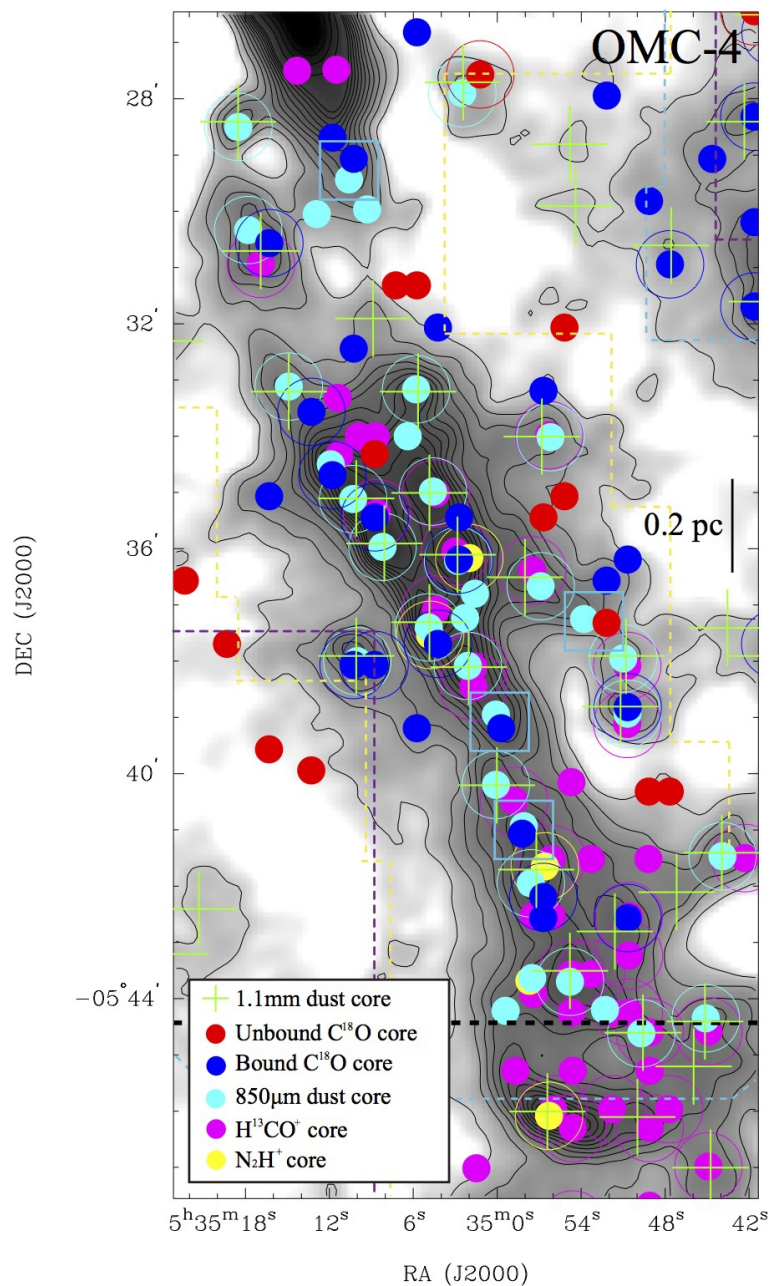


Fig. 22.— The same as Fig. 12, but for the OMC-4 region.

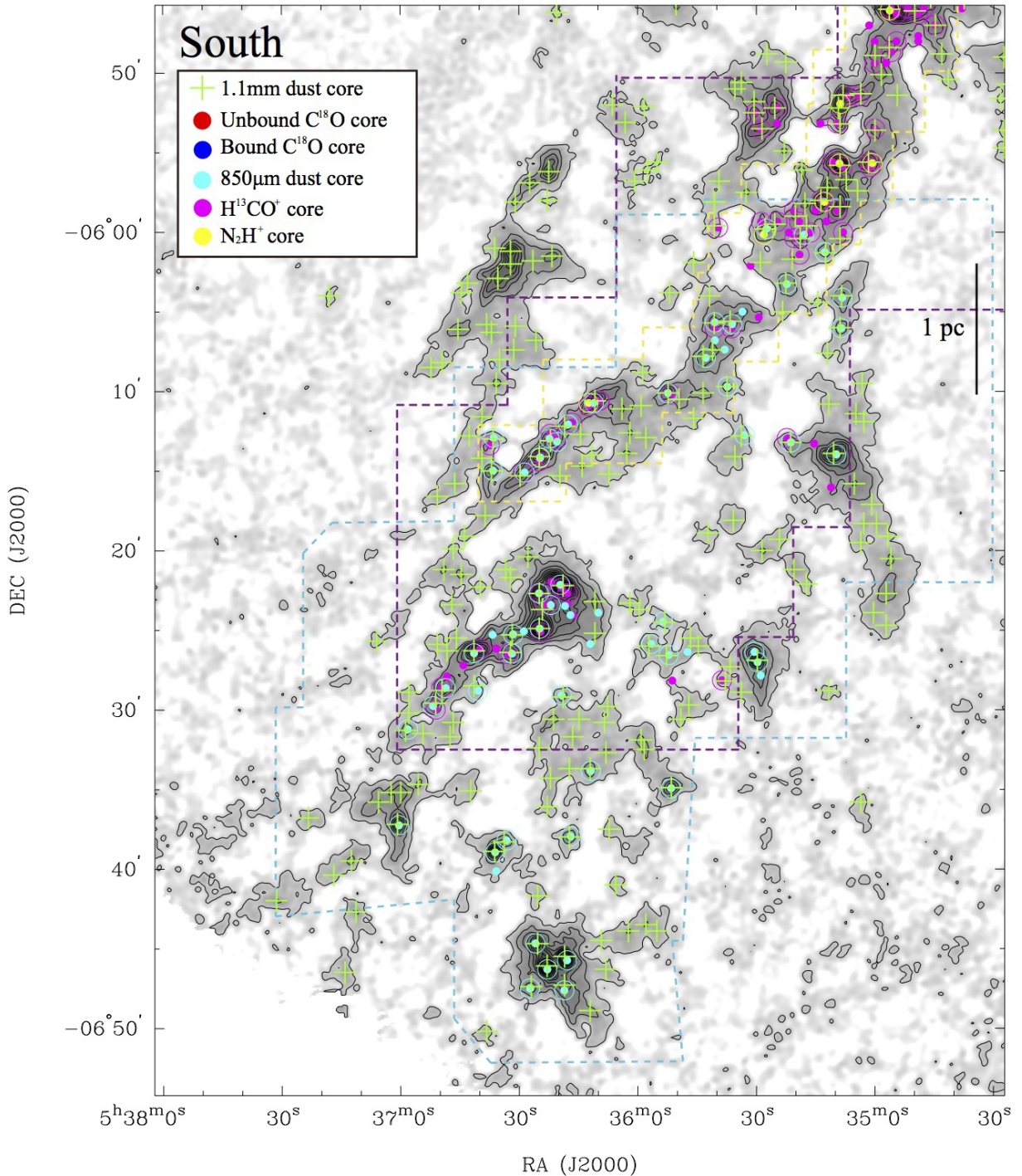


Fig. 23.— The same as Fig. 12, but for the South region. There is no C¹⁸O data for this region

Table 1. Physical properties of the 1.1 mm dust cores

Property	Mean [†]	Minimum	Maximum
Peak flux density [Jy beam ⁻¹]	0.27 ± 0.45	0.05	5.95
R_{core} [pc]	0.09 ± 0.03	0.01	0.20
M_{H_2} [M_{\odot}]	5.52 ± 9.55	0.60	116.95
Density [$\times 10^4$ cm ⁻³]	5.48 ± 38.94	0.31	915.01

[†]Errors are the standard deviation

Table 2. Identified AzTEC 1.1 mm dust cores

ID AzTEC-Ori	RA (J2000)	DEC (J2000)	Peak flux density [Jy beam ⁻¹]	Aspect ratio major/minor	R_{core} [pc]	M_{H_2} [M_{\odot}]	n [$\times 10^4 \text{ cm}^{-3}$]	category	note [†] [‡]
1	5 31 28.6	-5 40 33.6	0.10	1.1	0.10	1.9	0.7	...	
2	5 31 48.8	-5 23 4.2	0.11	1.2	0.08	1.5	1.2	...	
3	5 32 11.2	-5 38 16.6	0.18	1.0	0.14	6.0	0.9	...	
4	5 32 11.6	-5 36 46.6	0.09	2.1	0.08	1.3	1.1	...	
5	5 32 14.8	-5 37 40.7	0.09	1.9	0.06	1.3	3.0	...	
6	5 32 18.5	-5 37 46.7	0.10	1.0	0.10	1.9	0.8	...	
7	5 32 19.3	-5 33 58.8	0.09	1.3	0.09	1.3	0.9	...	
8	5 32 26.6	-5 26 34.9	0.06	1.1	0.08	1.1	0.8	...	
9	5 32 28.5	-5 34 16.9	0.51	1.5	0.16	10.1	1.1	...	
10	5 32 37.0	-5 35 53.1	0.25	1.4	0.14	7.6	1.3	...	
11	5 32 42.2	-5 35 47.2	0.96	1.4	0.12	18.4	4.0	...	
12	5 32 49.0	-5 34 41.3	0.62	1.3	0.14	16.8	2.6	...	1 protostar
13	5 32 49.0	-5 32 59.3	0.07	2.7	0.10	1.4	0.6	...	1 protostar, 1 PMS star
14	5 32 53.8	-5 33 59.4	0.13	1.2	0.12	3.6	0.8	...	
15	5 32 55.9	-5 32 59.4	0.06	1.4	0.05	0.6	1.7	...	
16	5 32 58.7	-5 32 23.4	0.07	1.6	0.07	0.8	1.0	...	
17	5 33 0.3	-5 30 47.5	0.10	1.3	0.07	1.1	1.5	...	
18	5 33 0.7	-5 31 35.5	0.10	1.3	0.08	1.5	1.3	...	
19	5 33 4.3	-5 30 41.5	0.08	1.1	0.09	1.4	0.9	...	
20	5 33 11.5	-5 28 47.6	0.06	1.2	0.07	0.7	0.9	...	
21	5 33 15.1	-5 56 47.5	0.09	1.0	0.08	1.2	1.0	...	
22	5 33 16.7	-5 40 35.6	0.07	1.3	0.09	1.3	0.7	...	
23	5 33 17.9	-5 58 47.5	0.06	1.3	0.08	1.0	0.8	...	
24	5 33 18.4	-5 34 17.7	0.13	1.4	0.08	2.0	1.9	...	
25	5 33 20.1	-4 48 23.9	0.08	1.7	0.09	1.2	0.8	...	
26	5 33 21.2	-5 35 29.7	0.07	1.1	0.08	1.1	0.9	...	
27	5 33 22.0	-5 30 35.7	0.07	1.3	0.08	1.1	1.1	...	
28	5 33 22.3	-5 57 35.6	0.06	1.0	0.12	1.8	0.5	...	
29	5 33 22.7	-5 49 35.7	0.13	1.1	0.15	4.6	0.6	...	
30	5 33 23.6	-5 34 5.7	0.07	1.3	0.09	1.5	1.0	...	
31	5 33 24.0	-5 35 5.7	0.06	1.2	0.05	0.6	2.1	...	
32	5 33 26.4	-5 30 53.8	0.12	1.4	0.10	2.7	1.3	...	
33	5 33 27.2	-5 35 35.8	0.07	1.0	0.07	1.0	1.2	...	
34	5 33 28.0	-5 48 23.7	0.11	1.3	0.12	3.2	0.7	...	
35	5 33 29.0	-6 30 23.2	0.14	1.4	0.10	2.7	1.1	...	
36	5 33 30.3	-5 55 47.7	0.10	1.0	0.11	1.7	0.6	...	
37	5 33 30.4	-5 29 47.8	0.06	1.7	0.07	0.7	1.0	...	1 PMS star
38	5 33 31.1	-6 18 23.5	0.11	1.0	0.08	1.4	1.4	...	
39	5 33 31.2	-5 50 35.8	0.34	1.2	0.17	9.7	0.8	...	1 protostar
40	5 33 32.7	-6 29 41.2	0.40	1.2	0.09	7.2	3.8	...	
41	5 33 33.1	-6 17 59.5	0.11	1.1	0.07	1.5	2.0	...	
42	5 33 33.9	-6 27 41.3	0.20	1.4	0.10	5.3	2.0	...	
43	5 33 33.9	-6 26 41.3	0.11	1.5	0.06	1.5	2.7	...	
44	5 33 34.8	-5 40 5.9	0.12	1.2	0.07	2.1	2.6	...	
45	5 33 35.2	-5 30 53.9	0.08	1.3	0.08	1.2	1.1	...	
46	5 33 35.6	-5 42 59.9	0.07	1.5	0.12	2.0	0.4	D	
47	5 33 35.9	-6 30 5.3	0.09	1.2	0.06	1.2	2.3	...	
48	5 33 38.5	-5 31 35.9	0.06	1.0	0.09	1.2	0.7	D	
49	5 33 39.7	-5 26 35.9	0.10	1.4	0.07	1.4	1.4	D	
50	5 33 40.0	-5 39 53.9	0.07	1.3	0.11	2.3	0.7	D	

Table 2—Continued

ID AzTEC-Ori	RA (J2000)	DEC (J2000)	Peak flux density [Jy beam ⁻¹]	Aspect ratio major/minor	R_{core} [pc]	M_{H_2} [M_{\odot}]	n [$\times 10^4 \text{cm}^{-3}$]	category	note [†] [‡]
51	5 33 40.7	-6 28 59.4	0.08	1.0	0.05	0.8	3.1	...	
52	5 33 40.7	-6 26 47.4	0.11	1.4	0.08	2.4	1.9	...	
53	5 33 40.8	-6 0 41.8	0.06	1.4	0.08	1.1	0.8	...	
54	5 33 41.5	-6 28 17.4	0.08	1.3	0.07	1.0	1.5	...	
55	5 33 42.4	-6 2 29.8	0.07	1.5	0.08	0.9	0.7	...	
56	5 33 42.9	-5 40 23.9	0.06	1.1	0.08	0.9	0.6	D	
57	5 33 43.3	-5 27 30.0	0.06	1.1	0.09	1.2	0.7	D	
58	5 33 43.6	-6 1 23.8	0.07	1.1	0.09	1.3	0.7	...	
59	5 33 44.3	-6 26 29.5	0.10	1.2	0.05	1.1	3.0	...	
60	5 33 46.4	-6 25 41.5	0.09	1.6	0.07	1.2	1.6	...	
61	5 33 46.7	-6 45 34.9	0.08	1.3	0.04	0.6	3.0	...	
62	5 33 48.9	-5 16 30.0	0.08	1.5	0.09	1.3	0.7	...	
63	5 33 49.3	-5 20 0.0	0.08	1.1	0.10	1.6	0.7	...	
64	5 33 49.3	-5 14 18.0	0.08	1.1	0.08	1.3	0.9	...	
65	5 33 49.7	-5 39 0.0	0.13	1.1	0.14	4.6	0.7	D	
66	5 33 49.7	-5 30 0.0	0.11	1.0	0.11	2.4	0.8	D	
67	5 33 50.8	-6 25 5.6	0.10	1.0	0.11	1.6	0.6	...	
68	5 33 50.9	-5 18 54.0	0.09	1.0	0.06	1.3	2.2	...	
69	5 33 51.3	-5 35 24.0	0.08	1.5	0.11	1.8	0.6	A	C ¹⁸ O-Ori 3
70	5 33 53.3	-5 27 36.1	0.09	1.1	0.08	1.7	1.5	D	
71	5 33 54.5	-5 26 54.1	0.09	1.0	0.07	1.2	1.8	A	C ¹⁸ O-Ori 7
72	5 33 54.5	-5 22 18.1	0.22	2.0	0.14	7.4	1.2	A	C ¹⁸ O-Ori 5
73	5 33 55.0	-5 19 6.1	0.11	1.0	0.09	2.0	1.0	...	
74	5 33 55.0	-5 11 36.1	0.08	1.4	0.08	1.3	1.0	...	
75	5 33 55.3	-5 30 12.1	0.19	1.6	0.09	4.3	2.4	A	C ¹⁸ O-Ori 6
76	5 33 57.0	-5 25 12.1	0.12	1.4	0.10	2.6	1.3	D	
77	5 33 57.4	-5 23 30.1	0.85	1.3	0.10	11.4	4.9	D	1 protostar
78	5 33 58.5	-5 39 12.1	0.11	1.1	0.10	1.9	0.9	D	
79	5 34 0.2	-5 28 24.1	0.34	1.3	0.11	7.3	2.5	A	C ¹⁸ O-Ori 9
80	5 34 0.6	-5 30 12.1	0.18	1.9	0.07	3.7	4.1	D	
81	5 34 0.6	-5 26 48.1	0.18	1.1	0.09	3.1	1.9	A	C ¹⁸ O-Ori 11
82	5 34 1.0	-5 4 36.1	0.07	1.2	0.09	1.0	0.7	...	
83	5 34 3.0	-5 24 0.1	0.30	1.3	0.12	7.6	1.8	D	
84	5 34 3.4	-5 30 0.1	0.17	1.3	0.07	2.8	2.8	D	
85	5 34 3.4	-4 52 30.2	0.11	1.3	0.10	1.9	0.7	...	
86	5 34 4.2	-5 34 18.1	0.37	1.4	0.13	9.2	1.9	D	
87	5 34 4.2	-5 32 24.1	0.36	1.4	0.13	10.9	2.0	A	C ¹⁸ O-Ori 12
88	5 34 4.6	-5 35 36.1	0.18	1.2	0.12	5.1	1.3	D	
89	5 34 6.2	-5 26 54.2	0.09	1.6	0.07	1.3	1.5	D	
90	5 34 6.3	-4 55 0.2	0.10	1.2	0.08	1.4	1.2	...	
91	5 34 6.3	-4 52 48.2	0.15	1.1	0.07	2.0	3.1	...	
92	5 34 7.0	-5 13 36.2	0.08	1.0	0.10	1.4	0.7	...	1 PMS star
93	5 34 7.5	-4 53 30.2	0.17	1.2	0.10	4.1	1.9	...	
94	5 34 8.2	-5 37 24.2	0.16	1.1	0.13	5.3	1.0	D	
95	5 34 9.1	-4 55 30.2	0.10	1.6	0.09	1.7	1.1	...	
96	5 34 9.8	-5 24 30.2	0.07	1.6	0.11	1.5	0.5	D	
97	5 34 10.1	-6 37 11.4	0.10	1.5	0.08	1.3	0.9	...	
98	5 34 11.0	-5 14 42.2	0.07	1.1	0.11	1.5	0.5	...	
99	5 34 11.7	-6 32 53.6	0.10	1.1	0.09	1.7	1.1	...	
100	5 34 13.3	-6 31 41.6	0.11	1.5	0.09	2.5	1.4	...	

Table 2—Continued

ID AzTEC-Ori	RA (J2000)	DEC (J2000)	Peak flux density [Jy beam ⁻¹]	Aspect ratio major/minor	R_{core} [pc]	M_{H_2} [M_{\odot}]	n [$\times 10^4 \text{cm}^{-3}$]	category	note [†] [‡]
101	5 34 14.9	-6 30 11.7	0.10	1.1	0.07	1.6	1.9	...	
102	5 34 15.0	-5 28 24.2	0.10	1.4	0.10	1.8	0.8	A	$\text{C}^{18}\text{O}-\text{Ori}$ 14
103	5 34 16.3	-4 53 24.3	0.12	1.3	0.07	2.0	2.6	...	
104	5 34 16.5	-6 30 41.7	0.09	1.3	0.05	1.2	3.2	...	
105	5 34 16.6	-5 36 36.2	0.31	1.0	0.12	8.8	2.0	A	$\text{C}^{18}\text{O}-\text{Ori}$ 16, 1 PMS star
106	5 34 17.1	-5 14 0.2	0.13	1.0	0.11	2.7	0.9	...	
107	5 34 17.3	-6 33 53.6	0.14	1.4	0.11	3.7	1.2	...	
108	5 34 17.5	-4 46 48.3	0.08	1.1	0.12	2.1	0.4	...	
109	5 34 18.2	-5 30 0.2	0.08	1.4	0.12	1.6	0.4	A	$\text{C}^{18}\text{O}-\text{Ori}$ 19
110	5 34 18.6	-5 26 48.2	0.27	1.2	0.12	4.5	1.1	B	$\text{C}^{18}\text{O}-\text{Ori}$ 17, 20
111	5 34 19.5	-4 53 18.3	0.11	1.9	0.08	1.9	1.4	...	
112	5 34 19.8	-6 34 35.6	0.11	1.2	0.09	2.2	1.1	...	
113	5 34 20.2	-5 44 6.2	0.09	1.4	0.08	1.1	0.9	D	
114	5 34 20.7	-5 22 18.3	0.14	1.6	0.09	2.2	1.2	D	
115	5 34 21.4	-5 36 18.2	0.15	1.1	0.09	3.2	1.6	D	
116	5 34 21.8	-6 30 35.7	0.11	1.0	0.09	2.4	1.3	...	
117	5 34 21.9	-5 19 54.3	0.13	1.4	0.09	2.6	1.4	...	
118	5 34 22.6	-5 45 24.2	0.06	1.2	0.07	0.8	0.8	...	
119	5 34 22.7	-5 38 6.2	0.40	1.6	0.12	10.5	2.6	D	
120	5 34 23.1	-5 6 36.3	0.11	1.6	0.08	1.4	1.0	...	
121	5 34 23.9	-5 39 0.3	0.22	1.4	0.06	2.8	4.5	D	
122	5 34 24.3	-5 14 6.3	0.12	1.2	0.09	2.2	1.3	...	
123	5 34 24.3	-5 7 18.3	0.09	1.4	0.11	1.8	0.5	...	
124	5 34 24.7	-5 21 6.3	0.12	1.9	0.08	2.2	1.9	...	
125	5 34 24.7	-4 56 18.3	0.08	1.2	0.08	1.2	0.9	...	
126	5 34 25.5	-5 21 48.3	0.11	1.5	0.08	1.8	1.7	D	1 PMS star
127	5 34 25.5	-5 19 36.3	0.20	1.0	0.10	5.1	2.3	...	
128	5 34 25.5	-4 53 6.3	0.10	1.2	0.07	1.4	1.7	...	
129	5 34 26.7	-5 50 42.2	0.09	2.1	0.08	1.7	1.2	...	
130	5 34 26.7	-4 53 42.3	0.12	1.1	0.07	1.6	2.2	...	
131	5 34 27.1	-5 33 54.3	0.19	1.2	0.09	3.0	1.9	A	$\text{C}^{18}\text{O}-\text{Ori}$ 23
132	5 34 27.5	-5 54 42.2	0.07	1.3	0.06	0.8	1.5	...	
133	5 34 27.5	-5 53 36.2	0.08	1.1	0.08	1.1	0.9	...	
134	5 34 27.5	-5 49 0.2	0.15	1.5	0.15	6.6	0.8	...	
135	5 34 27.5	-5 39 12.3	0.22	1.6	0.12	4.7	1.1	A	$\text{C}^{18}\text{O}-\text{Ori}$ 27
136	5 34 27.5	-5 32 18.3	0.20	1.1	0.09	3.4	1.9	A	$\text{C}^{18}\text{O}-\text{Ori}$ 26
137	5 34 27.5	-5 26 24.3	0.35	1.2	0.11	6.5	2.3	A	$\text{C}^{18}\text{O}-\text{Ori}$ 25, 1 PMS star
138	5 34 27.5	-5 24 54.3	0.30	1.5	0.14	9.6	1.5	A	$\text{C}^{18}\text{O}-\text{Ori}$ 22
139	5 34 27.5	-5 18 0.3	0.15	1.3	0.10	3.2	1.4	...	
140	5 34 28.3	-5 51 36.2	0.06	1.1	0.08	1.0	0.9	...	
141	5 34 28.3	-5 23 18.3	0.11	1.4	0.11	3.1	1.1	D	
142	5 34 28.7	-4 50 54.4	0.09	1.3	0.10	1.7	0.6	...	
143	5 34 29.1	-5 35 42.3	0.28	1.3	0.13	7.3	1.4	D	1 protostar
144	5 34 29.1	-5 33 36.3	0.19	1.0	0.07	2.4	2.9	D	
145	5 34 29.1	-4 55 30.3	0.22	1.1	0.06	2.4	4.0	...	1 protostar
146	5 34 29.9	-5 31 12.3	0.10	1.1	0.16	4.2	0.4	D	
147	5 34 30.3	-5 14 24.3	0.12	1.5	0.10	2.8	1.1	D	
148	5 34 31.1	-5 9 24.3	0.09	1.5	0.09	1.5	0.8	D	
149	5 34 31.5	-5 15 36.3	0.10	1.1	0.08	1.8	1.3	D	
150	5 34 33.1	-4 54 12.4	0.18	1.3	0.09	3.5	2.3	A	$\text{C}^{18}\text{O}-\text{Ori}$ 32

Table 2—Continued

ID AzTEC-Ori	RA (J2000)	DEC (J2000)	Peak flux density [Jy beam ⁻¹]	Aspect ratio major/minor	R_{core} [pc]	M_{H_2} [M_{\odot}]	n [$\times 10^4 \text{cm}^{-3}$]	category	note [†]	note [‡]
151	5 34 33.9	-5 27 6.3	0.10	2.7	0.11	2.5	0.8	D	1 PMS star	
152	5 34 34.3	-5 19 36.3	0.14	1.1	0.11	3.6	1.1	D		
153	5 34 34.7	-5 40 6.3	0.34	1.6	0.09	5.6	3.8	A	C^{18}O -Ori 35, 1 protostar	
154	5 34 34.7	-5 22 0.3	0.27	1.2	0.09	3.7	1.9	D		
155	5 34 35.5	-5 18 6.3	0.21	1.4	0.09	5.1	2.8	D		
156	5 34 36.3	-5 16 42.3	0.15	1.9	0.06	1.8	3.3	A	C^{18}O -Ori 37	
157	5 34 36.3	-5 15 48.3	0.07	1.6	0.07	1.0	1.1	D		
158	5 34 36.3	-5 10 42.3	0.07	1.3	0.10	1.3	0.6	D		
159	5 34 37.1	-5 17 18.3	0.17	1.5	0.06	2.4	4.9	A	C^{18}O -Ori 37	
160	5 34 37.5	-5 45 18.3	0.14	1.8	0.08	2.8	2.2	...		
161	5 34 37.5	-5 41 48.3	0.23	1.0	0.08	3.5	2.6	D		
162	5 34 40.3	-5 26 30.3	0.11	1.3	0.12	3.0	0.6	B	C^{18}O -Ori 40, 43, 1 PMS star	
163	5 34 40.7	-5 37 54.3	0.13	1.3	0.08	1.5	1.4	A	C^{18}O -Ori 41	
164	5 34 40.7	-5 31 36.3	0.61	1.5	0.17	17.3	1.4	A	C^{18}O -Ori 46, 1 protostar	
165	5 34 41.2	-5 16 12.3	0.05	1.6	0.09	1.1	0.7	D		
166	5 34 41.5	-5 50 24.3	0.10	1.8	0.09	1.4	0.8	...	1 PMS star	
167	5 34 42.4	-5 28 24.3	0.28	1.3	0.17	11.7	1.1	A	C^{18}O -Ori 44, 1 PMS star	
168	5 34 42.4	-4 55 6.4	0.11	1.5	0.08	1.8	1.6	D		
169	5 34 42.8	-4 51 36.4	0.14	1.0	0.11	2.9	0.8	D	1 PMS star	
170	5 34 43.1	-5 48 48.3	0.17	1.1	0.13	5.3	1.0	...		
171	5 34 43.2	-5 18 36.3	0.09	1.1	0.08	1.6	1.4	D		
172	5 34 43.6	-5 37 24.3	0.08	1.4	0.06	0.7	1.7	D		
173	5 34 44.0	-5 41 24.3	0.37	1.1	0.08	4.8	3.5	D	1 protostar, [ISK2007] 3, [NW2007] 8	
174	5 34 44.4	-5 12 0.4	0.09	1.6	0.06	1.0	1.6	D		
175	5 34 44.7	-5 47 0.3	0.31	1.0	0.11	8.4	2.4	...	[ISK2007] 5	
176	5 34 45.2	-5 44 24.3	0.39	1.4	0.08	7.0	5.2	D	[ISK2007] 4, [NW2007] 2	
177	5 34 45.2	-5 18 6.4	0.14	1.3	0.09	2.7	1.6	D		
178	5 34 46.0	-5 45 12.3	0.39	1.9	0.07	8.9	11.0	...		
179	5 34 46.0	-4 51 54.4	0.12	1.0	0.06	1.4	2.6	D		
180	5 34 47.2	-5 42 6.3	0.28	1.5	0.07	5.0	5.2	D	1 protostar	
181	5 34 47.6	-5 30 36.4	0.14	1.4	0.10	3.1	1.4	A	C^{18}O -Ori 52, 1 PMS star	
182	5 34 48.4	-4 55 30.4	0.55	1.1	0.09	8.1	4.6	A	C^{18}O -Ori 55, [ISK2007] 6	
183	5 34 48.8	-4 50 0.4	0.12	1.0	0.08	1.7	1.3	D	1 PMS star	
184	5 34 49.2	-5 18 24.4	0.13	1.6	0.13	4.1	0.8	A	C^{18}O -Ori 56	
185	5 34 49.6	-5 44 36.3	0.40	1.2	0.04	6.1	50.8	D	[ISK2007] 9, 18, [NW2007] 1	
186	5 34 50.0	-5 46 6.3	0.59	1.3	0.07	11.1	12.9	...	1 PMS star, [ISK2007] 7, 11, 20	
187	5 34 50.8	-5 37 54.4	0.18	1.0	0.07	2.8	3.3	D	[ISK2007] 14, [NW2007] 15	
188	5 34 50.8	-4 53 42.4	0.19	1.4	0.09	3.4	1.8	A	C^{18}O -Ori 54	
189	5 34 51.2	-5 38 48.4	0.29	1.6	0.06	2.9	5.3	A	C^{18}O -Ori 63, [ISK2007] 15, [NW2007] 11	
190	5 34 51.2	-5 22 36.4	0.11	1.6	0.09	2.2	1.2	D	1 PMS star	
191	5 34 51.6	-5 42 48.4	0.49	1.8	0.07	11.2	13.3	A	C^{18}O -Ori 64, [ISK2007] 16, 17	
192	5 34 51.6	-5 9 18.4	0.07	1.0	0.09	1.2	0.7	D		
193	5 34 52.8	-5 23 12.4	0.08	1.2	0.04	0.7	3.8	D		
194	5 34 53.6	-5 6 54.4	0.13	1.1	0.16	5.6	0.5	A	C^{18}O -Ori 66	
195	5 34 53.6	-4 57 0.4	0.39	1.2	0.08	5.6	4.1	A	C^{18}O -Ori 65, [ISK2007] 21, 22	
196	5 34 54.0	-5 11 30.4	0.08	1.1	0.09	1.6	0.9	D		
197	5 34 54.4	-5 51 24.3	0.14	1.2	0.14	5.6	0.9	...		
198	5 34 54.4	-5 29 54.4	0.06	1.7	0.10	1.5	0.6	D		
199	5 34 54.4	-4 50 36.4	0.12	1.1	0.07	1.5	1.7	D		
200	5 34 54.8	-5 43 30.4	0.71	1.2	0.13	28.5	5.3	D	[ISK2007] 24, 27, [NW2007] 5	

Table 2—Continued

ID AzTEC-Ori	RA (J2000)	DEC (J2000)	Peak flux density [Jy beam $^{-1}$]	Aspect ratio major/minor	R_{core} [pc]	M_{H_2} [M_{\odot}]	n [$\times 10^4 \text{cm}^{-3}$]	category	note † ‡
201	5 34 54.8	-5 28 48.4	0.06	1.9	0.08	0.8	0.7	D	
202	5 34 55.2	-5 24 30.4	0.22	1.0	0.08	3.0	2.4	A	C^{18}O -Ori 80
203	5 34 55.6	-4 58 12.4	0.18	1.2	0.04	1.9	9.8	D	
204	5 34 56.0	-6 20 30.0	0.15	1.6	0.14	5.7	0.9	...	
205	5 34 56.0	-5 5 12.4	0.08	1.1	0.07	1.1	1.3	A	C^{18}O -Ori 85
206	5 34 56.0	-4 55 6.4	0.26	1.3	0.09	4.7	3.2	A	C^{18}O -Ori 76, [ISK2007] 25
207	5 34 56.0	-4 51 12.4	0.13	1.1	0.11	3.2	1.0	D	
208	5 34 56.4	-5 48 24.4	0.28	1.1	0.11	8.0	2.4	...	[ISK2007] 31, 38
209	5 34 56.4	-5 46 0.4	1.10	1.0	0.14	28.3	4.0	...	[ISK2007] 30, 37, [TKU2008] 27
210	5 34 56.8	-6 19 6.1	0.07	1.2	0.07	1.1	1.5	...	
211	5 34 56.8	-5 34 0.4	0.29	1.2	0.11	7.1	2.5	D	[ISK2007] 34, [NW2007] 28
212	5 34 56.8	-5 16 18.4	0.30	1.7	0.12	6.3	1.4	D	[NW2007] 93
213	5 34 57.2	-6 24 42.0	0.09	1.1	0.08	1.6	1.2	...	
214	5 34 57.2	-6 22 42.0	0.20	1.2	0.13	6.4	1.3	...	
215	5 34 57.2	-5 41 42.4	0.68	1.1	0.13	23.7	4.6	A	C^{18}O -Ori 83, [ISK2007] 35, [NW2007] 7, [TKU2008] 25
216	5 34 57.2	-4 57 30.4	0.17	1.2	0.03	1.7	17.1	D	1 PMS star
217	5 34 57.2	-4 53 54.4	0.20	1.3	0.11	5.2	1.9	D	
218	5 34 57.6	-5 12 6.4	0.08	1.2	0.10	1.8	0.7	A	C^{18}O -Ori 86
219	5 34 58.0	-5 36 30.4	0.56	1.0	0.12	16.0	4.1	D	[ISK2007] 40, [NW2007] 21
220	5 34 58.0	-5 25 42.4	0.19	1.5	0.06	2.1	3.6	D	
221	5 34 58.4	-5 50 6.3	0.26	1.2	0.09	6.4	3.6	...	
222	5 34 59.6	-6 18 18.1	0.11	1.1	0.06	1.5	3.3	...	
223	5 34 59.6	-5 21 30.4	1.04	1.0	0.13	20.9	3.6	D	[ISK2007] 45, [NW2007] 55
224	5 35 0.0	-5 53 36.3	0.26	1.3	0.17	12.1	1.0	...	[ISK2007] 52
225	5 35 0.0	-5 48 54.4	0.30	1.4	0.09	6.5	3.8	...	1 protostar, [ISK2007] 51
226	5 35 0.0	-5 40 12.4	0.53	1.5	0.15	16.4	2.1	D	[ISK2007] 46, [NW2007] 10
227	5 35 0.0	-4 56 12.4	0.15	1.6	0.05	2.0	6.8	D	1 PMS star
228	5 35 0.4	-6 23 54.0	0.12	1.4	0.09	2.5	1.6	...	
229	5 35 0.4	-4 58 30.4	0.27	1.0	0.03	2.6	54.0	A	C^{18}O -Ori 88, [ISK2007] 44, [NW2007] 168
230	5 35 0.8	-6 17 6.1	0.11	1.1	0.07	1.7	2.1	...	
231	5 35 0.8	-5 18 6.4	0.18	1.3	0.09	2.8	1.6	A	C^{18}O -Ori 97, [ISK2007] 55, [NW2007] 85
232	5 35 0.8	-5 16 12.4	0.41	1.0	0.05	4.6	13.4	B	C^{18}O -Ori 89, 90, [NW2007] 94
233	5 35 1.6	-5 55 36.3	0.63	1.3	0.14	12.1	2.0	...	[ISK2007] 59, 60, [TKU2008] 29
234	5 35 1.6	-5 13 54.4	0.32	1.9	0.10	6.8	2.7	B	C^{18}O -Ori 94, 95, [NW2007] 109
235	5 35 1.6	-5 2 24.4	0.10	1.1	0.06	1.1	2.0	A	C^{18}O -Ori 102
236	5 35 2.0	-5 38 6.4	0.92	1.1	0.11	25.1	8.1	D	[ISK2007] 56, 57, [NW2007] 13
237	5 35 2.0	-5 15 24.4	0.49	1.1	0.05	5.6	17.5	A	C^{18}O -Ori 96, [ISK2007] 48, 54, 64, [NW2007] 100
238	5 35 2.4	-5 27 42.4	0.15	1.1	0.09	2.2	1.2	A	C^{18}O -Ori 99, [NW2007] 37
239	5 35 2.8	-6 18 18.1	0.13	1.3	0.09	2.2	1.2	...	
240	5 35 2.8	-6 11 54.2	0.09	1.4	0.12	2.6	0.6	...	
241	5 35 2.8	-5 36 6.4	1.23	1.1	0.04	20.4	142.8	A	C^{18}O -Ori 107, [ISK2007] 61, [NW2007] 22, [TKU2008] 23
242	5 35 2.9	-5 1 0.4	0.10	1.3	0.08	1.5	1.2	B	C^{18}O -Ori 93, 101
243	5 35 2.9	-4 58 54.4	0.20	1.1	0.04	2.1	10.9	D	[ISK2007] 53, [NW2007] 166
244	5 35 3.2	-6 9 30.2	0.09	1.2	0.11	2.0	0.6	...	
245	5 35 3.3	-5 20 36.4	0.21	1.1	0.08	3.7	3.1	D	[ISK2007] 65, 70, [NW2007] 66, 69
246	5 35 3.6	-6 35 47.7	0.08	1.1	0.05	0.7	2.3	...	
247	5 35 3.6	-6 19 30.1	0.11	1.3	0.09	1.8	1.1	...	
248	5 35 3.6	-5 51 18.4	0.34	1.2	0.10	7.6	3.1	...	1 PMS star, [ISK2007] 76
249	5 35 4.4	-5 57 24.3	0.18	1.1	0.13	6.5	1.2	...	
250	5 35 4.5	-5 24 24.4	0.63	1.5	0.09	10.9	6.6	B	C^{18}O -Ori 104, 112, 1 PMS star, [ISK2007] 72, 73, [NW2007] 43, [TKU2008] 20

Table 2—Continued

ID AzTEC-Ori	RA (J2000)	DEC (J2000)	Peak flux density [Jy beam $^{-1}$]	Aspect ratio major/minor	R_{core} [pc]	M_{H_2} [M_{\odot}]	n [$\times 10^4 \text{cm}^{-3}$]	category	note † ‡
251	5 35 4.8	-6 11 24.2	0.14	1.5	0.05	1.7	4.9	...	
252	5 35 4.9	-5 37 18.4	1.11	1.1	0.03	16.3	206.4	A	C^{18}O -Ori 114, 1 protostar, [ISK2007] 75, [NW2007] 16, [TKU2008] 24
253	5 35 4.9	-5 35 0.4	1.22	1.0	0.07	26.7	29.8	D	1 protostar, [ISK2007] 74, [NW2007] 25
254	5 35 4.9	-4 57 18.4	0.69	1.2	0.09	16.3	8.7	A	C^{18}O -Ori 108, 1 PMS star, [ISK2007] 63, [NW2007] 169
255	5 35 5.2	-6 15 48.1	0.23	1.4	0.17	12.8	1.1	...	
256	5 35 5.3	-5 13 18.4	0.14	2.3	0.10	2.6	0.9	D	
257	5 35 5.7	-5 33 12.4	0.79	1.7	0.11	18.2	6.0	D	[NW2007] 29
258	5 35 6.1	-4 54 30.4	1.05	1.1	0.16	35.5	3.4	D	[ISK2007] 68, [TKU2008] 1
259	5 35 6.5	-4 56 24.4	0.94	1.5	0.10	24.5	10.0	D	[ISK2007] 69, [NW2007] 172, [TKU2008] 2
260	5 35 7.3	-5 56 42.3	0.41	1.0	0.03	5.1	62.8	...	
261	5 35 8.1	-5 51 24.4	0.65	1.3	0.10	7.7	3.3	...	[ISK2007] 81
262	5 35 8.1	-5 35 54.4	1.40	1.1	0.05	17.6	69.0	D	1 protostar, [NW2007] 23
263	5 35 8.5	-6 4 0.3	0.23	1.3	0.16	8.0	0.9	...	[NW2007] 230
264	5 35 8.5	-4 44 18.5	0.10	1.6	0.12	2.7	0.7	...	
265	5 35 8.9	-6 6 0.3	0.21	1.2	0.10	3.4	1.6	...	[NW2007] 226
266	5 35 8.9	-6 0 24.3	0.20	1.3	0.10	4.1	1.8	...	[ISK2007] 90
267	5 35 8.9	-5 58 24.3	0.62	1.1	0.10	12.5	4.8	...	1 protostar, [ISK2007] 103
268	5 35 8.9	-5 55 48.3	1.25	1.1	0.09	14.7	9.3	...	1 protostar, [ISK2007] 89, 109, [TKU2008] 30
269	5 35 8.9	-5 53 12.3	0.25	2.5	0.07	2.8	2.9	...	[ISK2007] 102
270	5 35 8.9	-5 31 54.4	0.18	1.5	0.08	2.6	2.1	D	1 PMS star
271	5 35 9.3	-5 52 12.4	0.54	2.0	0.08	6.3	5.2	...	[TKU2008] 28
272	5 35 10.1	-5 37 54.4	0.46	1.2	0.15	11.4	1.5	B	C^{18}O -Ori 138, 142, [NW2007] 14
273	5 35 10.1	-5 35 6.4	1.18	1.1	0.13	32.8	6.8	B	C^{18}O -Ori 137, 145, 1 protostar, [ISK2007] 88, [NW2007] 24
274	5 35 10.5	-6 13 54.2	0.68	1.0	0.18	28.8	2.0	...	[NW2007] 213
275	5 35 11.3	-5 0 0.4	0.75	1.1	0.09	11.5	7.8	D	[ISK2007] 83, 92, [NW2007] 162
276	5 35 11.7	-6 28 47.9	0.07	1.2	0.06	0.9	1.3	...	
277	5 35 11.7	-6 10 48.2	0.11	1.6	0.09	2.2	1.1	...	
278	5 35 12.1	-6 7 36.2	0.10	1.4	0.06	1.0	1.7	...	
279	5 35 12.1	-5 57 12.3	0.44	1.1	0.05	6.0	16.0	...	
280	5 35 12.1	-5 8 48.4	0.14	1.6	0.09	2.4	1.3	D	
281	5 35 12.5	-6 1 18.3	0.17	1.0	0.09	3.2	2.1	...	[NW2007] 232
282	5 35 13.7	-5 58 0.3	0.77	1.3	0.03	8.1	86.4	...	1 protostar, [ISK2007] 125, [TKU2008] 31
283	5 35 13.7	-5 10 0.4	0.30	1.2	0.03	2.6	35.8	D	[NW2007] 121, 125
284	5 35 13.7	-4 54 54.4	0.50	2.0	0.11	12.5	3.5	D	
285	5 35 14.5	-5 10 24.4	0.30	1.2	0.04	4.0	19.7	D	
286	5 35 14.5	-6 4 24.3	0.07	1.2	0.09	1.1	0.7	...	
287	5 35 14.9	-5 33 12.4	0.37	1.5	0.11	7.9	2.8	A	C^{18}O -Ori 158, 2 PMS stars, [NW2007] 30
288	5 35 15.3	-5 16 0.4	0.50	1.4	0.03	4.6	101.3	B	C^{18}O -Ori 162, 163, 164, 1 PMS star, [ISK2007] 130, 137, [NW2007] 95
289	5 35 15.7	-4 55 12.4	0.51	1.4	0.09	9.1	5.0	A	C^{18}O -Ori 166
290	5 35 16.5	-5 15 12.4	0.59	1.1	0.01	6.6	915.0	A	C^{18}O -Ori 171, [ISK2007] 129, 149, [NW2007] 102
291	5 35 16.9	-4 56 12.4	0.49	1.8	0.16	19.0	1.9	A	C^{18}O -Ori 178, [NW2007] 171
292	5 35 16.9	-5 12 12.4	0.54	1.2	0.09	12.8	6.7	A	C^{18}O -Ori 161, [ISK2007] 126, [NW2007] 114, 115
293	5 35 16.9	-5 30 42.4	0.46	1.1	0.14	12.8	1.9	A	C^{18}O -Ori 175, 3 PMS stars, [ISK2007] 140, [NW2007] 31
294	5 35 17.3	-5 59 36.3	0.22	1.2	0.06	3.6	7.2	...	[ISK2007] 141, [NW2007] 233
295	5 35 17.3	-6 22 6.0	0.08	1.2	0.08	1.1	0.8	...	
296	5 35 17.7	-5 2 24.4	0.49	1.0	0.10	7.1	3.4	D	[ISK2007] 135, [NW2007] 151
297	5 35 17.7	-5 58 12.3	0.25	1.5	0.06	3.8	8.8	...	1 PMS star
298	5 35 18.5	-5 0 30.4	3.28	1.3	0.16	82.4	8.8	A	C^{18}O -Ori 180, 1 protostar, 1 PMS star, [ISK2007] 142, [NW2007] 161, [TKU2008] 4
299	5 35 18.5	-5 14 0.4	0.51	1.2	0.04	6.8	46.1	D	[NW2007] 106, 108
300	5 35 18.5	-5 28 24.4	0.37	1.1	0.06	3.5	6.9	D	1 protostar, 1 PMS star, [NW2007] 35

Table 2—Continued

ID AzTEC-Ori	RA (J2000)	DEC (J2000)	Peak flux density [Jy beam $^{-1}$]	Aspect ratio major/minor	R_{core} [pc]	M_{H_2} [M_{\odot}]	n [$\times 10^4 \text{cm}^{-3}$]	category	note [†]	‡
301	5 35 18.5	-5 56 6.3	0.17	1.1	0.07	2.2	3.0	...		
302	5 35 18.9	-5 9 12.4	0.46	2.6	0.09	9.3	5.3	D	[ISK2007] 146, [NW2007] 127	
303	5 35 18.9	-6 0 24.3	0.24	1.3	0.07	4.1	5.9	...	[ISK2007] 162, [NW2007] 233	
304	5 35 20.1	-5 5 6.4	1.17	1.1	0.18	46.8	3.5	D	1 protostar, [ISK2007] 145, 151, [NW2007] 147	
305	5 35 20.1	-5 59 0.3	0.23	1.1	0.05	3.3	9.8	...	[ISK2007] 153, 161	
306	5 35 20.5	-6 21 12.1	0.13	1.1	0.10	2.4	1.1	...		
307	5 35 20.9	-6 1 42.3	0.14	1.0	0.08	2.5	2.3	...	[ISK2007] 154	
308	5 35 21.3	-5 42 24.4	0.07	1.0	0.11	1.8	0.6	D	1 PMS star	
309	5 35 21.3	-6 13 12.2	0.25	1.0	0.14	6.7	1.1	...	1 protostar, [ISK2007] 169, [NW2007] 214	
310	5 35 21.7	-5 14 24.4	1.09	1.0	0.04	13.9	86.2	A	C^{18}O -Ori 190, [ISK2007] 159, [NW2007] 104, 105, [TKU2008] 13	
311	5 35 22.5	-5 49 18.4	0.09	1.1	0.09	1.7	1.0	...		
312	5 35 22.5	-6 3 12.3	0.23	1.0	0.10	5.2	2.0	...	[NW2007] 231	
313	5 35 22.9	-5 54 54.3	0.15	1.3	0.09	2.8	1.5	...		
314	5 35 23.3	-4 39 18.5	0.15	1.4	0.11	3.6	1.1	...		
315	5 35 23.3	-5 1 24.4	4.87	1.1	0.12	56.6	12.2	D	1 protostar, [ISK2007] 163, [NW2007] 155, 157	
316	5 35 23.3	-5 12 30.4	2.84	1.1	0.15	80.6	11.0	B	C^{18}O -Ori 189, 193, [ISK2007] 167, 170, [NW2007] 112, 116, [TKU2008] 12	
317	5 35 23.3	-5 43 12.4	0.07	1.1	0.06	0.8	1.7	D		
318	5 35 23.3	-6 5 0.3	0.12	1.2	0.12	3.1	0.7	...	1 PMS star	
319	5 35 23.7	-5 32 18.4	0.08	1.0	0.09	1.3	0.8	D		
320	5 35 24.1	-5 7 48.4	2.45	1.3	0.13	78.6	15.8	D	1 PMS star, [ISK2007] 165, [NW2007] 134, 135, [TKU2008] 9	
321	5 35 24.2	-6 19 18.1	0.09	1.0	0.09	1.6	0.9	...		C†
322	5 35 24.5	-5 15 30.4	0.48	1.4	0.10	10.2	3.8	D	1 PMS star, [NW2007] 98	C†
323	5 35 25.4	-5 52 12.3	0.48	1.6	0.14	15.6	2.2	...	[ISK2007] 175	
324	5 35 25.4	-5 59 30.3	0.24	1.6	0.08	4.6	4.3	...	[ISK2007] 177	
325	5 35 26.1	-5 5 36.4	2.15	1.2	0.07	39.5	55.4	A	C^{18}O -Ori 197, 2 protostars, [ISK2007] 179, [NW2007] 144, 146	
326	5 35 26.5	-5 3 48.4	1.64	1.1	0.12	31.6	6.9	A	C^{18}O -Ori 196, 1 protostar, [ISK2007] 178, [NW2007] 149	
327	5 35 27.0	-5 9 54.4	5.95	1.1	0.18	117.0	8.1	D	2 protostars, 1 PMS star, [ISK2007] 184, [NW2007] 120, 123, 126, [TKU2008] 10	
328	5 35 27.4	-5 48 48.4	0.07	1.7	0.09	1.3	0.9	...	1 PMS star	
329	5 35 27.8	-5 7 12.4	0.77	1.2	0.07	12.1	16.0	A	C^{18}O -Ori 202, 1 PMS star, [ISK2007] 183, [NW2007] 136, 137	
330	5 35 27.8	-5 28 12.4	0.15	1.0	0.10	3.2	1.2	D	1 PMS star, [NW2007] 36	
331	5 35 27.8	-5 59 48.3	0.26	1.5	0.08	4.6	3.4	...	[ISK2007] 193, [NW2007] 234, [TKU2008] 32	
332	5 35 28.6	-5 53 30.3	0.43	1.0	0.14	15.2	2.5	...	[ISK2007] 192	
333	5 35 28.6	-6 20 0.1	0.15	1.1	0.13	3.6	0.6	...		
334	5 35 29.0	-5 13 54.4	0.15	1.5	0.07	2.3	3.0	D		
335	5 35 29.0	-6 1 54.3	0.11	1.6	0.08	1.7	1.5	...		
336	5 35 29.4	-5 36 30.4	0.14	1.0	0.14	3.7	0.6	D	[NW2007] 20	
337	5 35 29.8	-4 58 42.4	1.53	1.4	0.20	44.2	2.3	A	C^{18}O -Ori 201, 1 protostar, [ISK2007] 186, 187, [NW2007] 167, [TKU2008] 3	
338	5 35 29.8	-6 26 53.9	0.83	1.8	0.20	24.0	1.2	...	1 protostar, [NW2007] 191, 195	
339	5 35 30.2	-4 38 54.5	0.08	1.8	0.07	1.2	1.2	...		
340	5 35 30.6	-5 40 6.4	0.16	1.2	0.12	4.2	1.1	D		
341	5 35 30.6	-5 41 6.4	0.07	1.7	0.09	1.8	0.9	D		
342	5 35 30.6	-5 51 48.3	0.24	1.1	0.07	4.4	5.7	...	2 PMS stars	
343	5 35 30.6	-5 52 30.3	0.37	1.6	0.08	4.5	3.8	...	1 PMS star, [ISK2007] 197	
344	5 35 32.2	-5 5 42.4	1.29	1.4	0.09	22.3	11.6	A	C^{18}O -Ori 204, 1 protostar, 1 PMS star, [ISK2007] 198, [NW2007] 145, [TKU2008] 8	
345	5 35 32.2	-5 20 48.4	1.02	1.2	0.08	17.6	12.7	A	C^{18}O -Ori 206, [NW2007] 65	
346	5 35 32.6	-5 57 30.3	0.15	1.7	0.11	3.1	1.1	...		
347	5 35 33.0	-5 30 24.4	0.11	1.0	0.14	4.4	0.6	D	1 PMS star	
348	5 35 33.4	-5 19 12.4	0.23	1.0	0.08	3.2	3.1	D	[NW2007] 74	
349	5 35 33.8	-5 42 0.4	0.08	1.1	0.09	1.6	0.9	D		
350	5 35 33.8	-5 50 36.3	0.19	1.6	0.11	4.3	1.3	...		

Table 2—Continued

ID AzTEC-Ori	RA (J2000)	DEC (J2000)	Peak flux density [Jy beam $^{-1}$]	Aspect ratio major/minor	R_{core} [pc]	M_{H_2} [M_{\odot}]	n [$\times 10^4 \text{ cm}^{-3}$]	category	note [†] [‡]
351	5 35 33.8	-6 12 48.2	0.12	1.3	0.11	2.5	0.9	...	[NW2007] 218
352	5 35 33.8	-6 28 53.9	0.11	1.0	0.12	3.2	0.7	...	
353	5 35 34.6	-5 13 54.4	0.23	2.1	0.07	3.2	3.6	D	[NW2007] 107
354	5 35 35.0	-5 8 18.4	0.16	1.9	0.08	2.2	2.1	A	C^{18}O -Ori 208, [NW2007] 131
355	5 35 35.4	-5 51 0.3	0.20	1.4	0.15	5.3	0.7	...	
356	5 35 35.4	-6 14 6.1	0.13	1.2	0.13	3.9	0.8	...	
357	5 35 35.8	-6 18 6.1	0.11	1.0	0.11	2.5	0.9	...	
358	5 35 36.2	-5 15 48.4	0.67	1.3	0.15	21.3	2.9	D	1 PMS star, [NW2007] 96
359	5 35 36.6	-6 5 36.2	0.30	1.1	0.16	12.7	1.4	...	[ISK2007] 204, [NW2007] 227
360	5 35 36.6	-6 27 17.9	0.09	1.2	0.09	1.9	1.1	...	
361	5 35 37.4	-5 23 48.4	0.20	1.3	0.07	2.6	3.8	D	
362	5 35 37.4	-5 37 12.4	0.07	1.6	0.10	1.3	0.6	D	
363	5 35 37.4	-6 9 42.2	0.19	1.7	0.12	4.0	1.1	...	[NW2007] 222
364	5 35 37.8	-5 1 6.4	0.19	2.0	0.09	3.2	1.9	A	C^{18}O -Ori 214, [NW2007] 158
365	5 35 37.8	-5 18 30.4	0.54	1.2	0.09	10.1	5.9	A	C^{18}O -Ori 212, [NW2007] 80, 84
366	5 35 37.8	-6 28 11.9	0.11	1.1	0.07	1.2	1.3	...	[ISK2007] 206
367	5 35 38.2	-5 6 12.4	0.54	1.1	0.13	15.2	2.8	A	C^{18}O -Ori 211, [NW2007] 141, 142
368	5 35 38.2	-5 29 0.4	0.07	1.3	0.10	1.8	0.7	D	
369	5 35 38.6	-5 17 12.4	0.48	1.3	0.08	7.1	5.2	D	1 PMS star, [NW2007] 89
370	5 35 39.4	-5 56 48.3	0.11	1.1	0.08	2.1	1.6	...	
371	5 35 40.2	-5 24 42.4	0.26	1.4	0.08	4.3	3.8	D	1 PMS star
372	5 35 40.6	-5 58 6.3	0.07	1.6	0.07	1.2	1.5	...	
373	5 35 40.6	-5 59 36.3	0.09	1.3	0.09	1.6	0.9	...	[ISK2007] 208
374	5 35 40.6	-6 5 42.2	0.27	1.2	0.11	7.3	2.4	...	[ISK2007] 209, [NW2007] 228
375	5 35 41.0	-6 7 24.2	0.27	1.1	0.10	7.0	3.1	...	
376	5 35 41.4	-5 0 36.4	0.07	1.4	0.09	1.1	0.7	D	
377	5 35 41.4	-5 2 24.4	0.29	1.2	0.10	4.1	1.6	D	[ISK2007] 207, [NW2007] 152
378	5 35 41.9	-6 4 0.2	0.09	1.6	0.11	2.1	0.7	...	
379	5 35 42.2	-5 30 36.4	0.16	1.5	0.11	3.7	1.3	D	
380	5 35 42.3	-6 18 54.0	0.06	1.7	0.10	1.5	0.6	...	
381	5 35 42.6	-5 13 30.4	0.13	1.1	0.09	2.5	1.4	D	
382	5 35 42.6	-5 20 54.4	0.61	1.4	0.08	9.7	7.5	A	C^{18}O -Ori 216, 1 PMS star, [NW2007] 62
383	5 35 42.6	-5 42 12.3	0.06	1.2	0.07	0.8	1.2	D	
384	5 35 43.5	-6 7 48.2	0.32	1.1	0.12	7.0	1.7	...	[NW2007] 223
385	5 35 43.5	-6 10 6.2	0.18	1.3	0.11	5.3	1.8	...	
386	5 35 43.8	-5 7 42.4	0.15	1.0	0.07	1.9	2.2	D	[ISK2007] 210
387	5 35 44.2	-5 10 36.4	0.15	1.0	0.09	2.0	1.3	A	C^{18}O -Ori 218
388	5 35 44.6	-5 25 18.4	0.47	1.3	0.09	9.7	6.6	D	
389	5 35 44.7	-6 25 59.9	0.13	1.3	0.09	2.2	1.4	...	
390	5 35 45.0	-5 19 30.4	0.29	1.1	0.12	6.4	1.5	A	C^{18}O -Ori 219
391	5 35 45.0	-5 41 24.3	0.07	1.1	0.07	1.1	1.6	D	
392	5 35 45.4	-5 12 42.4	0.09	1.0	0.09	1.3	0.7	D	
393	5 35 45.8	-5 26 24.3	0.44	1.3	0.10	10.1	3.9	D	
394	5 35 45.9	-6 1 54.2	0.08	1.1	0.11	2.0	0.7	...	
395	5 35 45.9	-6 11 42.1	0.08	1.9	0.10	2.0	0.8	...	
396	5 35 46.6	-5 5 36.4	0.11	1.4	0.05	1.0	2.8	D	
397	5 35 46.6	-5 23 42.3	0.33	1.2	0.11	8.1	2.3	A	C^{18}O -Ori 223
398	5 35 46.7	-6 25 29.9	0.09	1.2	0.06	1.1	2.1	...	
399	5 35 47.0	-5 21 24.3	0.48	1.1	0.09	8.1	4.4	A	C^{18}O -Ori 222
400	5 35 47.1	-6 29 41.8	0.12	1.4	0.11	2.8	0.9	...	

Table 2—Continued

ID AzTEC-Ori	RA (J2000)	DEC (J2000)	Peak flux density [Jy beam $^{-1}$]	Aspect ratio major/minor	R_{core} [pc]	M_{H_2} [M_{\odot}]	n [$\times 10^4 \text{cm}^{-3}$]	category	note † ‡
401	5 35 48.2	-5 8 18.3	0.19	1.0	0.08	3.0	2.1	D	
402	5 35 48.3	-5 40 30.3	0.06	1.7	0.07	0.8	1.0	D	
403	5 35 49.0	-5 5 48.3	0.10	1.0	0.08	1.5	1.2	D	
404	5 35 49.1	-5 27 36.3	0.40	1.3	0.11	11.2	3.6	D	
405	5 35 49.1	-6 30 35.8	0.09	1.2	0.04	0.7	4.1	...	
406	5 35 49.5	-6 10 30.1	0.21	1.5	0.09	4.8	2.8	...	
407	5 35 49.9	-5 29 48.3	0.52	2.4	0.08	11.8	10.5	D	1 PMS star
408	5 35 49.9	-5 31 6.3	0.50	1.2	0.14	23.6	3.4	D	
409	5 35 50.3	-5 22 12.3	0.38	1.4	0.10	7.6	3.6	D	
410	5 35 50.3	-5 45 42.3	0.16	1.4	0.15	5.7	0.7	...	
411	5 35 50.7	-5 29 18.3	0.48	1.8	0.12	13.2	3.6	D	
412	5 35 51.1	-5 33 12.3	0.23	1.4	0.09	4.8	3.2	D	
413	5 35 51.1	-5 41 42.3	0.56	1.3	0.09	8.7	5.7	A	C ¹⁸ O-Ori 226
414	5 35 51.5	-6 34 53.7	0.44	1.2	0.13	7.2	1.3	...	[NW2007] 183
415	5 35 51.9	-6 3 48.2	0.09	1.3	0.07	1.1	1.1	...	
416	5 35 52.2	-4 56 12.4	0.08	1.2	0.08	1.6	1.2	...	
417	5 35 52.3	-5 43 48.3	0.18	1.0	0.07	2.4	2.7	D	
418	5 35 52.3	-6 10 6.1	0.43	1.1	0.09	5.5	3.4	...	1 protostar, [ISK2007] 211, [NW2007] 221
419	5 35 52.6	-4 57 36.4	0.08	1.3	0.08	1.4	1.3	...	
420	5 35 52.7	-6 26 35.9	0.14	1.1	0.10	3.0	1.3	...	[NW2007] 192
421	5 35 53.1	-6 24 29.9	0.09	1.1	0.09	1.8	0.9	...	[NW2007] 203
422	5 35 53.5	-5 44 30.3	0.21	1.1	0.07	4.1	4.7	D	
423	5 35 54.3	-5 7 54.3	0.08	1.0	0.10	1.5	0.6	...	
424	5 35 54.3	-5 20 0.3	0.07	1.2	0.08	1.0	0.8	...	
425	5 35 54.3	-5 41 54.3	0.44	1.4	0.12	10.8	2.6	D	
426	5 35 55.1	-5 15 36.3	0.07	1.4	0.07	0.9	1.2	...	
427	5 35 55.1	-5 25 0.3	0.10	1.1	0.07	1.6	1.8	D	
428	5 35 55.1	-5 34 24.3	0.35	1.1	0.17	16.0	1.5	D	
429	5 35 55.1	-5 55 36.2	0.06	1.2	0.10	1.2	0.5	...	
430	5 35 55.2	-6 43 53.4	0.11	2.0	0.08	1.8	1.4	...	
431	5 35 55.5	-5 32 30.3	0.20	1.3	0.14	6.8	1.1	D	
432	5 35 55.5	-5 39 12.3	0.07	1.3	0.10	1.4	0.6	D	
433	5 35 56.3	-5 26 24.3	0.08	1.3	0.07	1.2	1.4	D	
434	5 35 56.7	-5 23 0.3	0.17	1.4	0.07	2.7	2.8	D	
435	5 35 57.2	-6 25 59.9	0.14	1.2	0.08	2.1	1.6	...	[NW2007] 197
436	5 35 57.5	-5 18 42.3	0.11	1.5	0.10	2.3	1.1	...	
437	5 35 57.5	-5 27 30.3	0.09	1.0	0.10	2.0	0.9	D	
438	5 35 57.5	-5 56 6.2	0.06	1.0	0.06	0.7	1.2	...	
439	5 35 58.0	-6 12 54.1	0.12	1.1	0.12	3.6	0.8	...	
440	5 35 58.0	-6 43 29.4	0.14	1.7	0.07	2.0	2.6	...	
441	5 35 58.3	-5 15 30.3	0.06	1.2	0.08	1.0	0.8	...	
442	5 35 58.3	-5 44 0.3	0.17	1.4	0.13	4.9	0.9	D	
443	5 35 58.3	-5 52 6.2	0.06	1.2	0.10	1.2	0.6	...	
444	5 35 58.4	-6 32 29.7	0.17	1.0	0.11	3.6	1.1	...	
445	5 35 58.7	-5 37 12.3	0.18	1.7	0.12	4.6	1.2	D	1 PMS star
446	5 35 58.8	-6 8 48.1	0.08	1.5	0.12	1.9	0.5	...	
447	5 35 59.1	-4 57 36.3	0.10	1.6	0.08	1.9	1.8	...	
448	5 35 59.2	-6 10 54.1	0.13	1.2	0.09	3.2	1.7	...	
449	5 35 59.2	-6 31 53.7	0.18	1.3	0.09	3.0	1.5	...	
450	5 35 59.6	-6 23 41.9	0.09	1.5	0.10	1.6	0.7	...	

Table 2—Continued

ID AzTEC-Ori	RA (J2000)	DEC (J2000)	Peak flux density [Jy beam ⁻¹]	Aspect ratio major/minor	R_{core} [pc]	M_{H_2} [M_{\odot}]	n [$\times 10^4 \text{cm}^{-3}$]	category	note [†] [‡]
451	5 35 59.9	-5 20 12.3	0.07	1.2	0.07	1.0	1.1	...	
452	5 36 0.3	-5 37 54.3	0.20	1.2	0.11	4.4	1.5	A	C^{18}O -Ori 230
453	5 36 0.7	-5 16 36.3	0.08	1.3	0.08	1.5	1.2	...	
454	5 36 0.7	-5 56 48.2	0.07	1.4	0.11	1.9	0.6	...	
455	5 36 1.1	-5 36 18.3	0.09	1.0	0.08	1.8	1.3	D	
456	5 36 1.9	-4 57 24.3	0.10	1.9	0.09	1.8	1.1	...	
457	5 36 1.9	-5 18 24.3	0.08	1.6	0.08	1.3	1.2	...	
458	5 36 2.0	-6 12 36.1	0.15	1.8	0.07	2.5	2.9	...	
459	5 36 2.0	-6 23 17.9	0.09	1.1	0.09	1.4	0.8	...	
460	5 36 2.4	-6 43 53.3	0.15	1.2	0.11	3.5	1.2	...	
461	5 36 2.8	-6 13 54.0	0.14	1.3	0.11	3.1	1.0	...	
462	5 36 3.1	-5 24 0.3	0.21	1.0	0.10	4.5	1.9	D	
463	5 36 3.2	-5 53 6.2	0.13	1.1	0.12	3.7	0.8	...	
464	5 36 3.9	-5 22 6.3	0.10	1.1	0.09	1.8	1.1	D	
465	5 36 4.0	-6 11 6.1	0.23	1.9	0.11	7.2	2.6	...	
466	5 36 4.7	-5 13 48.3	0.06	1.1	0.07	0.8	0.9	...	
467	5 36 4.7	-5 41 54.3	0.14	1.3	0.10	3.3	1.5	A	C^{18}O -Ori 231
468	5 36 5.1	-5 35 12.3	0.06	1.6	0.09	1.3	0.6	A	C^{18}O -Ori 232
469	5 36 5.5	-5 19 48.3	0.11	1.0	0.08	1.5	1.1	...	
470	5 36 5.6	-6 40 59.4	0.08	1.5	0.09	1.2	0.7	...	
471	5 36 5.9	-5 18 24.3	0.08	1.2	0.06	1.0	1.8	...	
472	5 36 6.4	-5 52 0.2	0.10	1.1	0.09	1.8	1.0	...	
473	5 36 6.7	-5 17 6.3	0.06	1.3	0.09	1.1	0.7	...	
474	5 36 7.1	-5 25 12.3	0.15	1.1	0.09	2.9	1.6	D	
475	5 36 7.2	-5 41 54.2	0.11	1.4	0.11	2.0	0.7	D	1 PMS star
476	5 36 7.2	-6 15 12.0	0.08	1.2	0.11	2.2	0.6	...	
477	5 36 7.2	-6 37 29.5	0.10	1.6	0.08	1.5	1.0	...	
478	5 36 7.6	-6 29 47.7	0.10	1.2	0.08	1.4	1.0	...	
479	5 36 8.0	-6 32 41.6	0.13	1.1	0.12	3.8	0.9	...	
480	5 36 8.1	-6 46 17.2	0.11	1.3	0.08	1.9	1.4	...	
481	5 36 8.4	-6 30 47.7	0.08	1.0	0.05	1.0	2.7	...	
482	5 36 9.2	-5 35 30.2	0.27	1.6	0.11	5.0	1.4	B	C^{18}O -Ori 234, 235
483	5 36 9.2	-5 37 54.2	0.06	1.3	0.09	1.3	0.6	D	
484	5 36 9.3	-6 44 29.3	0.09	1.3	0.09	1.7	0.9	...	
485	5 36 10.0	-5 33 6.2	0.08	1.7	0.08	1.1	1.0	D	
486	5 36 10.3	-5 20 42.2	0.10	1.1	0.06	1.3	2.2	...	
487	5 36 10.3	-5 23 24.2	0.24	1.5	0.10	5.1	2.3	D	
488	5 36 10.8	-6 10 36.0	0.76	1.0	0.14	14.8	2.2	...	[ISK2007] 213, 214, 215, [NW2007] 220, [TKU2008] 33
489	5 36 10.8	-6 23 11.8	0.26	1.6	0.10	5.2	2.3	...	
490	5 36 10.8	-6 25 11.8	0.20	1.3	0.11	4.7	1.4	...	
491	5 36 11.6	-5 24 36.2	0.14	1.3	0.10	2.8	1.2	D	
492	5 36 11.6	-6 14 00.0	0.06	1.1	0.08	1.0	0.8	...	
493	5 36 12.1	-6 33 41.6	0.21	1.1	0.09	3.6	1.9	...	[NW2007] 184
494	5 36 12.1	-6 48 53.1	0.19	1.2	0.11	4.7	1.7	...	
495	5 36 14.0	-6 14 41.9	0.15	1.3	0.10	3.7	1.4	...	
496	5 36 14.4	-6 12 42.0	0.13	1.2	0.09	2.5	1.4	...	
497	5 36 14.8	-5 31 36.2	0.09	1.1	0.09	1.8	1.0	D	
498	5 36 14.8	-5 34 42.2	0.11	1.3	0.12	2.7	0.6	D	
499	5 36 14.9	-6 30 35.6	0.10	1.2	0.07	1.6	1.8	...	
500	5 36 16.5	-6 31 41.6	0.14	1.3	0.10	2.8	1.3	...	

|
G
88
|

Table 2—Continued

ID AzTEC-Ori	RA (J2000)	DEC (J2000)	Peak flux density [Jy beam $^{-1}$]	Aspect ratio major/minor	R_{core} [pc]	M_{H_2} [M_{\odot}]	n [$\times 10^4 \text{cm}^{-3}$]	category	note [†] [‡]
501	5 36 17.3	-6 33 41.5	0.12	1.0	0.08	2.4	1.6	...	
502	5 36 17.3	-6 37 59.4	0.25	1.1	0.09	3.1	1.6	...	1 protostar, [NW2007] 181
503	5 36 18.0	-5 30 36.2	0.05	1.7	0.06	0.7	1.3	D	
504	5 36 18.5	-6 12 12.0	0.29	1.0	0.10	6.0	2.3	...	[ISK2007] 216, [NW2007] 219
505	5 36 18.5	-6 45 29.2	1.35	1.4	0.13	22.2	4.6	...	1 protostar, [NW2007] 176
506	5 36 18.5	-6 47 17.1	0.40	1.2	0.14	16.0	2.3	...	[NW2007] 173
507	5 36 18.9	-6 22 11.8	2.95	1.5	0.17	49.5	4.0	...	4 protostars, [ISK2007] 218, 220, [NW2007] 209
508	5 36 18.9	-6 29 11.6	0.16	1.5	0.09	2.1	1.3	...	1 protostar, [NW2007] 187
509	5 36 19.6	-5 31 24.2	0.08	1.2	0.08	1.2	0.9	D	
510	5 36 19.7	-6 15 17.9	0.12	1.1	0.10	2.6	1.1	...	
511	5 36 20.4	-5 28 36.2	0.13	1.2	0.14	3.9	0.6	D	
512	5 36 20.4	-5 46 12.1	0.06	1.1	0.11	1.4	0.5	...	
513	5 36 21.3	-6 30 35.6	0.17	1.0	0.11	4.2	1.5	...	
514	5 36 21.7	-6 1 30.0	0.30	1.1	0.14	7.4	1.1	...	
515	5 36 22.1	-6 13 5.9	0.40	1.0	0.09	7.3	4.2	...	[ISK2007] 221, 222, [NW2007] 215, 216
516	5 36 22.1	-6 34 17.5	0.11	1.5	0.09	1.9	1.1	...	
517	5 36 22.4	-5 30 6.2	0.09	1.4	0.07	1.2	1.2	D	
518	5 36 22.5	-5 56 12.1	0.45	1.2	0.15	10.9	1.5	...	
519	5 36 22.9	-5 58 0.1	0.06	1.5	0.11	1.3	0.5	...	
520	5 36 22.9	-6 36 5.4	0.09	1.1	0.09	1.3	0.8	...	
521	5 36 23.0	-6 46 5.1	1.54	1.0	0.07	21.6	22.8	...	2 protostars, [NW2007] 175
522	5 36 24.1	-6 23 41.7	0.58	2.2	0.08	13.3	13.3	...	[ISK2007] 224, [NW2007] 207
523	5 36 24.9	-6 14 5.9	0.66	1.2	0.10	11.7	5.7	...	[ISK2007] 225, [NW2007] 212, [TKU2008] 34
524	5 36 24.9	-6 22 41.7	0.87	1.4	0.09	15.0	9.8	...	1 protostar, [ISK2007] 226, [NW2007] 208
525	5 36 24.9	-6 24 53.7	1.39	1.9	0.13	27.9	5.3	...	3 protostars, [ISK2007] 227, [NW2007] 202
526	5 36 24.9	-6 32 23.5	0.09	1.1	0.10	1.9	0.8	...	
527	5 36 25.4	-6 41 41.2	0.10	1.4	0.08	1.3	1.2	...	
528	5 36 25.4	-6 44 41.1	0.67	1.2	0.15	16.7	2.1	...	1 protostar, [NW2007] 177
529	5 36 25.6	-5 24 54.1	0.07	1.5	0.11	1.5	0.4	D	
530	5 36 25.7	-6 6 48.0	0.14	1.5	0.13	3.6	0.7	...	
531	5 36 26.5	-6 1 48.0	0.23	2.4	0.11	6.1	1.8	...	
532	5 36 27.0	-6 47 23.0	0.27	1.1	0.14	7.5	1.1	...	[NW2007] 174
533	5 36 27.3	-5 56 54.0	0.26	1.4	0.11	4.0	1.3	...	
534	5 36 27.7	-6 20 23.7	0.16	1.8	0.09	3.1	1.9	...	
535	5 36 29.7	-6 15 17.8	0.35	1.2	0.12	8.8	2.3	...	[ISK2007] 228, [NW2007] 210
536	5 36 30.0	-5 21 30.1	0.07	1.0	0.07	0.9	1.2	D	
537	5 36 30.9	-5 58 6.0	0.16	1.3	0.09	2.4	1.2	...	
538	5 36 30.9	-6 5 53.9	0.09	1.3	0.12	3.1	0.8	...	
539	5 36 31.2	-5 26 36.1	0.08	1.1	0.13	2.8	0.6	D	
540	5 36 31.3	-6 7 23.9	0.13	1.2	0.10	3.4	1.4	...	
541	5 36 31.8	-6 25 17.6	0.42	1.2	0.11	8.9	2.7	...	[NW2007] 200
542	5 36 32.1	-6 1 12.0	0.63	1.4	0.10	10.6	4.6	...	1 protostar
543	5 36 32.1	-6 2 00.0	0.57	1.1	0.05	8.9	23.9	...	
544	5 36 32.2	-6 21 41.7	0.09	1.2	0.10	2.2	0.8	...	
545	5 36 32.2	-6 26 23.6	0.39	1.2	0.11	9.8	2.7	...	[ISK2007] 229, [NW2007] 193
546	5 36 33.4	-6 21 11.7	0.07	1.1	0.07	1.2	1.2	...	
547	5 36 33.8	-6 38 17.3	0.26	1.2	0.08	3.1	3.0	...	[NW2007] 180
548	5 36 35.0	-6 7 59.9	0.08	1.5	0.09	1.7	0.9	...	
549	5 36 35.3	-5 26 0.1	0.09	1.0	0.10	1.7	0.9	...	
550	5 36 35.3	-5 28 30.1	0.08	1.8	0.10	1.6	0.8	...	

Table 2—Continued

ID AzTEC-Ori	RA (J2000)	DEC (J2000)	Peak flux density [Jy beam $^{-1}$]	Aspect ratio major/minor	R_{core} [pc]	M_{H_2} [M_{\odot}]	n [$\times 10^4 \text{ cm}^{-3}$]	category	note [†] [‡]
551	5 36 35.3	-6 2 53.9	0.46	1.0	0.15	16.8	2.3	...	
552	5 36 35.8	-6 9 29.8	0.16	1.6	0.13	3.9	0.7	...	
553	5 36 36.1	-6 0 59.9	0.11	1.9	0.10	2.1	0.9	...	
554	5 36 36.2	-6 38 53.2	0.76	1.1	0.12	7.9	2.1	...	[NW2007] 179
555	5 36 36.6	-6 12 59.8	0.15	1.8	0.06	1.3	2.8	...	[ISK2007] 231, [NW2007] 217
556	5 36 37.0	-6 6 17.9	0.14	1.2	0.08	2.4	1.8	...	
557	5 36 37.0	-6 14 59.8	0.33	1.6	0.09	4.5	2.7	...	1 PMS star, [NW2007] 211
558	5 36 38.2	-6 5 47.9	0.13	1.2	0.07	2.4	2.4	...	
559	5 36 38.3	-6 50 10.8	0.12	1.1	0.05	1.0	3.1	...	
560	5 36 38.6	-6 17 47.7	0.13	1.2	0.09	3.1	1.7	...	
561	5 36 38.9	-5 26 42.0	0.12	1.2	0.10	3.5	1.5	...	
562	5 36 39.4	-6 11 35.8	0.14	1.2	0.07	1.8	1.8	...	
563	5 36 39.4	-6 14 11.7	0.13	1.1	0.04	1.3	9.5	...	
564	5 36 39.8	-6 22 17.6	0.07	1.1	0.09	1.2	0.7	...	
565	5 36 41.4	-6 26 17.5	0.81	1.2	0.14	21.5	3.4	...	[ISK2007] 232, [NW2007] 194
566	5 36 41.4	-6 28 29.5	0.12	1.3	0.08	2.1	1.5	...	[NW2007] 188
567	5 36 42.3	-6 35 5.3	0.09	1.1	0.06	1.2	1.8	...	
568	5 36 42.6	-6 12 47.7	0.09	1.2	0.07	1.3	1.8	...	
569	5 36 43.0	-6 3 11.8	0.11	2.0	0.06	1.3	2.8	...	
570	5 36 43.8	-6 19 5.6	0.09	1.4	0.07	1.0	1.4	...	
571	5 36 44.5	-5 26 6.0	0.10	1.1	0.07	1.3	1.7	...	
572	5 36 44.5	-5 36 30.0	0.06	1.5	0.10	1.1	0.5	...	
573	5 36 44.6	-6 3 47.8	0.09	1.1	0.08	1.2	1.2	...	
574	5 36 44.6	-6 21 29.6	0.16	1.2	0.09	2.6	1.6	...	
575	5 36 45.3	-5 27 12.0	0.09	1.0	0.07	1.6	2.0	...	
576	5 36 45.4	-6 6 5.8	0.23	1.1	0.15	7.5	0.9	...	
577	5 36 45.9	-6 25 29.5	0.13	1.1	0.07	1.5	2.2	...	
578	5 36 46.2	-6 15 47.6	0.13	1.4	0.08	2.0	1.8	...	
579	5 36 46.6	-6 19 53.6	0.07	1.4	0.08	1.0	0.8	...	
580	5 36 46.7	-6 30 47.3	0.14	1.2	0.08	2.2	1.9	...	
581	5 36 47.1	-6 23 23.5	0.10	1.0	0.08	1.5	1.0	...	
582	5 36 47.5	-6 31 41.3	0.10	1.3	0.09	1.7	1.1	...	
583	5 36 47.7	-5 25 54.0	0.09	1.9	0.09	1.8	0.9	...	
584	5 36 48.3	-6 26 17.4	0.11	1.4	0.06	1.4	3.0	...	
585	5 36 49.1	-6 21 11.5	0.15	1.0	0.11	3.3	1.1	...	
586	5 36 49.3	-5 27 23.9	0.07	1.1	0.10	1.4	0.7	...	
587	5 36 49.4	-6 8 11.7	0.07	1.2	0.11	2.0	0.6	...	
588	5 36 49.5	-6 28 47.4	0.41	1.0	0.12	9.5	2.5	...	[ISK2007] 235, [NW2007] 189
589	5 36 50.7	-6 16 35.6	0.12	1.0	0.10	2.1	0.8	...	
590	5 36 50.7	-6 25 53.4	0.10	1.5	0.08	1.5	1.0	...	
591	5 36 51.1	-6 29 35.3	0.27	1.3	0.07	4.3	4.4	...	[ISK2007] 236, [NW2007] 186
592	5 36 52.3	-6 8 29.7	0.10	1.1	0.10	2.0	0.9	...	
593	5 36 54.3	-6 31 29.2	0.10	2.1	0.10	2.4	1.0	...	
594	5 36 55.5	-6 34 41.1	0.15	1.6	0.09	2.3	1.5	...	
595	5 36 55.8	-5 32 17.9	0.08	2.3	0.09	1.3	0.7	...	
596	5 36 57.9	-6 28 53.2	0.10	1.0	0.07	1.1	1.4	...	
597	5 36 57.9	-6 30 11.2	0.08	1.3	0.07	1.1	1.4	...	
598	5 36 58.8	-6 31 17.2	0.19	1.2	0.07	3.2	3.3	...	[NW2007] 185
599	5 36 60.0	-6 35 11.1	0.31	1.8	0.07	4.8	5.9	...	
600	5 37 0.8	-6 37 11.0	0.63	2.5	0.15	13.5	1.6	...	1 protostar, [NW2007] 182

Table 2—Continued

ID AzTEC-Ori	RA (J2000)	DEC (J2000)	Peak flux density [Jy beam ⁻¹]	Aspect ratio major/minor	R_{core} [pc]	M_{H_2} [M_{\odot}]	n [$\times 10^4 \text{cm}^{-3}$]	category	note [†] [‡]
601	5 37 2.4	-6 35 11.0	0.24	1.6	0.05	2.8	12.0	...	
602	5 37 5.6	-6 35 47.0	0.23	1.1	0.12	7.0	1.6	...	
603	5 37 6.0	-6 25 41.2	0.08	1.4	0.09	1.2	0.6	...	
604	5 37 10.2	-5 27 17.7	0.06	1.1	0.08	1.1	0.8	...	
605	5 37 11.3	-6 42 40.7	0.14	1.3	0.09	2.2	1.4	...	
606	5 37 12.5	-6 39 28.8	0.17	1.3	0.12	3.6	0.8	...	
607	5 37 14.1	-6 46 28.5	0.13	1.2	0.08	1.8	1.8	...	
608	5 37 16.9	-6 40 22.7	0.09	1.0	0.10	2.1	1.0	...	
609	5 37 17.9	-5 28 23.6	0.07	1.4	0.07	0.9	1.3	...	
610	5 37 18.0	-6 3 59.4	0.07	2.3	0.13	1.7	0.3	...	
611	5 37 23.3	-6 36 46.7	0.12	1.2	0.06	1.2	2.7	...	
612	5 37 26.7	-5 31 17.5	0.08	1.5	0.11	1.8	0.6	...	
613	5 37 31.4	-6 41 58.4	0.15	1.8	0.06	1.9	3.5	...	
614	5 38 14.2	-5 52 22.6	0.08	1.1	0.09	1.3	0.9	...	
615	5 38 21.3	-5 13 52.7	0.12	1.0	0.14	3.3	0.5	...	
616	5 38 28.1	-5 13 22.5	0.08	1.0	0.07	1.1	1.2	...	
617	5 38 36.5	-5 13 52.4	0.08	1.3	0.08	1.3	1.0	...	
618	5 38 45.3	-6 7 27.7	0.11	1.5	0.06	1.1	2.2	...	
619	5 38 54.0	-5 49 39.7	0.16	1.3	0.11	4.0	1.2	...	

[†][NW2007] #, [ISK2007] #, and [TKU2008] # are the SCUBA 850 μm dust core from Nutter & Ward-Thompson (2007), the H¹³CO⁺ (1–0) core from Ikeda et al. (2007), and the N₂H⁺ (1–0) core from Tatematsu et al. (2008), respectively.

[‡]The Spitzer YSOs and Disk sources, respectively, cataloged by Megeath et al. (2012)

Table 3. Physical properties of the C¹⁸O cores

Property	Bound			Unbound			Total		
	Mean [†]	Minimum	Maximum	Mean [†]	Minimum	Maximum	Mean [†]	Minimum	Maximum
$M_{\text{LTE}} [M_{\odot}]$	15.3 ± 10.7	1.3	61.8	4.4 ± 2.5	1.0	13.4	12.4 ± 10.4	1.0	61.8
$dV_{\text{core}} [\text{km s}^{-1}]$	0.59 ± 0.13	0.31	1.02	0.66 ± 0.18	0.40	1.31	0.61 ± 0.14	0.31	1.31
$R_{\text{core}} [\text{pc}]$	0.23 ± 0.04	0.13	0.34	0.21 ± 0.04	0.13	0.32	0.23 ± 0.04	0.13	0.34
$n [\times 10^3 \text{ cm}^{-3}]$	4.8 ± 2.8	1.1	17.5	2.0 ± 1.1	0.8	5.6	4.1 ± 2.8	0.8	17.5
\mathcal{R}_{vir}	1.5 ± 0.7	0.4	3.0	5.0 ± 2.8	3.1	20.1	2.4 ± 2.2	0.4	20.1
$M_J [M_{\odot}]$	3.0 ± 2.7	0.2	20.2	5.6 ± 8.9	0.5	55.6	3.7 ± 5.2	0.2	55.6
$M_{\phi} [M_{\odot}]$	0.4 ± 0.1	0.1	0.8	0.3 ± 0.1	0.1	0.7	0.4 ± 0.1	0.1	0.8
\mathcal{R}_c	5.5 ± 3.4	1.1	20.8	1.3 ± 0.7	0.1	2.6	4.4 ± 3.5	0.1	20.8

[†]Errors are the standard deviation

Table 4. Identified C¹⁸O cores

ID C ¹⁸ O-Ori	RA (J2000)	DEC (J2000)	V_{LSR} [km s ⁻¹]	T_{peak} [K]	Aspect	R_{core} [pc]	dV_{core} [km s ⁻¹]	σ [km s ⁻¹]	M_{LTE} [M_{\odot}]	M_{VIR} [M_{\odot}]	\mathcal{R}_{vir}	M_J [M_{\odot}]	M_{Φ} [M_{\odot}]	\mathcal{R}_c	n [$\times 10^4 \text{ cm}^{-3}$]	area	category	note
1	5 33 44.4	-5 28 19.0	8.0	1.7	1.2	0.20	0.63	0.27	8.8	16.7	1.9	3.0	0.3	2.7	0.5	Bending	C	
2	5 33 50.4	-5 31 19.0	8.4	1.2	1.3	0.24	0.59	0.25	6.6	17.4	2.7	2.3	0.4	2.4	0.2	Bending	C	
3	5 33 51.9	-5 35 26.5	8.0	1.9	1.7	0.25	0.55	0.23	8.7	15.8	1.8	1.7	0.4	4.0	0.2	Bending	A	AzTEC-Ori 69
4	5 33 53.4	-5 32 26.5	7.9	1.8	1.1	0.24	0.54	0.23	8.5	14.8	1.7	1.6	0.4	4.2	0.3	Bending	C	
5	5 33 53.4	-5 22 41.5	8.1	3.2	1.3	0.24	0.50	0.21	15.0	12.1	0.8	1.1	0.4	9.8	0.5	Bending	A	AzTEC-Ori 72
6	5 33 56.4	-5 29 49.0	8.1	3.3	1.2	0.20	0.61	0.26	17.2	15.1	0.9	2.6	0.3	6.1	1.0	Bending	A	AzTEC-Ori 75
7	5 33 56.4	-5 27 11.5	7.8	0.9	1.1	0.23	0.44	0.19	2.6	9.3	3.6	0.7	0.4	2.4	0.1	Bending	A	AzTEC-Ori 71
8	5 33 57.9	-5 24 11.5	8.3	3.5	1.1	0.26	0.58	0.25	23.1	18.8	0.8	2.2	0.5	8.7	0.5	Bending	C	
9	5 33 59.4	-5 28 41.5	8.0	3.7	1.2	0.22	0.51	0.22	13.9	12.2	0.9	1.3	0.3	8.4	0.5	Bending	A	AzTEC-Ori 79
10	5 34 0.9	-5 30 56.5	8.4	3.5	1.2	0.22	0.66	0.28	23.0	19.9	0.9	3.6	0.3	5.9	0.9	Bending	C	
11	5 34 0.9	-5 26 49.0	8.7	1.9	1.2	0.28	0.53	0.22	15.7	16.4	1.0	1.5	0.6	7.8	0.3	Bending	A	AzTEC-Ori 81
12	5 34 2.4	-5 32 4.0	8.3	3.5	1.2	0.27	0.76	0.32	34.2	32.2	0.9	6.3	0.5	5.0	0.8	Bending	A	AzTEC-Ori 87
13	5 34 10.0	-5 36 56.5	8.3	2.5	1.1	0.31	0.71	0.30	27.6	32.7	1.2	4.8	0.7	5.1	0.4	Bending	C	
14	5 34 13.0	-5 28 19.0	8.3	1.5	1.0	0.21	0.48	0.21	7.4	10.3	1.4	1.0	0.3	5.5	0.3	Bending	A	AzTEC-Ori 102
15	5 34 16.0	-5 29 4.0	9.0	1.3	1.0	0.23	0.49	0.21	6.6	11.7	1.8	1.1	0.4	4.4	0.2	Bending	C	
16	5 34 17.5	-5 36 56.5	7.7	3.3	1.2	0.26	0.56	0.24	20.3	17.3	0.9	1.9	0.5	8.5	0.5	Bending	A	AzTEC-Ori 105
17	5 34 17.5	-5 26 26.5	8.2	1.2	1.1	0.22	0.44	0.19	5.9	8.9	1.5	0.7	0.3	5.7	0.2	Bending	B	AzTEC-Ori 110
18	5 34 19.0	-5 34 19.0	7.2	0.8	1.1	0.26	0.59	0.25	4.2	19.3	4.6	2.4	0.5	1.5	0.1	Bending	C	
19	5 34 19.0	-5 30 11.5	8.5	1.5	1.1	0.24	0.56	0.24	7.8	15.7	2.0	1.9	0.4	3.4	0.2	Bending	A	AzTEC-Ori 109
20	5 34 19.0	-5 27 11.5	8.9	1.6	1.1	0.22	0.58	0.25	6.1	15.7	2.6	2.1	0.4	2.5	0.2	Bending	B	AzTEC-Ori 110
21	5 34 20.5	-5 38 26.5	8.3	2.9	1.1	0.27	0.66	0.28	18.6	24.5	1.3	3.6	0.5	4.6	0.4	Bending	C	
22	5 34 26.6	-5 24 34.0	8.2	2.9	1.2	0.24	0.68	0.29	18.7	22.7	1.2	4.0	0.4	4.3	0.6	Bending	A	AzTEC-Ori 138
23	5 34 26.6	-5 33 56.5	7.9	2.9	1.9	0.27	0.59	0.25	16.5	19.3	1.2	2.3	0.5	5.9	0.4	Bending	A	AzTEC-Ori 131
24	5 34 26.6	-5 35 26.5	7.8	2.7	1.7	0.18	0.65	0.28	10.8	15.6	1.4	3.3	0.2	3.0	0.8	Bending	C	
25	5 34 28.1	-5 26 26.5	7.7	2.4	1.2	0.21	0.55	0.23	10.2	13.4	1.3	1.7	0.3	5.0	0.4	Bending	A	AzTEC-Ori 137
26	5 34 28.1	-5 32 4.0	8.1	2.0	1.4	0.27	0.62	0.26	13.8	21.5	1.6	2.8	0.5	4.1	0.3	Bending	A	AzTEC-Ori 136
27	5 34 28.1	-5 39 34.0	9.4	0.9	1.1	0.28	1.31	0.56	5.1	101.9	20.1	55.6	0.6	0.1	0.1	Bending	A	AzTEC-Ori 135
28	5 34 29.6	-5 29 26.5	9.7	1.0	2.2	0.27	0.66	0.28	5.3	24.4	4.6	3.6	0.5	1.3	0.1	Bending	C	
29	5 34 29.6	-5 36 34.0	7.7	2.7	1.0	0.23	0.65	0.28	20.7	20.5	1.0	3.4	0.4	5.5	0.7	Bending	C	
30	5 34 31.1	-5 21 56.5	8.0	1.8	1.2	0.18	0.60	0.25	5.6	13.4	2.4	2.5	0.2	2.1	0.4	Bending	C	
31	5 34 31.1	-5 40 41.5	8.9	1.2	1.1	0.30	0.87	0.37	11.3	47.6	4.2	10.7	0.6	1.0	0.2	Bending	C	
32	5 34 32.6	-4 54 11.5	10.5	1.7	1.3	0.21	0.55	0.23	6.8	13.3	2.0	1.7	0.3	3.4	0.3	OMC-2/3	A	AzTEC-Ori 150
33	5 34 32.6	-5 36 34.0	9.8	1.3	1.5	0.13	0.35	0.15	1.3	3.3	2.6	0.3	0.1	3.1	0.3	Bending	C	
34	5 34 34.1	-5 24 56.5	9.5	2.1	1.1	0.27	0.79	0.34	15.9	35.5	2.2	7.4	0.5	2.0	0.3	Bending	C	
35	5 34 34.1	-5 40 19.0	7.8	2.5	1.1	0.32	0.65	0.28	22.2	27.7	1.2	3.4	0.7	5.5	0.3	Bending	A	AzTEC-Ori 153
36	5 34 35.6	-4 54 34.0	11.5	1.3	1.1	0.16	0.46	0.20	2.9	7.3	2.5	0.9	0.2	2.7	0.3	OMC-2/3	C	
37	5 34 35.6	-5 17 4.0	9.9	1.2	1.0	0.16	0.40	0.17	2.9	5.4	1.8	0.5	0.2	4.5	0.3	OMC-1	A	AzTEC-Ori 156
38	5 34 38.6	-4 53 4.0	11.5	1.7	1.3	0.18	0.49	0.21	4.9	9.0	1.8	1.1	0.2	3.8	0.3	OMC-2/3	C	
39	5 34 38.6	-5 41 4.0	7.2	0.8	1.2	0.23	0.38	0.16	3.1	6.9	2.2	0.4	0.4	4.1	0.1	Bending	C	
40	5 34 40.1	-5 26 49.0	8.8	1.8	1.1	0.26	0.60	0.26	15.1	20.1	1.3	2.5	0.5	5.0	0.3	Bending	B	AzTEC-Ori 162
41	5 34 40.1	-5 37 41.5	8.0	2.5	1.3	0.26	0.79	0.34	22.8	34.5	1.5	7.5	0.5	2.9	0.5	Bending	A	AzTEC-Ori 163
42	5 34 41.6	-5 11 26.5	11.0	1.5	1.2	0.21	0.59	0.25	7.2	15.1	2.1	2.3	0.3	2.7	0.3	OMC-2/3	C	
43	5 34 41.6	-5 26 26.5	7.5	0.9	1.2	0.16	0.53	0.23	1.7	9.3	5.5	1.5	0.2	1.0	0.2	Bending	B	AzTEC-Ori 162
44	5 34 41.6	-5 28 19.0	7.9	2.3	1.3	0.21	0.51	0.22	9.1	11.5	1.3	1.3	0.3	5.6	0.4	Bending	A	AzTEC-Ori 167
45	5 34 41.6	-5 30 11.5	7.8	2.2	1.1	0.22	0.48	0.20	9.1	10.5	1.2	1.0	0.3	6.9	0.3	Bending	C	
46	5 34 41.6	-5 31 41.5	7.2	2.2	1.3	0.28	0.69	0.29	19.6	27.9	1.4	4.3	0.5	4.0	0.4	Bending	A	AzTEC-Ori 164
47	5 34 43.1	-4 52 19.0	10.8	0.8	1.1	0.22	0.46	0.20	3.2	9.8	3.1	0.9	0.3	2.6	0.1	OMC-2/3	C	
48	5 34 43.1	-4 53 49.0	11.3	1.4	1.0	0.23	0.66	0.28	6.7	21.0	3.1	3.6	0.4	1.7	0.2	OMC-2/3	C	
49	5 34 44.6	-5 15 11.5	10.0	0.8	1.1	0.13	0.45	0.19	1.0	5.7	6.0	0.8	0.1	1.0	0.2	OMC-2/3	C	
50	5 34 44.6	-5 29 4.0	8.2	2.4	1.2	0.21	0.40	0.17	8.8	7.0	0.8	0.5	0.3	11.1	0.4	Bending	C	

Table 4—Continued

ID C^{18}O -Ori	RA (J2000)	DEC (J2000)	V_{LSR} [km s $^{-1}$]	T_{peak} [K]	Aspect	R_{core} [pc]	dV_{core} [km s $^{-1}$]	σ [km s $^{-1}$]	M_{LTE} [M_{\odot}]	M_{VIR} [M_{\odot}]	\mathcal{R}_{vir}	M_{J} [M_{\odot}]	M_{Φ} [M_{\odot}]	\mathcal{R}_{c}	n [$\times 10^4 \text{ cm}^{-3}$]	area	category	note
51	5 34 47.7	-5 25 19.0	9.3	0.8	1.4	0.21	0.53	0.22	3.2	12.4	3.9	1.4	0.3	1.8	0.1	Bending	C	
52	5 34 47.7	-5 30 56.5	8.3	2.0	1.0	0.21	0.50	0.21	6.0	10.6	1.8	1.1	0.3	4.2	0.3	Bending	A	AzTEC-Ori 181
53	5 34 47.7	-5 40 19.0	6.4	0.8	1.2	0.27	0.72	0.31	4.4	29.5	6.6	5.2	0.5	0.8	0.1	OMC-4	C	
54	5 34 49.1	-4 53 26.5	10.7	2.0	1.1	0.24	0.51	0.22	10.4	13.1	1.3	1.3	0.4	6.2	0.3	OMC-2/3	A	AzTEC-Ori 188
55	5 34 49.1	-4 55 19.0	10.6	3.0	1.5	0.24	0.77	0.33	12.8	29.6	2.3	6.8	0.4	1.8	0.4	OMC-2/3	A	AzTEC-Ori 182
56	5 34 49.2	-5 18 56.5	10.7	1.1	1.2	0.15	0.41	0.17	1.7	5.1	3.0	0.5	0.1	2.6	0.2	OMC-1	A	AzTEC-Ori 184
57	5 34 49.2	-5 20 26.5	10.8	0.9	1.0	0.14	0.63	0.27	1.6	11.2	7.0	2.9	0.1	0.5	0.3	OMC-1	C	
58	5 34 49.2	-5 29 49.0	8.7	2.1	1.0	0.21	0.55	0.23	6.5	12.9	2.0	1.7	0.3	3.3	0.3	Bending	C	
59	5 34 49.2	-5 40 19.0	10.1	0.8	1.6	0.24	0.53	0.23	3.2	14.0	4.4	1.5	0.4	1.7	0.1	OMC-4	C	
60	5 34 50.7	-5 4 41.5	10.7	0.8	1.3	0.27	0.57	0.24	4.8	18.4	3.8	2.0	0.5	1.9	0.1	OMC-2/3	C	
61	5 34 50.7	-5 9 56.5	10.7	1.1	1.3	0.16	0.61	0.26	2.3	12.5	5.5	2.6	0.2	0.8	0.2	OMC-2/3	C	
62	5 34 50.7	-5 36 11.5	8.0	1.0	1.4	0.22	0.38	0.16	3.5	6.7	1.9	0.4	0.3	4.7	0.1	OMC-4	C	
63	5 34 50.7	-5 38 49.0	7.7	3.3	1.2	0.24	0.72	0.30	20.8	26.1	1.3	5.0	0.4	3.9	0.6	OMC-4	A	AzTEC-Ori 189
64	5 34 50.7	-5 42 34.0	7.5	3.6	1.1	0.22	0.65	0.28	22.2	18.9	0.8	3.3	0.3	6.1	0.9	OMC-4	A	AzTEC-Ori 191
65	5 34 52.2	-4 56 49.0	10.9	3.0	1.0	0.18	0.62	0.26	10.5	14.2	1.4	2.9	0.2	3.4	0.8	OMC-2/3	A	AzTEC-Ori 195
66	5 34 52.2	-5 6 56.5	11.4	1.4	1.0	0.17	0.66	0.28	4.7	15.7	3.4	3.7	0.2	1.2	0.4	OMC-2/3	A	AzTEC-Ori 194
67	5 34 52.2	-5 19 19.0	9.6	1.4	1.6	0.22	0.58	0.25	6.6	16.0	2.4	2.2	0.4	2.6	0.2	OMC-1	C	
68	5 34 52.2	-5 27 56.5	7.8	1.2	1.4	0.17	0.39	0.17	2.9	5.6	2.0	0.5	0.2	4.3	0.2	Bending	C	
69	5 34 52.2	-5 36 34.0	7.4	2.0	1.2	0.28	0.73	0.31	19.7	31.5	1.6	5.5	0.5	3.3	0.4	OMC-4	C	
70	5 34 52.2	-5 37 19.0	8.1	1.0	1.3	0.20	0.58	0.25	3.5	13.7	3.9	2.1	0.3	1.5	0.2	OMC-4	C	
71	5 34 53.7	-5 8 49.0	11.3	1.3	1.4	0.19	0.36	0.15	3.7	5.0	1.4	0.3	0.2	6.7	0.2	OMC-2/3	64	
72	5 34 55.2	-5 8 4.0	10.7	1.2	1.3	0.23	0.65	0.28	6.5	20.3	3.1	3.4	0.4	1.7	0.2	OMC-2/3	C	
73	5 34 55.2	-5 23 49.0	11.1	1.6	1.1	0.27	0.54	0.23	11.9	16.6	1.4	1.6	0.5	5.5	0.3	OMC-1	C	
74	5 34 55.2	-5 32 4.0	8.2	1.1	1.3	0.22	0.77	0.33	6.0	27.3	4.6	6.6	0.3	0.9	0.2	OMC-4	C	
75	5 34 55.2	-5 35 4.0	9.0	1.0	1.6	0.23	0.52	0.22	3.6	12.6	3.5	1.3	0.4	2.1	0.1	OMC-4	C	
76	5 34 56.7	-4 55 19.0	11.1	3.9	1.4	0.22	0.62	0.26	21.3	17.7	0.8	2.7	0.3	6.9	0.8	OMC-2/3	A	AzTEC-Ori 206
77	5 34 56.7	-5 20 4.0	9.9	0.8	1.0	0.18	0.47	0.20	2.9	8.3	2.9	0.9	0.2	2.5	0.2	OMC-1	C	
78	5 34 56.7	-5 20 49.0	8.3	2.9	1.2	0.22	1.02	0.43	21.9	47.1	2.2	20.2	0.3	1.1	0.9	OMC-1	C	
79	5 34 56.7	-5 23 49.0	12.1	1.3	1.1	0.24	0.53	0.22	4.7	13.9	3.0	1.5	0.4	2.5	0.1	OMC-1	C	
80	5 34 56.7	-5 24 11.5	11.8	1.7	1.1	0.20	0.33	0.14	5.1	4.5	0.9	0.2	0.3	10.2	0.3	OMC-1	A	AzTEC-Ori 202
81	5 34 56.7	-5 33 11.5	7.0	2.3	1.4	0.24	0.68	0.29	17.7	22.8	1.3	4.0	0.4	4.0	0.6	OMC-4	C	
82	5 34 56.7	-5 35 26.5	8.4	0.8	1.2	0.20	0.50	0.21	3.3	10.3	3.1	1.2	0.3	2.3	0.2	OMC-4	C	
83	5 34 56.7	-5 42 11.5	7.3	3.4	1.0	0.25	0.67	0.28	26.1	23.5	0.9	3.7	0.5	6.3	0.7	OMC-4	A	AzTEC-Ori 215
84	5 34 56.7	-5 42 34.0	9.0	4.7	1.1	0.26	0.66	0.28	42.2	23.6	0.6	3.5	0.5	10.5	1.0	OMC-4	C	
85	5 34 58.2	-5 5 26.5	11.5	1.8	1.1	0.28	0.74	0.31	15.7	32.2	2.1	5.6	0.6	2.5	0.3	OMC-2/3	A	AzTEC-Ori 205
86	5 34 58.2	-5 12 11.5	10.8	2.0	1.2	0.24	0.55	0.23	13.9	15.6	1.1	1.8	0.4	6.4	0.4	OMC-2/3	A	AzTEC-Ori 218
87	5 34 58.2	-5 41 4.0	8.7	3.8	1.5	0.28	0.60	0.25	28.3	21.3	0.8	2.4	0.6	9.4	0.5	OMC-4	C	
88	5 34 59.7	-4 58 19.0	10.8	2.3	1.0	0.24	0.68	0.29	15.7	22.8	1.5	4.0	0.4	3.5	0.5	OMC-2/3	A	AzTEC-Ori 229
89	5 34 59.7	-5 16 41.5	10.3	0.8	1.3	0.17	0.47	0.20	2.3	8.1	3.5	1.0	0.2	2.0	0.2	OMC-1	B	AzTEC-Ori 232
90	5 34 59.7	-5 16 41.5	8.5	1.2	1.0	0.26	0.51	0.22	7.6	14.5	1.9	1.3	0.5	4.2	0.2	OMC-1	B	AzTEC-Ori 232
91	5 34 59.7	-5 19 19.0	10.2	0.9	1.2	0.18	0.46	0.19	2.3	7.8	3.4	0.8	0.2	2.2	0.2	OMC-1	C	
92	5 34 59.7	-5 39 11.5	9.1	3.6	1.0	0.28	0.64	0.27	23.8	24.2	1.0	3.2	0.5	6.3	0.5	OMC-4	C	
93	5 35 1.2	-5 1 19.0	11.3	2.0	1.3	0.29	0.62	0.26	13.3	22.9	1.7	2.8	0.6	4.0	0.2	OMC-2/3	B	AzTEC-Ori 242
94	5 35 1.2	-5 13 19.0	10.2	2.7	1.2	0.21	0.38	0.16	8.8	6.2	0.7	0.4	0.3	12.7	0.4	OMC-2/3	B	AzTEC-Ori 234
95	5 35 1.2	-5 13 41.5	9.9	3.1	1.2	0.21	0.53	0.22	12.1	12.1	1.0	1.4	0.3	6.9	0.6	OMC-2/3	B	AzTEC-Ori 234
96	5 35 1.2	-5 15 34.0	9.4	3.1	1.3	0.25	0.70	0.30	21.3	25.5	1.2	4.6	0.4	4.3	0.6	OMC-2/3	A	AzTEC-Ori 237
97	5 35 1.2	-5 18 11.5	8.4	1.7	1.6	0.21	0.52	0.22	7.1	11.9	1.7	1.4	0.3	4.1	0.3	OMC-1	A	AzTEC-Ori 231
98	5 35 1.2	-5 19 41.5	8.2	1.7	1.5	0.17	0.81	0.34	5.7	23.4	4.1	8.2	0.2	0.7	0.5	OMC-1	C	
99	5 35 1.2	-5 27 34.0	8.9	1.0	1.4	0.23	0.73	0.31	5.1	25.6	5.0	5.3	0.4	0.9	0.2	OMC-1	A	AzTEC-Ori 238
100	5 35 2.7	-4 55 19.0	11.1	3.4	1.3	0.21	0.60	0.25	21.1	16.1	0.8	2.4	0.3	7.7	0.9	OMC-2/3	C	

Table 4—Continued

ID C^{18}O -Ori	RA (J2000)	DEC (J2000)	V_{LSR} [km s $^{-1}$]	T_{peak} [K]	Aspect	R_{core} [pc]	dV_{core} [km s $^{-1}$]	σ [km s $^{-1}$]	M_{LTE} [M_{\odot}]	M_{VIR} [M_{\odot}]	\mathcal{R}_{vir}	M_J [M_{\odot}]	M_{Φ} [M_{\odot}]	\mathcal{R}_c	n [$\times 10^4 \text{ cm}^{-3}$]	area	category	note
101	5 35 2.7	-5 0 56.5	12.3	1.6	1.2	0.23	0.39	0.16	4.9	7.1	1.5	0.4	0.4	6.2	0.2	OMC-2/3	B	AzTEC-Ori 242
102	5 35 2.7	-5 2 49.0	12.4	0.8	1.2	0.18	0.45	0.19	2.4	7.9	3.2	0.8	0.2	2.4	0.2	OMC-2/3	A	AzTEC-Ori 235
103	5 35 2.7	-5 23 26.5	10.1	1.3	1.4	0.27	0.62	0.27	10.5	21.6	2.1	2.9	0.5	3.1	0.2	OMC-1	C	
104	5 35 2.7	-5 24 34.0	9.5	1.6	1.2	0.30	0.59	0.25	14.3	21.9	1.5	2.3	0.6	4.9	0.2	OMC-1	B	AzTEC-Ori 250
105	5 35 2.7	-5 25 41.5	11.8	1.7	1.2	0.23	0.75	0.32	11.4	26.5	2.3	5.9	0.4	1.8	0.4	OMC-1	C	
106	5 35 2.7	-5 35 26.5	6.5	4.0	1.1	0.34	0.52	0.22	33.2	19.2	0.6	1.3	0.8	15.2	0.3	OMC-4	C	
107	5 35 2.7	-5 36 11.5	7.1	5.5	1.3	0.27	0.57	0.24	45.9	18.7	0.4	2.1	0.5	17.8	1.0	OMC-4	A	AzTEC-Ori 241
108	5 35 4.2	-4 57 34.0	11.5	4.2	1.1	0.27	0.57	0.24	28.0	18.7	0.7	2.1	0.5	10.9	0.6	OMC-2/3	A	AzTEC-Ori 254
109	5 35 4.2	-5 12 11.5	10.0	1.6	1.3	0.25	0.59	0.25	11.0	18.2	1.7	2.4	0.4	3.9	0.3	OMC-2/3	C	
110	5 35 4.2	-5 17 49.0	7.8	1.3	1.8	0.24	0.64	0.27	5.8	20.2	3.5	3.1	0.4	1.6	0.2	OMC-1	C	
111	5 35 4.2	-5 18 56.5	9.6	1.3	1.5	0.22	0.70	0.30	8.6	22.1	2.6	4.5	0.3	1.8	0.4	OMC-1	C	
112	5 35 4.2	-5 24 34.0	8.3	1.6	1.5	0.16	0.67	0.28	5.4	14.6	2.7	3.7	0.2	1.4	0.6	OMC-1	B	AzTEC-Ori 250
113	5 35 4.2	-5 32 4.0	10.2	0.9	1.0	0.22	0.49	0.21	3.8	10.9	2.9	1.1	0.3	2.6	0.2	OMC-4	C	
114	5 35 4.2	-5 37 41.5	8.7	3.8	1.0	0.27	0.59	0.25	24.1	19.9	0.8	2.3	0.5	8.5	0.5	OMC-4	A	AzTEC-Ori 252
115	5 35 5.7	-5 0 11.5	9.8	1.2	1.3	0.21	0.66	0.28	3.5	19.2	5.5	3.6	0.3	0.9	0.2	OMC-2/3	C	
116	5 35 5.7	-5 0 56.5	11.8	1.2	1.0	0.29	0.42	0.18	8.6	10.4	1.2	0.6	0.6	7.5	0.2	OMC-2/3	C	
117	5 35 5.7	-5 9 34.0	11.3	0.8	1.2	0.25	0.75	0.32	4.9	29.7	6.1	5.9	0.5	0.8	0.1	OMC-2/3	C	
118	5 35 5.7	-5 10 41.5	10.6	1.6	1.3	0.24	0.65	0.27	12.5	21.2	1.7	3.3	0.4	3.4	0.4	OMC-2/3	C	
119	5 35 5.7	-5 20 49.0	8.0	1.3	1.2	0.23	0.64	0.27	9.4	19.2	2.0	3.1	0.4	2.7	0.3	OMC-1	C	
120	5 35 5.7	-5 22 41.5	6.7	1.6	1.1	0.19	0.54	0.23	4.1	11.3	2.8	1.6	0.2	2.2	0.3	OMC-1	.↓.	
121	5 35 5.7	-5 23 4.0	8.3	1.6	1.2	0.15	0.73	0.31	9.3	16.5	1.8	5.3	0.2	1.7	1.2	OMC-1	G	
122	5 35 5.7	-5 24 56.5	7.4	0.9	1.4	0.16	0.46	0.19	2.2	7.0	3.3	0.8	0.2	2.1	0.2	OMC-1	G	
123	5 35 5.7	-5 26 49.0	11.4	1.2	1.4	0.26	0.68	0.29	10.4	24.4	2.4	3.9	0.5	2.4	0.3	OMC-1	G	
124	5 35 5.7	-5 31 19.0	10.8	0.8	1.2	0.25	0.71	0.30	3.3	25.9	7.9	4.8	0.4	0.6	0.1	OMC-4	C	
125	5 35 5.8	-5 39 11.5	7.6	2.0	1.1	0.24	0.68	0.29	17.7	22.8	1.3	4.0	0.4	4.0	0.6	OMC-4	C	
126	5 35 7.2	-5 15 34.0	9.5	3.2	1.4	0.22	0.68	0.29	23.9	21.5	0.9	4.1	0.3	5.4	0.9	OMC-2/3	C	
127	5 35 7.2	-5 23 4.0	6.3	1.2	1.1	0.18	1.17	0.50	5.3	52.0	9.8	35.7	0.2	0.1	0.4	OMC-1	...	
128	5 35 7.2	-5 31 19.0	12.5	1.2	1.8	0.16	0.71	0.30	2.7	16.9	6.3	4.8	0.2	0.5	0.3	OMC-4	C	
129	5 35 8.7	-4 55 19.0	12.6	2.2	1.2	0.22	0.55	0.23	7.5	14.0	1.9	1.7	0.3	3.6	0.3	OMC-2/3	C	
130	5 35 8.7	-4 59 49.0	9.8	1.2	1.1	0.28	0.70	0.30	9.0	28.8	3.2	4.5	0.6	1.8	0.2	OMC-2/3	C	
131	5 35 8.7	-5 2 4.0	10.8	1.2	1.2	0.22	0.64	0.27	9.2	19.2	2.1	3.2	0.4	2.6	0.3	OMC-2/3	C	
132	5 35 8.7	-5 12 11.5	8.0	1.2	1.0	0.19	0.44	0.19	3.0	7.7	2.6	0.7	0.3	3.1	0.2	OMC-2/3	C	
133	5 35 8.7	-5 17 4.0	8.0	0.9	1.2	0.22	0.42	0.18	3.4	8.3	2.4	0.6	0.3	3.6	0.1	OMC-1	C	
134	5 35 8.7	-5 20 49.0	10.7	0.8	1.4	0.25	0.46	0.20	4.5	11.4	2.5	0.9	0.4	3.4	0.1	OMC-1	C	
135	5 35 8.7	-5 21 56.5	9.9	1.2	1.1	0.19	0.71	0.30	8.4	20.3	2.4	4.9	0.3	1.6	0.5	OMC-1	...	
136	5 35 8.8	-5 34 19.0	5.6	1.9	1.2	0.19	0.83	0.35	8.0	27.0	3.4	8.8	0.3	0.9	0.5	OMC-4	C	
137	5 35 8.8	-5 35 26.5	8.1	5.1	1.0	0.22	0.56	0.24	22.9	14.7	0.6	1.9	0.3	10.1	0.9	OMC-4	B	AzTEC-Ori 273
138	5 35 8.8	-5 38 4.0	7.9	2.8	1.2	0.25	0.46	0.20	16.2	11.2	0.7	0.9	0.4	12.4	0.4	OMC-4	B	AzTEC-Ori 272
139	5 35 10.2	-5 17 26.5	9.2	3.3	1.1	0.27	0.73	0.31	28.5	30.2	1.1	5.4	0.5	4.8	0.6	OMC-1	C	
140	5 35 10.3	-5 29 4.0	11.1	2.7	1.0	0.24	0.60	0.25	11.6	18.4	1.6	2.4	0.4	4.1	0.3	OMC-1	C	
141	5 35 10.3	-5 32 26.5	5.7	2.1	1.0	0.21	0.75	0.32	11.7	25.0	2.1	6.0	0.3	1.8	0.5	OMC-4	C	
142	5 35 10.3	-5 38 4.0	7.3	3.5	1.1	0.29	0.72	0.30	22.6	31.1	1.4	5.0	0.6	4.1	0.4	OMC-4	B	AzTEC-Ori 272
143	5 35 11.7	-5 13 41.5	11.5	0.8	1.5	0.24	0.83	0.35	4.0	34.8	8.7	8.8	0.4	0.4	0.1	OMC-2/3	C	
144	5 35 11.8	-5 28 41.5	10.3	1.6	1.1	0.25	0.78	0.33	13.9	32.4	2.3	7.1	0.4	1.8	0.4	OMC-1	C	
145	5 35 11.8	-5 34 41.5	8.0	5.0	1.0	0.26	0.54	0.23	24.1	15.9	0.7	1.6	0.5	11.7	0.5	OMC-4	B	AzTEC-Ori 273
146	5 35 13.2	-4 53 49.0	12.7	1.4	1.3	0.16	0.52	0.22	3.6	9.0	2.5	1.4	0.2	2.3	0.4	OMC-2/3	C	
147	5 35 13.2	-4 56 26.5	12.0	2.1	1.7	0.23	0.60	0.26	10.5	17.8	1.7	2.5	0.4	3.6	0.3	OMC-2/3	C	
148	5 35 13.2	-4 59 4.0	10.9	6.2	1.2	0.27	0.87	0.37	58.5	42.9	0.7	10.6	0.5	5.2	1.2	OMC-2/3	C	
149	5 35 13.3	-5 21 56.5	8.7	2.4	1.2	0.31	0.68	0.29	25.2	29.6	1.2	4.1	0.7	5.3	0.4	OMC-1	...	
150	5 35 13.3	-5 22 19.0	7.8	2.7	1.6	0.27	0.43	0.18	15.5	10.4	0.7	0.7	0.5	13.4	0.3	OMC-1	...	

Table 4—Continued

ID C^{18}O -Ori	RA (J2000)	DEC (J2000)	V_{LSR} [km s $^{-1}$]	T_{peak} [K]	Aspect	R_{core} [pc]	dV_{core} [km s $^{-1}$]	σ [km s $^{-1}$]	M_{LTE} [M_{\odot}]	M_{VIR} [M_{\odot}]	\mathcal{R}_{vir}	M_{J} [M_{\odot}]	M_{Φ} [M_{\odot}]	\mathcal{R}_{c}	n [$\times 10^4 \text{ cm}^{-3}$]	area	category	note
151	5 35 13.3	-5 22 41.5	7.2	2.4	1.1	0.23	0.42	0.18	9.5	8.6	0.9	0.6	0.4	9.7	0.3	OMC-1	...	
152	5 35 13.3	-5 23 4.0	8.3	3.6	1.0	0.19	0.56	0.24	10.8	12.8	1.2	1.9	0.3	5.0	0.6	OMC-1	...	
153	5 35 13.3	-5 23 49.0	6.7	3.2	1.7	0.22	1.07	0.45	13.4	51.3	3.8	24.6	0.3	0.5	0.6	OMC-1	...	
154	5 35 13.3	-5 24 11.5	7.2	3.2	1.2	0.20	0.50	0.21	10.3	10.4	1.0	1.2	0.3	7.1	0.5	OMC-1	...	
155	5 35 13.3	-5 24 56.5	8.2	2.3	1.2	0.16	0.57	0.24	8.8	11.0	1.3	2.0	0.2	4.1	0.8	OMC-1	...	
156	5 35 13.3	-5 26 26.5	8.5	3.5	1.6	0.27	0.70	0.30	26.0	27.8	1.1	4.7	0.5	5.0	0.6	OMC-1	...	
157	5 35 13.3	-5 27 11.5	7.7	1.9	1.3	0.25	0.67	0.29	9.3	23.7	2.5	3.9	0.4	2.1	0.3	OMC-1	...	
158	5 35 13.3	-5 33 34.0	7.0	2.7	1.0	0.24	0.70	0.30	19.6	24.9	1.3	4.7	0.4	3.9	0.6	OMC-4	A	AzTEC-Ori 287
159	5 35 13.3	-5 39 56.5	8.4	0.8	1.2	0.19	0.60	0.25	3.4	14.2	4.2	2.4	0.3	1.3	0.2	OMC-4	C	
160	5 35 14.7	-5 4 41.5	11.0	3.8	1.2	0.26	0.67	0.28	36.1	24.7	0.7	3.8	0.5	8.5	0.8	OMC-2/3	C	
161	5 35 14.8	-5 12 11.5	10.8	3.8	1.7	0.22	0.56	0.24	20.6	14.7	0.7	1.9	0.3	9.1	0.8	OMC-2/3	A	AzTEC-Ori 292
162	5 35 14.8	-5 15 34.0	8.8	0.8	1.2	0.23	0.63	0.27	3.7	19.1	5.2	3.0	0.4	1.1	0.1	OMC-2/3	B	AzTEC-Ori 288
163	5 35 14.8	-5 16 19.0	10.3	2.8	1.5	0.22	0.52	0.22	17.1	12.8	0.7	1.4	0.3	9.6	0.6	OMC-1	B	AzTEC-Ori 288
164	5 35 14.8	-5 16 19.0	9.7	1.9	1.0	0.23	0.46	0.19	10.7	9.9	0.9	0.8	0.4	9.0	0.4	OMC-1	B	AzTEC-Ori 288
165	5 35 14.8	-5 26 49.0	10.5	1.9	1.4	0.26	0.53	0.22	14.0	15.5	1.1	1.5	0.5	7.1	0.3	OMC-1	...	
166	5 35 16.2	-4 55 19.0	12.6	1.6	1.0	0.22	0.62	0.26	6.7	17.5	2.6	2.8	0.3	2.1	0.3	OMC-2/3	A	AzTEC-Ori 289
167	5 35 16.3	-5 3 56.5	10.3	3.1	1.9	0.30	0.49	0.21	27.6	15.1	0.5	1.1	0.6	15.9	0.5	OMC-2/3	C	
168	5 35 16.3	-5 4 41.5	9.7	2.1	1.1	0.26	0.90	0.38	11.8	44.1	3.7	12.2	0.5	0.9	0.3	OMC-2/3	C	
169	5 35 16.3	-5 9 34.0	9.9	1.2	1.0	0.31	0.66	0.28	9.8	28.1	2.9	3.6	0.7	2.3	0.1	OMC-2/3	C	
170	5 35 16.3	-5 13 19.0	10.5	3.1	1.3	0.21	0.57	0.24	16.6	14.5	0.9	2.0	0.3	7.2	0.7	OMC-2/3	C	
171	5 35 16.3	-5 14 49.0	10.1	2.9	1.1	0.24	0.49	0.21	16.0	12.3	0.8	1.1	0.4	10.6	0.5	OMC-2/3	⌚	AzTEC-Ori 290
172	5 35 16.3	-5 19 41.5	9.5	3.7	1.0	0.22	0.75	0.32	28.0	26.4	0.9	6.0	0.4	4.4	1.0	OMC-1	⌚	
173	5 35 16.3	-5 21 34.0	9.9	4.3	1.1	0.23	0.89	0.38	26.8	37.9	1.4	11.8	0.4	2.2	0.9	OMC-1	⌚	
174	5 35 16.3	-5 26 4.0	9.9	3.3	1.1	0.29	0.63	0.27	27.9	24.1	0.9	3.0	0.6	7.8	0.5	OMC-1	...	
175	5 35 16.3	-5 30 34.0	6.2	3.2	1.4	0.22	0.69	0.29	13.7	22.0	1.6	4.4	0.3	2.9	0.5	OMC-4	A	AzTEC-Ori 293
176	5 35 16.3	-5 35 4.0	8.4	2.3	1.1	0.27	0.56	0.24	13.1	17.9	1.4	1.9	0.5	5.5	0.3	OMC-4	C	
177	5 35 16.3	-5 39 34.0	9.4	1.0	1.2	0.21	0.47	0.20	2.8	9.5	3.4	0.9	0.3	2.3	0.1	OMC-4	C	
178	5 35 17.7	-4 56 4.0	11.1	0.8	1.2	0.20	0.69	0.29	3.2	20.0	6.2	4.4	0.3	0.7	0.2	OMC-2/3	A	AzTEC-Ori 291
179	5 35 17.8	-5 18 34.0	10.3	2.7	1.1	0.24	0.54	0.23	18.2	15.0	0.8	1.7	0.4	8.8	0.5	OMC-1	...	
180	5 35 19.3	-5 0 34.0	11.1	6.3	1.2	0.25	0.95	0.40	61.8	46.3	0.7	15.4	0.4	3.9	1.8	OMC-2/3	A	AzTEC-Ori 298
181	5 35 19.3	-5 17 4.0	11.0	1.5	1.2	0.26	0.57	0.24	11.1	17.2	1.5	1.9	0.5	4.6	0.3	OMC-1	C	
182	5 35 19.3	-5 18 34.0	9.6	3.7	1.1	0.17	0.79	0.33	16.3	22.6	1.4	7.3	0.2	2.2	1.3	OMC-1	...	
183	5 35 19.3	-5 37 41.5	8.5	0.9	1.1	0.18	0.62	0.26	3.5	14.5	4.1	2.8	0.2	1.2	0.3	OMC-4	C	
184	5 35 20.8	-4 56 49.0	12.0	2.7	1.0	0.25	0.86	0.36	18.0	38.5	2.1	10.2	0.4	1.7	0.5	OMC-2/3	C	
185	5 35 20.8	-5 5 49.0	10.8	4.2	1.3	0.20	0.59	0.25	25.8	14.7	0.6	2.3	0.3	9.9	1.3	OMC-2/3	C	
186	5 35 20.8	-5 7 41.5	10.7	4.0	1.6	0.28	0.75	0.32	48.0	33.7	0.7	6.1	0.6	7.2	0.9	OMC-2/3	C	
187	5 35 20.8	-5 11 26.5	11.3	3.2	1.0	0.27	0.57	0.24	27.7	18.8	0.7	2.0	0.5	10.8	0.6	OMC-2/3	C	
188	5 35 22.3	-5 4 41.5	12.3	1.3	1.8	0.28	0.52	0.22	8.9	16.0	1.8	1.4	0.6	4.6	0.2	OMC-2/3	C	
189	5 35 22.3	-5 12 34.0	10.9	2.3	1.0	0.19	0.47	0.20	8.3	8.9	1.1	0.9	0.3	7.0	0.5	OMC-2/3	B	AzTEC-Ori 316
190	5 35 22.3	-5 14 49.0	10.6	2.7	1.1	0.19	0.65	0.28	14.0	17.3	1.2	3.5	0.3	3.7	0.8	OMC-2/3	A	AzTEC-Ori 310
191	5 35 22.3	-5 25 19.0	11.0	1.3	1.1	0.32	0.60	0.25	7.7	23.7	3.1	2.4	0.7	2.5	0.1	OMC-1	...	
192	5 35 22.3	-5 36 34.0	9.1	0.9	1.4	0.24	0.48	0.20	3.5	11.4	3.3	1.0	0.4	2.5	0.1	OMC-4	C	
193	5 35 23.8	-5 12 56.5	10.6	2.5	1.1	0.19	0.51	0.21	9.9	10.1	1.0	1.2	0.3	6.6	0.6	OMC-2/3	B	AzTEC-Ori 316
194	5 35 25.3	-5 2 49.0	11.1	3.4	1.2	0.23	0.69	0.29	32.2	22.7	0.7	4.4	0.4	6.8	1.2	OMC-2/3	C	
195	5 35 25.3	-5 24 34.0	9.4	1.3	1.3	0.27	0.70	0.30	7.7	27.7	3.6	4.5	0.5	1.5	0.2	OMC-1	...	
196	5 35 26.8	-5 3 34.0	10.8	3.4	1.4	0.24	0.37	0.16	15.8	6.9	0.4	0.3	0.4	20.8	0.5	OMC-2/3	A	AzTEC-Ori 326
197	5 35 26.8	-5 5 49.0	11.5	4.8	1.4	0.23	0.50	0.21	28.3	11.9	0.4	1.2	0.4	18.4	1.0	OMC-2/3	A	AzTEC-Ori 325
198	5 35 26.8	-5 11 4.0	10.8	2.8	1.3	0.23	0.65	0.28	21.0	20.3	1.0	3.5	0.4	5.5	0.8	OMC-2/3	C	
199	5 35 26.8	-5 20 4.0	7.7	0.9	1.2	0.25	0.69	0.29	4.9	25.3	5.2	4.4	0.4	1.0	0.1	OMC-1	C	
200	5 35 26.8	-5 24 34.0	10.4	2.1	1.3	0.29	0.69	0.29	14.6	29.1	2.0	4.4	0.6	2.9	0.3	OMC-1	...	

Table 4—Continued

ID $\text{C}^{18}\text{O}-\text{Ori}$	RA (J2000)	DEC (J2000)	V_{LSR} [km s $^{-1}$]	T_{peak} [K]	Aspect	R_{core} [pc]	dV_{core} [km s $^{-1}$]	σ [km s $^{-1}$]	M_{LTE} [M_{\odot}]	M_{VIR} [M_{\odot}]	\mathcal{R}_{vir}	M_{J} [M_{\odot}]	M_{Φ} [M_{\odot}]	\mathcal{R}_{c}	n [$\times 10^4 \text{ cm}^{-3}$]	area	category	note
201	5 35 28.3	-4 58 19.0	11.7	5.3	1.0	0.29	0.90	0.38	51.7	48.6	0.9	12.5	0.6	3.9	0.9	OMC-2/3	A	AzTEC-Ori 337
202	5 35 28.3	-5 7 19.0	11.5	3.5	1.2	0.23	0.63	0.27	30.3	18.8	0.6	2.9	0.4	9.2	1.1	OMC-2/3	A	AzTEC-Ori 329
203	5 35 29.8	-5 3 11.5	10.4	3.3	1.2	0.32	0.54	0.23	20.5	20.1	1.0	1.7	0.7	8.6	0.3	OMC-2/3	C	
204	5 35 31.3	-5 5 26.5	11.9	4.3	1.2	0.23	0.49	0.21	16.8	11.5	0.7	1.1	0.4	11.5	0.6	OMC-2/3	A	AzTEC-Ori 344
205	5 35 31.3	-5 9 34.0	11.1	3.0	1.1	0.23	0.80	0.34	23.0	30.1	1.3	7.6	0.4	2.9	0.8	OMC-2/3	C	
206	5 35 31.3	-5 20 26.5	7.1	1.3	1.5	0.19	1.04	0.44	5.9	43.9	7.5	22.2	0.3	0.3	0.3	OMC-1	A	AzTEC-Ori 345
207	5 35 34.3	-5 6 56.5	12.4	2.4	1.5	0.28	0.47	0.20	15.9	12.9	0.8	0.9	0.6	10.8	0.3	OMC-2/3	C	
208	5 35 34.3	-5 8 4.0	11.3	2.5	1.1	0.21	0.77	0.33	15.2	26.8	1.8	6.8	0.3	2.1	0.6	OMC-2/3	A	AzTEC-Ori 354
209	5 35 35.8	-5 15 11.5	9.4	0.9	1.4	0.22	0.86	0.37	2.5	34.1	13.4	10.6	0.3	0.2	0.1	OMC-2/3	C	
210	5 35 35.9	-5 21 34.0	6.7	0.9	1.2	0.22	0.79	0.34	3.1	28.4	9.2	7.5	0.3	0.4	0.1	OMC-1	C	
211	5 35 37.3	-5 6 11.5	11.7	3.3	1.3	0.21	0.70	0.30	18.9	21.3	1.1	4.5	0.3	4.0	0.9	OMC-2/3	A	AzTEC-Ori 367
212	5 35 37.4	-5 18 34.0	9.6	1.4	1.4	0.13	0.66	0.28	2.2	12.4	5.6	3.7	0.1	0.6	0.4	OMC-1	A	AzTEC-Ori 365
213	5 35 37.4	-5 19 19.0	7.8	0.8	1.9	0.25	0.48	0.20	4.0	11.9	3.0	1.0	0.4	2.8	0.1	OMC-1	C	
214	5 35 38.8	-5 1 19.0	11.6	2.8	1.1	0.29	0.74	0.31	33.6	32.6	1.0	5.6	0.6	5.5	0.6	OMC-2/3	A	AzTEC-Ori 364
215	5 35 40.4	-5 19 41.5	8.9	1.5	1.6	0.18	0.44	0.19	4.0	7.3	1.8	0.7	0.2	4.3	0.3	OMC-1	C	
216	5 35 41.9	-5 20 49.0	8.3	1.5	1.5	0.23	0.61	0.26	6.3	17.5	2.8	2.6	0.4	2.1	0.2	OMC-1	A	AzTEC-Ori 382
217	5 35 43.4	-5 4 19.0	11.4	1.2	1.1	0.22	0.76	0.32	8.0	26.4	3.3	6.3	0.3	1.2	0.3	OMC-2/3	C	
218	5 35 43.4	-5 11 4.0	10.4	1.8	1.1	0.26	0.69	0.29	9.8	25.9	2.6	4.3	0.5	2.1	0.2	OMC-2/3	A	AzTEC-Ori 387
219	5 35 44.9	-5 19 41.5	9.6	1.3	1.0	0.15	0.53	0.23	2.9	8.8	3.1	1.5	0.2	1.7	0.4	OMC-1	A	AzTEC-Ori 390
220	5 35 47.9	-5 7 41.5	11.4	1.2	1.5	0.22	0.34	0.14	2.6	5.2	2.0	0.3	0.3	4.4	0.1	OMC-2/3	C	
221	5 35 47.9	-5 7 41.5	11.7	1.5	1.2	0.24	0.58	0.25	7.5	16.9	2.3	2.2	0.4	2.9	0.2	OMC-2/3	C	
222	5 35 47.9	-5 21 11.5	8.9	1.5	1.0	0.20	0.58	0.25	5.2	14.2	2.7	2.2	0.3	2.1	0.3	OMC-1	A	AzTEC-Ori 399
223	5 35 47.9	-5 23 49.0	11.5	1.0	1.2	0.22	0.65	0.27	3.7	18.9	5.0	3.3	0.3	1.0	0.2	OMC-1	A	AzTEC-Ori 397
224	5 35 49.4	-5 20 49.0	9.5	1.4	1.0	0.16	0.41	0.18	3.3	5.5	1.7	0.5	0.2	4.6	0.4	OMC-1	C	
225	5 35 50.9	-5 20 26.5	10.2	0.9	1.0	0.15	0.31	0.13	1.5	3.0	2.0	0.2	0.2	4.5	0.2	OMC-1	C	
226	5 35 51.0	-5 41 49.0	7.9	2.6	1.1	0.19	0.60	0.26	8.0	14.7	1.8	2.5	0.3	2.9	0.5	DLSF	A	AzTEC-Ori 413
227	5 35 52.5	-5 30 11.5	12.2	1.1	1.1	0.17	0.59	0.25	2.5	12.4	5.0	2.3	0.2	1.0	0.2	DLSF	C	
228	5 35 52.5	-5 31 41.5	7.3	2.4	1.9	0.32	0.58	0.24	22.5	22.3	1.0	2.1	0.7	8.0	0.3	DLSF	C	
229	5 35 58.5	-5 29 4.0	9.8	0.7	1.6	0.17	0.45	0.19	1.8	7.2	4.0	0.7	0.2	1.9	0.1	DLSF	C	
230	5 36 0.0	-5 38 4.0	7.9	1.2	1.1	0.18	0.49	0.21	2.7	9.0	3.4	1.1	0.2	2.0	0.2	DLSF	A	AzTEC-Ori 452
231	5 36 3.0	-5 41 49.0	8.3	1.3	1.4	0.19	0.67	0.28	3.9	17.2	4.4	3.7	0.2	1.0	0.3	DLSF	A	AzTEC-Ori 467
232	5 36 4.5	-5 35 26.5	10.3	0.8	1.4	0.22	0.40	0.17	1.9	7.2	3.7	0.5	0.3	2.4	0.1	DLSF	A	AzTEC-Ori 468
233	5 36 6.0	-5 38 49.0	7.7	1.3	1.0	0.18	0.55	0.23	3.3	11.4	3.4	1.8	0.2	1.7	0.2	DLSF	C	
234	5 36 9.0	-5 35 4.0	8.4	1.8	1.1	0.18	0.51	0.22	3.8	10.0	2.7	1.3	0.2	2.5	0.3	DLSF	B	AzTEC-Ori 482
235	5 36 10.6	-5 35 26.5	7.8	1.0	1.1	0.19	0.67	0.28	2.6	17.5	6.8	3.8	0.2	0.6	0.2	DLSF	B	AzTEC-Ori 482

Table 5. Numbers and number densities of the 1.1 mm dust cores, protostars, and pre-main sequence stars in the six distinct regions

Region	Area definition			Number			Number density		
	BLC	TRC	area [pc ²]	1.1 mm †	protostar	PMS star	1.1 mm † [pc ⁻²]	protostar [pc ⁻²]	PMS star [pc ⁻²]
	RA _{J2000} , DEC _{J2000}	RA _{J2000} , DEC _{J2000}							
OMC1	5 36 00, -5 32 35	5 34 35, -5 13 35	5.6	...	45	621	...	8.0	110.2
OMC2/3	5 36 05, -5 14 40	5 34 40, -4 46 40	8.1	55	51	286	6.8	6.3	35.5
OMC4	5 35 22, -5 47 42	5 34 42, -5 28 42	2.6	19	19	190	7.4	7.4	73.9
DLSF	5 36 15, -5 48 35	5 35 35, -5 24 35	3.2	36	1	65	11.1	0.3	20.0
Bending	5 34 45, -5 43 30	5 33 30, -5 21 30	5.6	47	11	90	8.4	2.0	16.1
South	5 38 00, -6 55 30	5 34 30, -5 45 30	49.8	209	61	366	4.2	1.2	7.4

†Numbers of 1.1 mm dust cores without YSOs.

Table 6: Kolmogorov-Smirnov Test for R_{core} and dV_{core} †,‡

$R_{\text{core}} \setminus dV_{\text{core}}$	OMC1	OMC23	OMC4	DLSF	Bending
OMC1	...	97.5%	67.5%	31.3%	97.5%
OMC23	97.5%	...	67.5%	3.1%	67.5%
OMC4	67.5%	67.5%	...	67.5%	97.5%
DLSF	11.1%	11.1%	31.3%	...	67.5%
Bending	67.5%	97.5%	97.5%	11.1%	...

†Values in the upper triangular portion are the probabilities of the KS test for dV_{core} .

‡Values in the lower triangular portion are the probabilities of the KS test for R_{core} .

Table 7: Kolmogorov-Smirnov Test for R_{vir} and M_{LTE} †,‡

$R_{\text{vir}} \setminus M_{\text{LTE}}$	OMC1	OMC23	OMC4	DLSF	Bending
OMC1	...	97.5%	11.1%	0.7%	67.5%
OMC23	97.5%	...	11.1%	0.7%	67.5%
OMC4	67.5%	31.3%	...	67.5%	67.5%
DLSF	31.3%	11.1%	31.3%	...	11.1%
Bending	97.5%	67.5%	97.5%	67.5%	...

†Values in the upper triangular portion are the probabilities of the KS test for M_{LTE} .

‡Values in the lower triangular portion are the probabilities of the KS test for R_{vir} .

Table 8. Numbers and fractions of the 1.1 mm dust and C¹⁸O cores in each category

	1.1 mm core	C ¹⁸ O		
		bound	unbound	total
Category A	69/257 (26.8 %)	56/156 (35.9 %)	13/57 (22.8 %)	69/213 (32.4 %)
Category B	10/257 (3.9 %)	19/156 (12.2 %)	4/57 (7.0 %)	23/213 (10.8 %)
Category C	...	81/156 (51.9 %)	40/57 (70.2 %)	121/213 (56.8 %)
Category D	178/257 (69.3 %)

Table 9. Area definition of PDRs

Region	Area definition	
	BLC	TRC
	RA _{J2000} , DEC _{J2000}	RA _{J2000} , DEC _{J2000}
DLSF	5 36 15, -5 48 35	5 35 35, -5 24 35
M43	5 36 00, -5 24 35	5 35 25, -5 13 06
Region A	5 34 48, -5 20 54	5 34 04, -5 13 06
Region B	5 34 08, -5 26 06	5 33 49, -5 20 36
Region C	5 34 01, -5 41 30	5 35 27, -5 37 30
Region D	5 35 35, -5 42 18	5 35 24, -5 38 00

Table 10. Numbers and fractions of the 850 μ m, C¹⁸O, H¹³CO⁺, and N₂H⁺ cores associated with the 1.1 mm dust cores

850 μ m [†]	C ¹⁸ O (1-0)			H ¹³ CO ⁺ (1-0) [†]	N ₂ H ⁺ (1-0) [†]
	bound	unbound	total		
133/215 (61.9 %)	75/156 (48.1 %)	17/57 (29.8 %)	92/213 (43.2 %)	119/210 (56.7 %)	21/27 (77.8 %)

[†]Catalogs of the 850 μ m, H¹³CO⁺, and N₂H⁺ cores are from Nutter & Ward-Thompson (2007), Ikeda et al. (2007), and Tatematsu et al. (2008), respectively.

A. Weak dependence of the core properties on the Clumpfind parameters

As described in Section 2.1.1, the properties of the cores identified by the Clumpfind algorithm in some degree depend on the input parameters of the algorithm. In order to investigate the influence of the Clumpfind parameters on the core properties, we performed the core identification with various step sizes and threshold levels in a reasonable range of 2σ to 5σ . Figure 24 shows the resulting number, R_{core} , dV_{core} , and M_{LTE} of the identified C^{18}O cores as a function of the step size and the threshold level. The number of the identified C^{18}O cores significantly decreases with increasing step size, while the core number weakly depends on the threshold level. In contrast, the dependence of the number of cores on the threshold is week. The R_{core} , dV_{core} , and M_{LTE} values gradually increase with increasing step size, but do not depend on the threshold level. In conclusion, we demonstrated the weak dependence of the core properties on both the step size and the threshold level in a reasonable range of 2σ to 5σ , which was also shown by Pineda et al. (2009) and Ikeda & Kitamura (2009). Figure 25 shows the distribution of the identified C^{18}O cores with various step sizes and threshold levels. Most C^{18}O cores having weak intensities are not identified by the Clumpfind with a larger step size and threshold level, and some C^{18}O cores which are close to each other are merged into one core.

The source extraction with a 2σ threshold level and a 5σ step size identified some cores which are not identified with a 2σ threshold level and a 2σ step size. Figures 26 (a) and (b) show the difference in the core identification with the two different step sizes and the same threshold level. As described in Section 2.2.1, a core must contain two or more continuous velocity channels, and they must have at least 3 pixels whose intensities are above the 3σ level, and in addition the pixels must be connected to one another in both the space and velocity domains. In the case of a 2σ threshold level and a 2σ step size, the cores labeled as A, B, and C are flagged out due to the lack of the velocity width (pixels along the velocity axis) as shown in Fig 26 (a). However, in the case of a 2σ threshold level and a 5σ step size, these cores are merged along the velocity axis and the merged cores labeled as D are identified as shown in Fig 26 (b). The source extraction with a 2σ threshold level and a 5σ step size does not identify the some cores which are identified with a 2σ threshold level and a 2σ step size as shown in Figs. 26 (c) and (d) . In the case of a 2σ threshold level and a 2σ step size, the core labeled as E is identified. However, the core labeled as F is flagged out due to the lack of the velocity width and spatial size. In the case of a 2σ threshold level and a 5σ step size, the velocity width of each core is changed due to the different step size. The core labeled as G is flagged out due to the lack of the velocity width. The core labeled as H is also flagged out due to the lack of the spatial size.

B. How the Clumpfind identified the dust and C¹⁸O cores in the mapping data

In Section 2.1.1 and 2.2.1, we identified cores from the 1.1 mm dust continuum and C¹⁸O emission using the Clumpfind method (Williams et al. 1994). Although this algorithm has been widely used for the identification of cores and clumps, results of the identification are known to vary depending on the parameters used in the algorithm (Pineda et al. 2009). In order to see how the algorithm works in the case of our catalog, we compare the distribution of the cores with the 1.1 mm dust continuum and C¹⁸O maps.

Figures 27 – 30 show the distribution of the identified 1.1 mm dust cores overlaid on the 1.1 mm dust continuum maps with the boundaries of each core. The movie of the C¹⁸O velocity channel maps with a velocity resolution of 0.104 km s⁻¹ overlaid the positions of the identified C¹⁸O cores are available at the web page of the NRO star formation project (via <http://th.nao.ac.jp/MEMBER/nakamrfm/sflegacy/sflegacy.html>). The apparent distributions of the 1.1mm dust and C¹⁸O cores have good agreements with the positions of the cores identified by the Clumpfind.

C. Effectiveness of the FRUIT method in extracting the dust core properties from the ground-based bolometer array map

Shimajiri et al. (2011) applied a principal component analysis (PCA) cleaning method to remove atmospheric noise in the AzTEC 1.1 mm dust continuum map. The PCA cleaning, however, removes also astronomical signals in the case that the emission has an extended structure, because the PCA method can not distinguish the extended astronomical emission over several bolometer array elements from the extended atmospheric emission. This causes the negative-flux feature around bright objects. Figure 31 shows the intensity profiles of the 1.1mm dust continuum emission along the R.A. direction for the three brightest cores with flux densities above 3 Jy beam⁻¹. The negative flux features around the bright objects are clearly recognized in the PCA profiles. Hence the flux density and size of the extended sources are underestimated.

In order to recover the extended features in our Orion map after the PCA cleaning, an interactive mapping method FRUIT was applied. To investigate the performance of the FRUIT data reduction, Shimajiri et al. (2011) performed a simulation in which Gaussian sources with various FWHM sizes and total flux were implanted in Orion data-set as described in Section 2.1.1. The larger the FWHM size of the model source, the lower the recovered fraction of the input total flux densities were artificially embedded in the Orion

data. In the case that the FWHM size of the input source is below $150''$ (~ 0.3 pc), the output total flux density is underestimated by less than 20%. Since the size range of the identified 1.1 mm cores is 0.01 – 0.20 pc, we believe that the sizes and flux densities of the dust cores are well recovered on the 1.1 mm map. In fact, significant negative flux features can not be recognized in the FRUIT map as seen in Figure 31.

We also investigated the recovery of source size using the same simulation data set in Shimajiri et al. (2011). Figure 32 shows how the input source size is recovered. In the case that the inserted source sizes are less than $120''$ (~ 0.24 pc), the source sizes are mostly recovered. In the case that inserted source sizes are $240''$ (~ 0.5 pc), the source sizes are underestimated by 20%. In our results, the size range of the 1.1 mm dust cores is 0.01 – 0.20 pc, and we did not detect any cores with sizes of 0.2 – 0.5 pc. These results suggest that there are no large ($> \sim 0.5$ pc) cores which could not be well recovered by the FRUIT method and were misidentified as smaller ($< \sim 0.5$ pc) cores. We conclude that the source size of the cores detected in the 1.1 mm dust continuum map is mostly recovered.

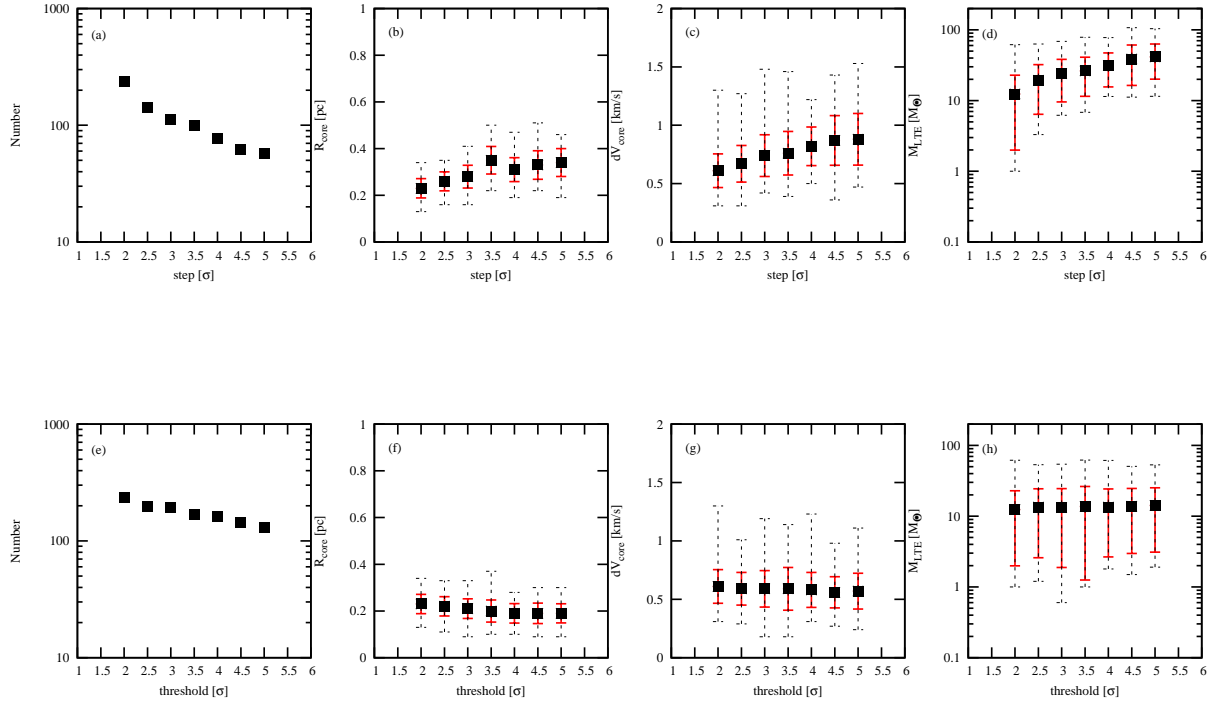


Fig. 24.— (a) Number, (b) R_{core} , (c) dV_{core} , and (d) M_{LTE} of the identified C^{18}O cores as a function of the step size with a threshold level of 2σ in the Clumpfind algorithm. (e) Number, (f) R_{core} , (g) dV_{core} , and (h) M_{LTE} as a function of the threshold level with a step size of 2σ . In the panels (b), (c), (d), (f), (g), and (h), the back filled squares show the mean values and the lower and upper limits in black show the minimum and maximum values. The red error bars indicate the standard deviation.

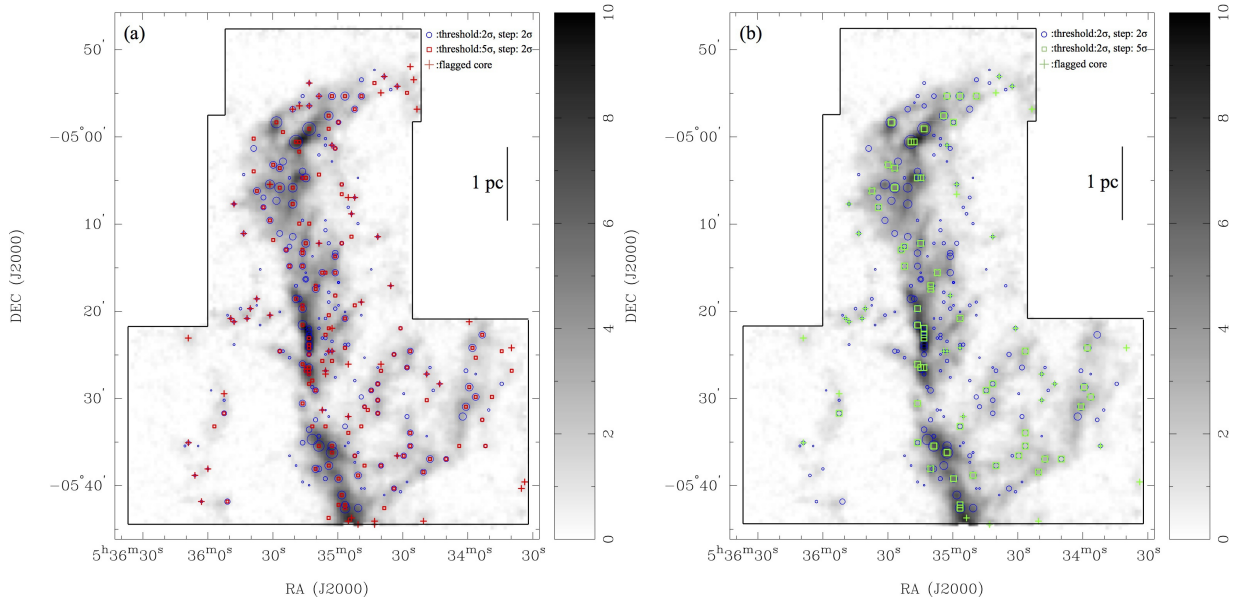


Fig. 25.— Positions of the C¹⁸O cores identified by the Clumpfind algorithm with various parameters on the C¹⁸O total integrated intensity map (gray scale). The blue circles indicate the C¹⁸O cores identified with a 2σ threshold level and a 2σ step size. Their sizes are set to be proportional to their peak intensities. In panel (a), the red squares indicate the C¹⁸O cores identified with a 5σ threshold level and a 2σ step size. In panel (b), the green squares indicate the C¹⁸O cores identified with a 2σ threshold level and a 5σ step size. In both panels, the crosses indicate the C¹⁸O cores flagged out due to the lack of the spatial size and/or velocity width.

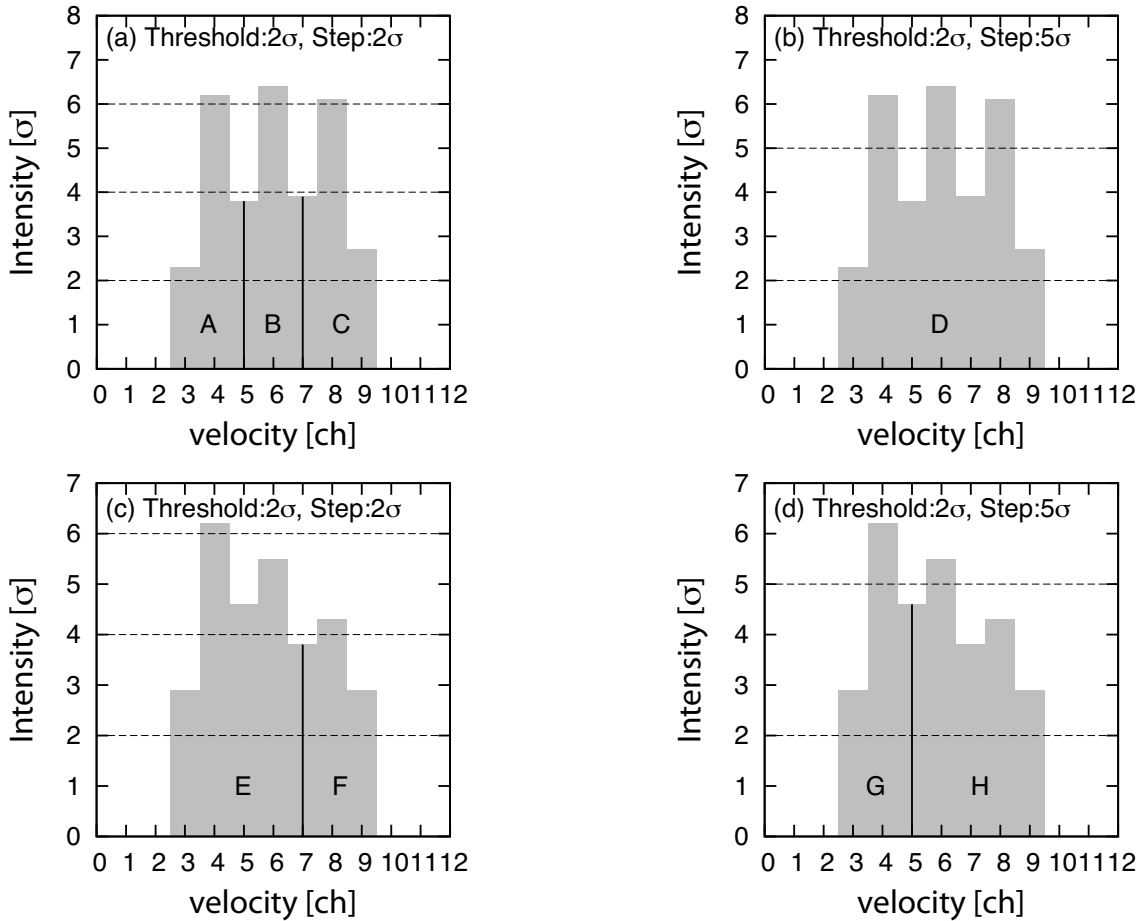


Fig. 26.— Plots to typically show the difference in the core identification with various parameters. The four panels show the distribution of the identified cores along the velocity axis. The panels (a) and (c) are for the source extraction with a 2σ threshold level and a 2σ step size. The panels (b) and (d) are for the source extraction with a 2σ threshold level and a 5σ step size. The horizontal axis shows the velocity in units of channel. The vertical axis shows the intensity in units of σ .

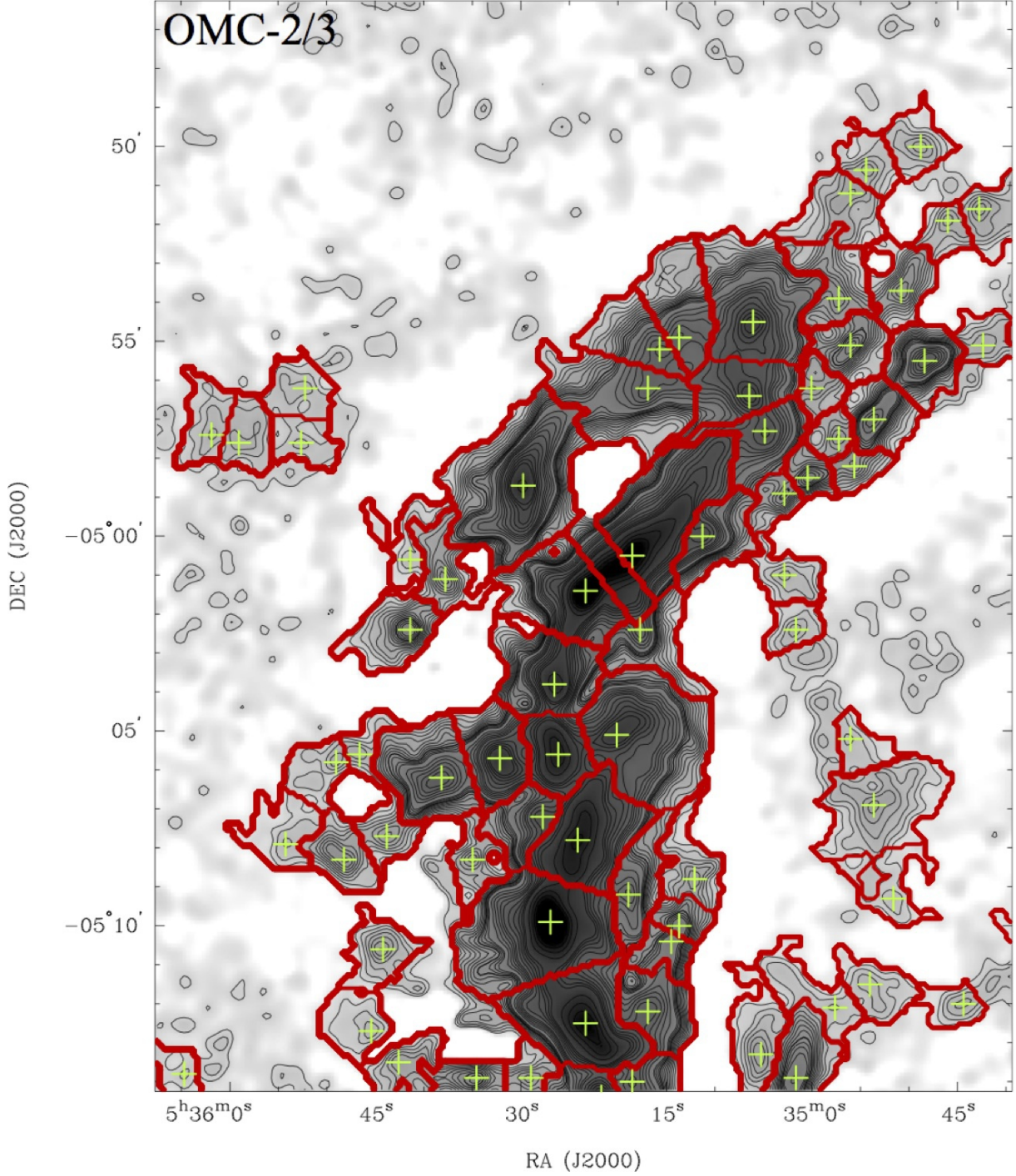


Fig. 27.— The identified 1.1 mm dust cores on the AzTEC 1.1mm maps of the OMC-2/3 region. The green plus signs show the positions of the 1.1 mm dust cores, and the thick red lines denote their boundaries defined by the Clumpfind algorithm. The contours start from 4σ noise level with an increment of 2σ for the range $4\text{--}30\sigma$, 5σ for the range $30\text{--}105\sigma$, and 50σ for the range $>105\sigma$ ($1\sigma=9$ mJy beam $^{-1}$).

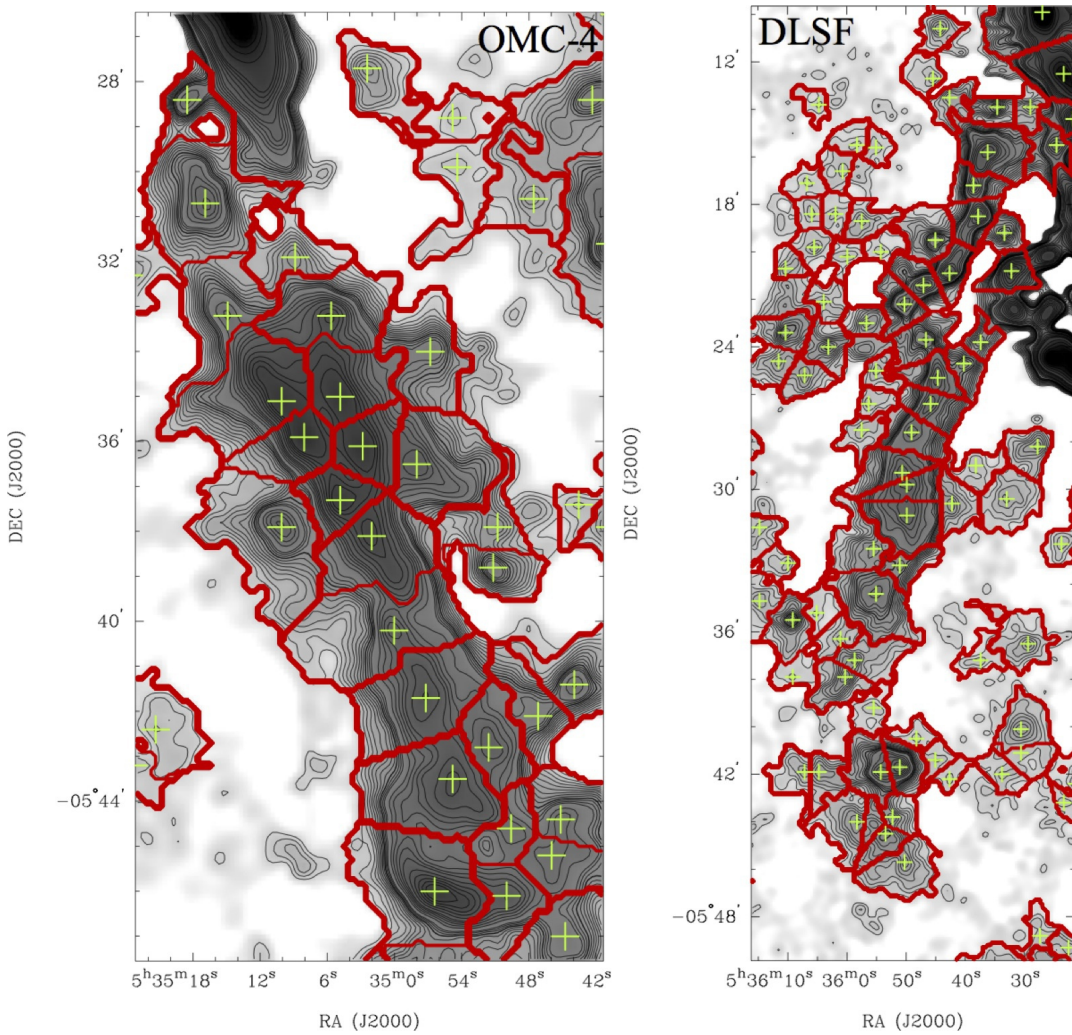


Fig. 28.— Same as Fig. 27, but for the OMC-4 and DLSF regions.

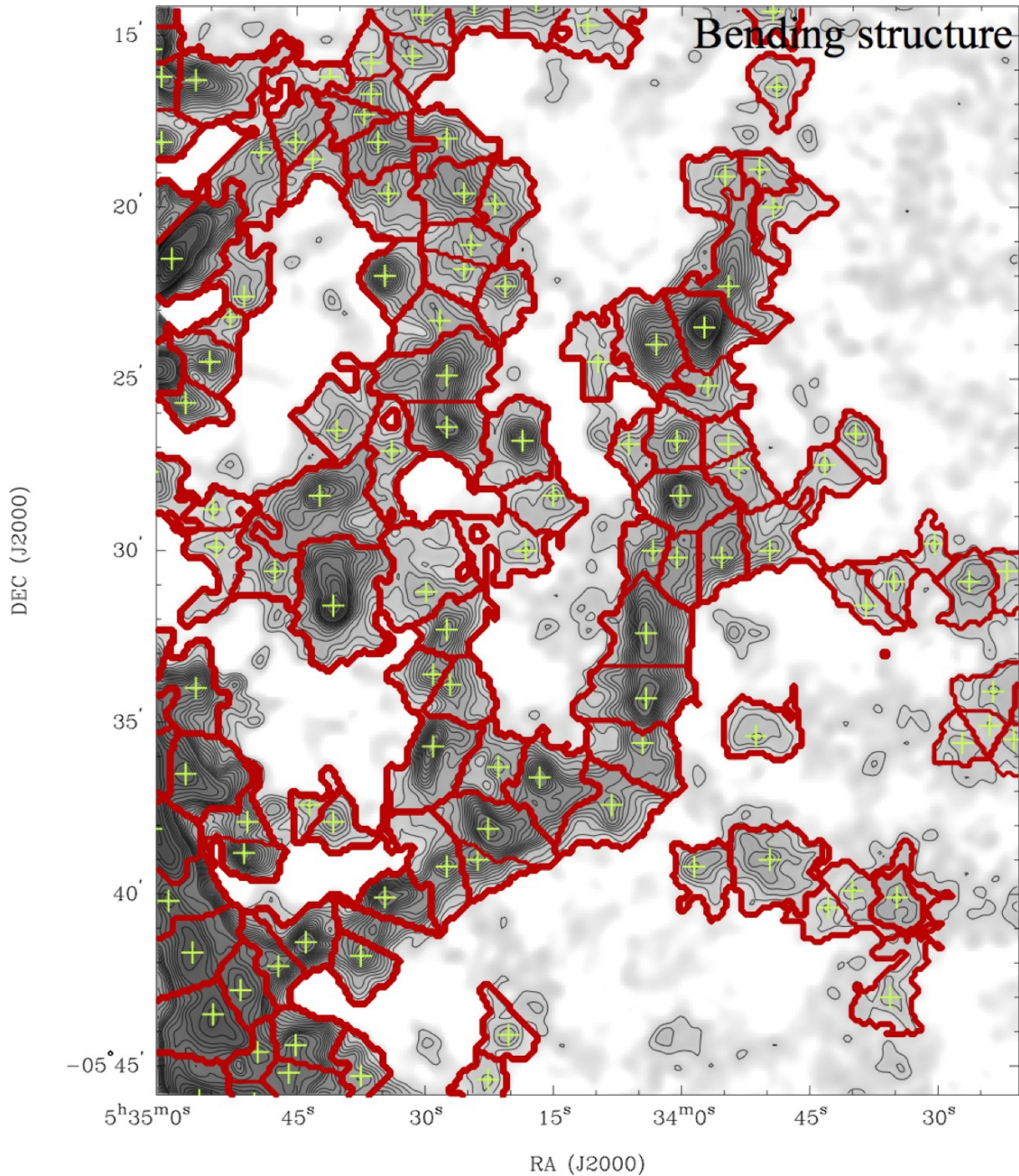


Fig. 29.— Same as Fig. 27, but for the bending structure region.

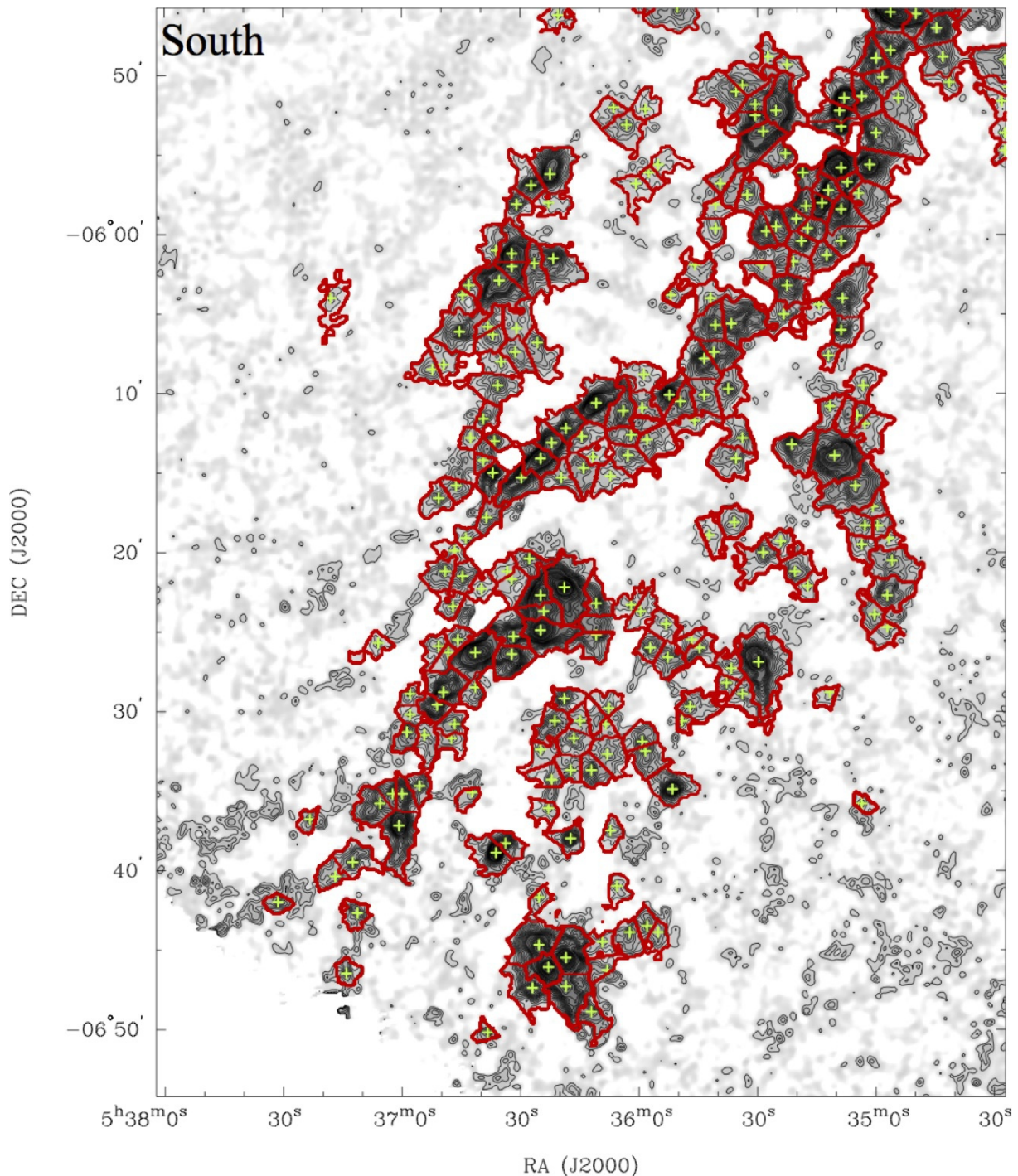


Fig. 30.— Same as Fig. 27, but for the South region.

(Peak flux density=4.87Jy/beam)

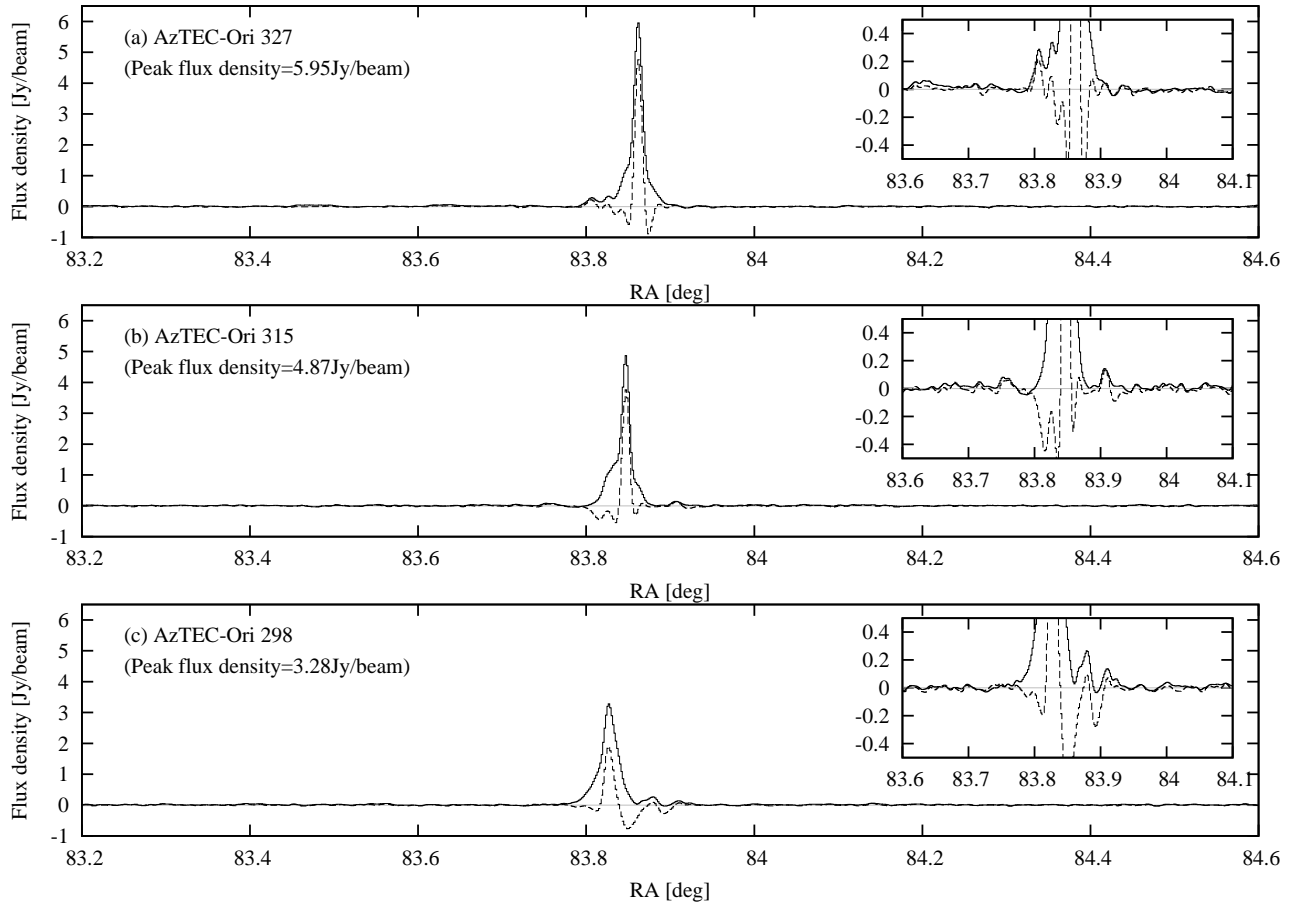


Fig. 31.— Intensity profiles of the 1.1 mm dust continuum emission along the R.A. direction for the three brightest cores of (a) AzTEC-Ori 327 (DEC = $-5^{\circ} 9' 54''$.4), (b) 315 (DEC = $-5^{\circ} 1' 24''$.4), and (c) 298 (DEC = $-5^{\circ} 0' 30''$.4). The cut lines along the Dec. direction go through the peak positions of the cores. The black dashed lines indicate the PCA profiles. The black solid lines indicate the FRUIT profiles.

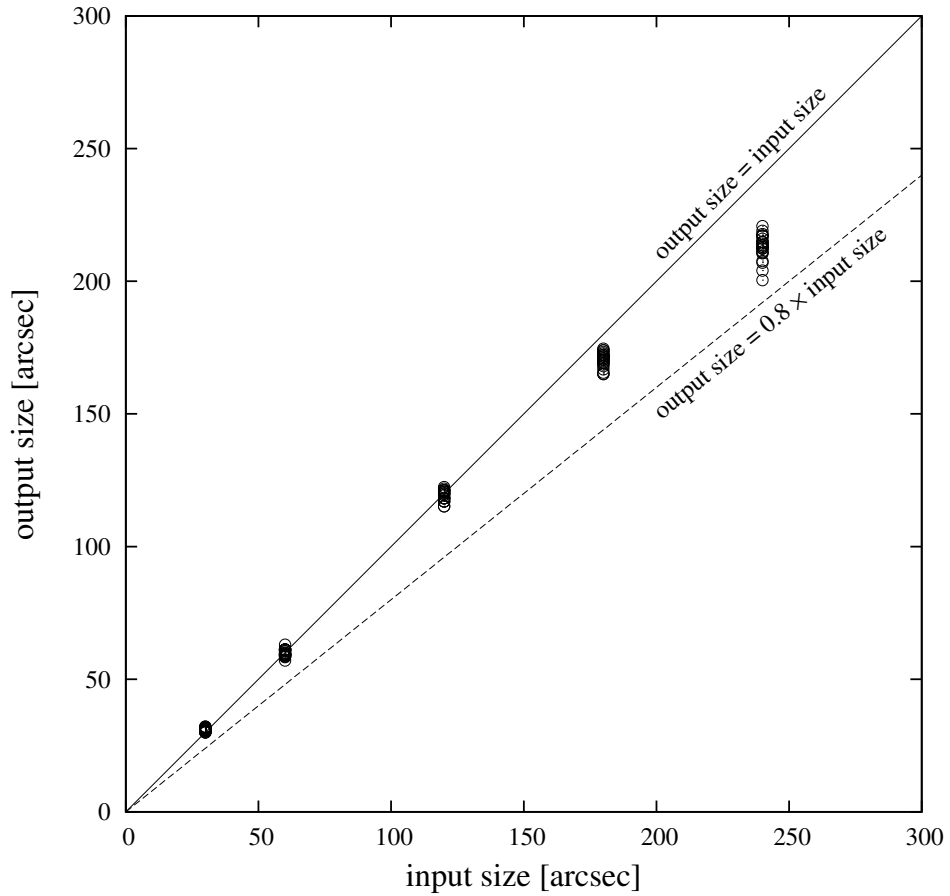


Fig. 32.— Recovery of the source size for simulation observations. We performed a simulation in which twenty five Gaussian sources with a peak flux of 1 Jy and FWHM sizes of 30'', 60'', 120'', 180'', and 240'' were inserted to Orion data-set. The solid and broken lines indicate (output size = input size) and (output size = $0.8 \times$ input size), respectively.